The Effect of Scintillation on Ground-Based Exoplanet Transit Photometry

FOHRING, DORA

The Effect of Scintillation on Ground-Based Exoplanet Transit Photometry

Dóra Föhring

A Thesis presented for the degree of
Doctor of Philosophy

Centre for Advanced Instrumentation
Department of Physics
University of Durham
England

September 2014

The Effect of Scintillation on Ground-Based Exoplanet Transit Photometry

Dóra Föhring

Submitted for the degree of Doctor of Philosophy
September 2014

Abstract

In this thesis, the effect of scintillation arising from atmospheric optical turbulence on exoplanet transit and secondary eclipse photometry is examined. Atmospheric scintillation arises from the propagation of phase aberrations resulting from wavefront perturbations due to optical turbulence high in the atmosphere. Scintillation causes intensity variations of astronomical targets, which is a problem in exoplanet transit photometry, where the measurement of a decrease in brightness of 1% or less is required. For this reason, ground-based telescopes have inferior photometric precision compared to their space-based counterparts, despite having the advantage of a reduced cost.

In contrast with previous work on the detection limits of fast photometry, which is obtained for an atmosphere averaged over time, the actual scintillation noise can vary considerably from night to night depending on the magnitude of the high-altitude turbulence. From simulation of turbulent layers, the regimes where scintillation is the dominant source of noise on photometry are presented. These are shown to be in good agreement with the analytical, layer based, equations for scintillation. Through Bayesian analysis, the relationship between the errors on the light and the uncertainties on the astrophysical parameters are examined. The errors on the light curve arising from scintillation linearly increase the scatter on the astrophysical parameters with a gradient in the range of 0.68 – 0.80.

The noise due to the photometry aperture is investigated. It is found that for short exposure in times in good seeing, speckle noise contributes to noise in

photometry for aperture sizes of up to approximately 2.3×FWHM.

The results from simultaneous turbulence profiling and time-series photometry are presented. It is found that turbulence profiling can be used to accurately predict the amount of scintillation noise present in photometric observations.

An investigation of the secondary eclipse of WASP-12b on the William Herschel Telescope (WHT) is performed, resulting in a high quality z-band light curve for WASP-12b consistent with a carbon-rich model and with no evidence for strong thermal inversion.

Declaration

The work in this thesis is based on research carried out at the Centre for Advanced Instrumentation, the Department of Physics, England. No part of this thesis has been submitted elsewhere for any other degree or qualification and it is all my own work unless referenced to the contrary in the text.
Parts of this work have appeared in the following publications:

"ULTRACAM z'-band Detection of the Secondary Eclipse of WASP-12b"
D. Föhring, V. S. Dhillon, N. Madhusudhan, T. R. Marsh, C. M. Copperwheat, S. P. Littlefair, R. W. Wilson
MNRAS, 435, 2268 (2013)

"Scintillation Noise in Exoplanet Transit Photometry"
D. Föhring, R. Wilson, J. Osborn, V. S. Dhillon
Proc. of IOP: conference series, Adapting to the Atmosphere, 2015, in prep.

"Scintillation correction for high precision photometry using Conjugate-Plane Photometry: on-sky results"
J. Osborn, R. Wilson, T. Butterley, D. Föhring, V. S. Dhillon
MNRAS, in prep.

"Characterising atmospheric optical turbulence using stereo-SCIDAR
J. Osborn, R. Wilson, T. Butterley, T. Morris, D. Föhring, R. Avila
Proc. of IOP: conference series, Adapting to the Atmosphere, 2015, in prep.

Acknowledgements

First and foremost, I would like to thank my supervisors Richard Wilson and Vik Dhillon. Richard has tirelessly guided, supported and encouraged me through the ups and downs of this journey, and without him this work would not have been possible. My deepest thanks extend also to Vik, whose energy, enthusiasm and vast wealth of knowledge have been invaluable.

In addition to my supervisors, I would like to thank everyone who has in some manner supported me along the way. I would like to thank James Osborn, for all his help, especially with everything related to turbulence profiling, and for always being up for a good chat about physics. I would like to extend my thanks to Stuart Littlefair, for all his expertise and help with the mysteries of pipeline software installation and data reduction. Many thanks also go to Tim Butterley, for his helpful discussions, much time in the beginning helping me get started up with software, and for dealing with, on many occasions, the fallout of my simulations. Thanks also to Chris Saunter, Tim Morris and Ali Bharmal for helpful comments on my work.

I would also like to thank my office mates, who have been through this along with me. In particular, Saavi Perera, for making sure I was always well fed with chocolates and cakes, Matt Townson, for always finding the latest relief from work on the internet, and Scott Silburn and Rob Harris, for sharing the pain of the last few months with me. Special thanks go to Daniel Farrow, whose friendship and company I have benefitted from throughout my time in Durham.

Finally, I would like to thank my Mum and Dad for their support and love through all these years and since the very beginning, and for encouraging me to follow my dreams.

Contents

List of Figures

List of Tables

Chapter 1

Introduction

There are infinite worlds both like and unlike this world of ours

—Epicurus c. 300 BC

The existence of planets orbiting around stars other than the Sun has been postulated since ancient history by philosophers such as Aristotle and Epicurus. Planets outside of our solar system are called extrasolar planets, or exoplanets. While the first modern scientific studies into the possibility of detecting planets around other stars have existed since the 1970s [56], it was not only until 1995 that the first planet orbiting a main-sequence star, 51 Pegasi b, was confirmed [91]. Today, as of August 2014, nearly 20 years since the first discovery and more than 2000 since Aristotle, we currently know of over 1800 confirmed exoplanets[1].

The rapid growth of the field of exoplanet study is driven by our thirst for answering some of the biggest questions of our existence: Where have we come from? What is our place in the Cosmos? Are we alone? Efforts in the field are divided into two areas: the search for new, ultimately Earth-like planets, and the characterisation of exoplanets, primarily through their atmospheric properties. Both play a crucial role in answering these questions. Through the search for new planets, we can gain insight into the distribution of exoplanetary systems, learn about their orbital architectures and how common planets like the Earth are, and find new

[1] http://exoplanet.eu

interesting targets for follow-up. The holy grail of the search for exoplanets is to find an Earth-analogue planet in the habitable zone of its star, which would have significant implications on the prospect of the detection of life. Characterisation of exoplanet atmospheres provides an important means for refining our models of planet formation and for the development of new physical models to explain the properties observed, some of which have no likeness in our solar system. In addition to unveiling the properties of a plethora of exotic systems, exoplanet atmospheric characterisation enables the detection of molecules in the atmosphere which can be used as biomarkers for the detection of life.

There are several methods currently known for studying extrasolar planets. The main methods are: transits, radial velocity measurements, direct imaging, microlensing, astrometry and timing. Figure 1.1 shows the distribution of the known exoplanets as of 2012 by mass and orbital radius. From this diagram it can be seen that transits are most sensitive to the detection of close-in planets, while radial velocity, microlensing and imaging are most sensitive to planets further from the star.

Since the first detection of a photometric eclipse [22; 59] a new window has opened up for obtaining information about exoplanetary systems that is not accessible by other means. Some of the science enabled by transits include determination of absolute planetary and stellar parameters such as the radius and orbital eccentricity and inclination. Combining these with radial velocity measurements allows for an estimation of the true masses and densities, providing a constraint on the planets composition (see e.g. Winn [142]). Variations in transit timing can be used to infer the existence of non-transiting planets [62] or moons in the system [71], and longer-period variations can be used to indicate orbital precession [93]. Doppler shift measurements during transit allow determination of orbital obliquity [51]. Spectroscopy during transit allows the measurement of the absorption due to the planetary atmosphere giving insights into its composition [24; 137], whereas spectroscopy during the secondary eclipse, when the planet passes behind the star, can reveal thermal emissions and dayside temperature and be used for estimating the planetary albedo and inferring zonal winds [115].

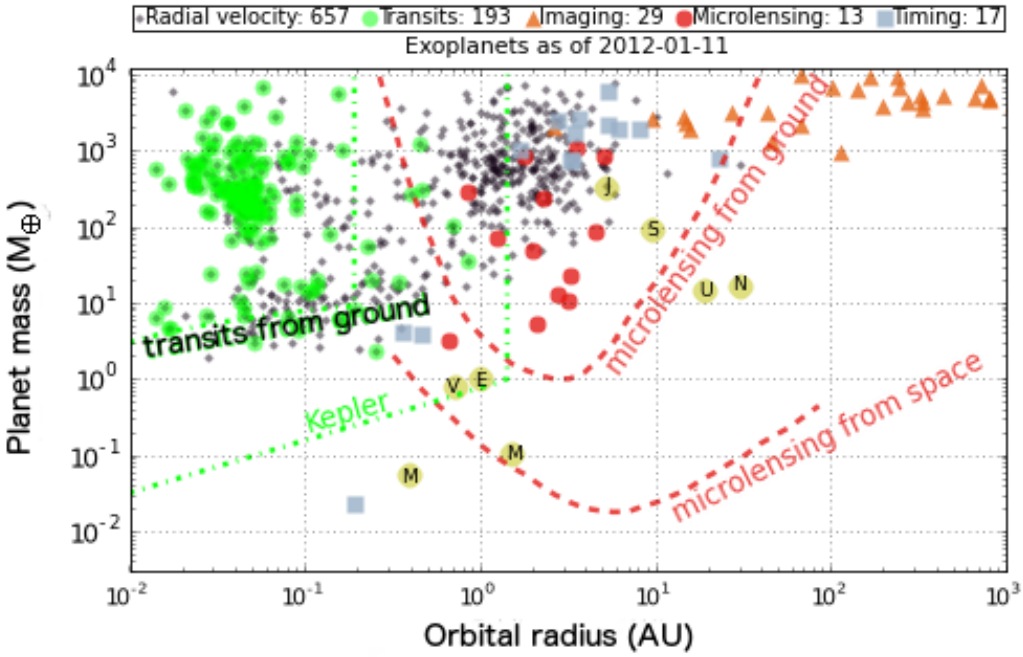

Figure 1.1: Exoplanets as of 2012 by mass and orbital radius. The location of the Earth, Jupiter and Hot Jupiters are shown. Transit detection is most sensitive to close-in planets, while radial velocity, microlensing and imaging are most sensitive to planets further from the star. We note that since 2014 the transit method has surpassed the radial velocity method as the most productive means of exoplanet detection due to new discoveries from Kepler. Presently, only observations from space are sensitive enough to be able to detect planets of mass of the order of the Earth. This is due to the effect of Earth's atmosphere. *Image credit: Yannis Tsapras lcogt.net.*

Both ground- and space-based instruments will continue to play a vital role in the future of exoplanet detection and characterisation. Up to now, space-based observations have provided the highest quality data [28]. In figure 1.1, it can be seen that presently only observations from space are sensitive enough to be able to detect planets the size of the order of the Earth. However, space-based observations are not without disadvantage: they are constrained by the enormous cost involved and are subject to calibration issues. In comparison, ground-based telescopes are three orders of magnitude cheaper to build per unit area of telescope than the equivalent in space. This means that for the same cost, a much larger telescope apertures can be built on the ground which enable a much higher signal-to-noise ratio, as long as the atmosphere induced noise can be corrected for.

The effects of the atmosphere on astronomy have been well documented in the past [116]. They include: Extinction, sky background, transparency variations, seeing and scintillation.

- *Atmospheric extinction*, is caused by energy absorbed by the rotation and vibration of molecules in the atmosphere and reradiated at different wavelengths. The air molecules also scatter the light from the astronomical object, which results in an overall dimming of the observed image at the telescope. The amount of extinction is dependent on the airmass the light needs to travel through, and the local atmospheric conditions. Atmospheric extinction is also highly wavelength dependent, which limits the spectral region that can be observed from the ground to the visible and a number of windows at the infrared wavelengths.

- *Sky background*, arises from emission and scattering from molecules in the atmosphere. Emission is caused by reradiated thermal energy in the infrared and spectral emission lines of molecules, such as OH. Air molecules, aerosols and dust scatter the light from the moon and the surface of Earth (light pollution) resulting in a noisy background that can make the detection of faint objects difficult, particularly when the illuminated moon is present.

- *Transparency variations*, are caused by absorption due to water vapour (clouds)

in the atmosphere. The amount of absorption varies as the wind blows clouds across the field of view of the telescope. The resulting transparency variations range from partial reduction in intensity due to thin cirrus, to complete coverage due to thick cloud.

- *Atmospheric seeing and scintillation*, is caused by light passing between media of varying refractive index, which is a function of temperature and pressure. Turbulence in the atmosphere causes light passing through different paths in the atmosphere to experience different amounts of refraction. This gives rise to image motion and blurring, and a second order effect causing irradiance fluctuations, as refraction causes extra light to be focussed into or out of the telescope aperture. The former effects are referred to as atmospheric seeing, and the latter is scintillation, one of the main topics of this thesis. Figure 1.2 describes the principle of scintillation.

Whilst seeing, the first order effect of atmospheric refraction which causes blurring and motion of the PSF (point spread function), can be corrected through adaptive optics, scintillation can only be partially corrected through such techniques. The correction for scintillation is possible, but requires a dedicated instrument, such as the Conjugate-Plane Photometer [102]. Before we fully make use of these scintillation-correcting instruments, we need to know what contribution scintillation makes to the light curves from the ground, which is one of the main aims of this thesis.

Through fully characterising the effects of the Earth's atmosphere we are able to:

1. Know under what conditions noise due to the atmosphere is limiting the precision of our observation in order to improve observation strategy, and

2. Be able to assess the improvement we should expect through the use of adaptive optics and/or scintillation correcting techniques and know when these techniques offer advantages over standard observation.

In this thesis I examine the sources of noise on transit photometry through simulation and observation to determine the effects of scintillation on the noise budget and the

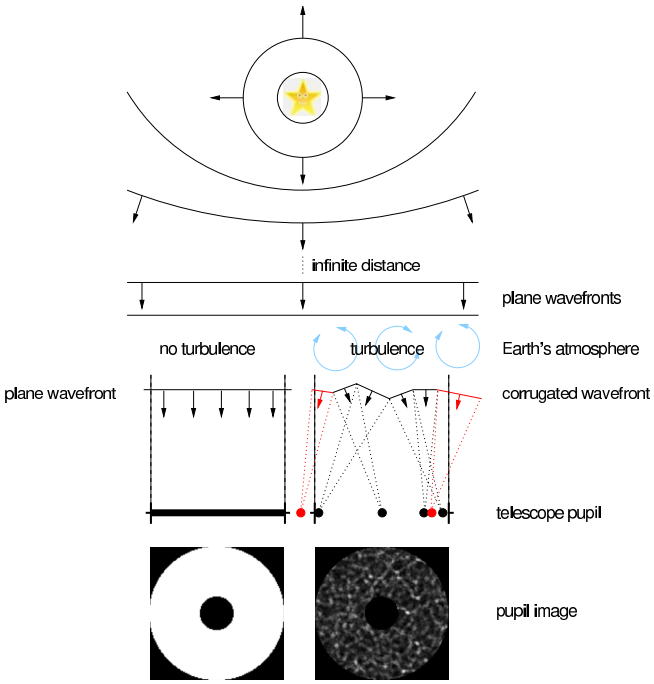

Figure 1.2: Diagram illustrating the principle of scintillation. Plane waves from the star at infinity appear flat at the top of Earth's atmosphere. In the absence of turbulence, the entire flux is collected by the telescope pupil. In the presence of a turbulent atmosphere, the wavefront passes through refractive index variations caused by changes in temperature and pressure. As the wavefront propagates down to the ground, the wavefront interferes with itself constructively and destructively resulting in a flying shadow pattern at the telescope pupil. At any one time, the configuration of the atmosphere may be such that either a little more or a little less of the starlight falls into the telescope pupil. This gives rise to intensity variations in the point-spread-function of the image. *Diagram from [102].*

uncertainties in the astrophysical parameters.

1.1 Thesis Synopsis

The layout of the thesis is as follows:

- Chapter 2 gives the theoretical background required for understanding the concepts of exoplanet transit, eclipse observations and atmospheric scintillation. This includes the description of the numerical and analytical methods for calculating the shape of the light curve for the transit and secondary eclipse and the description of the methods used for light curve fitting, which include the downhill simplex and Markov-Chain Monte Carlo Methods. The origins of atmospheric turbulence are described. The Kolmogorov turbulence model is presented and the theoretical predictions for the effect of scintillation are presented. The sources of noise on photometry are examined in detail.

- Chapter 3 explains the physical and mathematical framework behind the simulation of atmospheric turbulence used in chapters 4 and 5. The underlying theory of phase screen generation and optical propagation are presented. The theory for producing noise on the simulated images is described. The implementation of the simulation and the tests performed against theory are shown. The assumptions and limitations of the simulation are discussed.

- Chapter 4 presents an examination of the sources of noise on transit photometry through numerical simulation. The need for time-resolved turbulence measurements is presented. The verification of the simulation for longer exposure times is shown. The validity of combining scintillation noise and photon noise in the simulations is tested. The fractional noise contributions are compared for the case of the ULTRACAM instrument, with implications on photometric instruments in general. The magnitudes at which scintillation dominates are presented for different turbulence strengths, telescope diameters and wavelengths. The effect of scintillation noise on the uncertainties in the astrophysical parameters are investigated for several cases of exoplanetary systems through Markov-Chain Monte Carlo fitting, and generalised.

- Chapter 5 describes the process of aperture photometry. The concept of aper-

ture noise is introduced. The noise due to aperture photometry is investigated through simulated images. The photometry aperture size up to which aperture noise adds a source of noise is determined for different exposure times and turbulence strengths.

- Chapter 6 contains an observational study of the effect of scintillation on photometry. The principle of turbulence profiling using SCItillation Detection And Ranging (SCIDAR) is presented. The methods used for obtaining scintillation noise from SCIDAR measurements are described. SCIDAR measurements of scintillation noise are presented. These are compared to photometric time-series measurements from ULTRACAM and the $pt5m$ telescope.

- Chapter 7 presents the observations of the secondary eclipse of WASP-12b from the ground. The details of the observation, data reduction and analysis are presented. Details of the error estimation are given. The implications of the data on the astrophysics of WASP-12b are examined.

- Capter 8 provides the conclusions to this work.

Chapters 2 and 3 contain background material with the theory required for the subsequent chapters, which place this work in the wider context. Chapters 4, 5, 6 and 7 contain original work by the author. The material presented in chapter 7 has been published in Föhring et al. [47].

Chapter 2

Theory

In this chapter, the theory required for the rest of the thesis is given. This chapter consists of three main parts. The first part, in sections 2.1 and 2.2, concerns exoplanet transit photometry. Within this section, hot Jupiters are described and the fundamental concepts in transit photometry are given. The descriptions of the analytical and numerical equations for modelling transit and eclipse light curves, which are employed in chapters 4 and 7 are given. In the second part, the nature and origin of scintillation noise are discussed. The theoretical equations describing scintillation are presented. In the third part, the main sources of noise on photometry other than scintillation are described and discussed. This is followed by an explanation of the statistics used for handling noise. Finally, the causes and effects of systematics are discussed.

2.1 Hot Jupiters

Hot Jupiters are a class of exoplanet with masses close to or exceeding that of Jupiter, not composed of rock or other solid matter, on a very close orbit around their host star. These planets have very high surface temperatures (>1000K), due to their proximity of their star, between 0.015 and 0.5 AU, and orbital periods of typically of a few days. Figure 2.1 shows an artist's impression of a hot Jupiter. The majority of hot Jupiter orbits are circularised via tidal interactions due to the proximity to their host star (e.g. [118]). Their large size and proximity to their host make hot

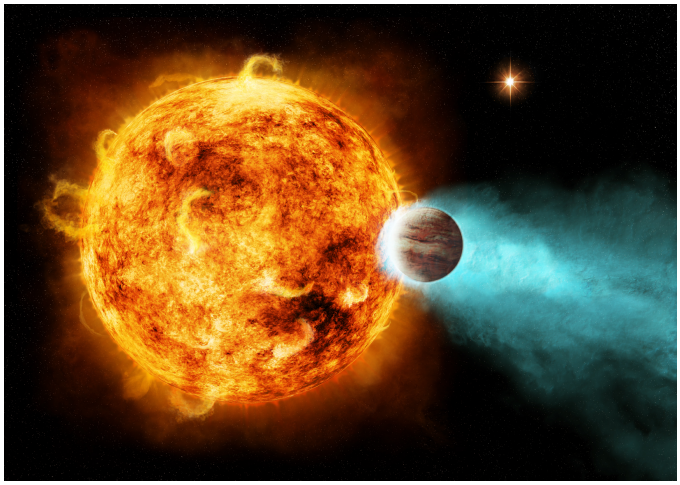

Figure 2.1: Artist's impression of a transiting hot Jupiter. Hot Jupiters are on close orbits around their stars and often display evaporation. *Image credit: NASA/CXC/M. Weiss.*

Jupiters prime candidates for detection and characterisation. Indeed, many of the first exoplanets to be discovered have been hot Jupiters [91; 16; 22; 59; 2]. The discovery of hot Jupiters has been a surprise, as their existence was not predicted by current planet formation theories, which advocate that planets form outside the *frost line*, the distance from the protostar where hydrogen compounds such as water, ammonia and methane can freeze [12; 80; 13]. The existence of these hot Jupiters invoke the need for planetary migration theories, such as *disk migration* (e.g. [79]) to account for the observations. An interesting property of hot Jupiters, including WASP-12b, is that many of them have radii exceeding predictions, even after the irradiation from the star is considered (figure 2.2). The reason for this is still not fully understood, although several theories have been proposed [5; 65; 46; 106].

2.2 Exoplanet Transit Photometry

A *primary eclipse* occurs when a planet passes in front of a star in the line of sight of the observer, causing a small reduction in the apparent brightness of the star. If the entire planet is in front of the stellar surface, this is referred to as a *transit*. An exoplanet transit occurs when a planet passes directly in front of a star and thereby

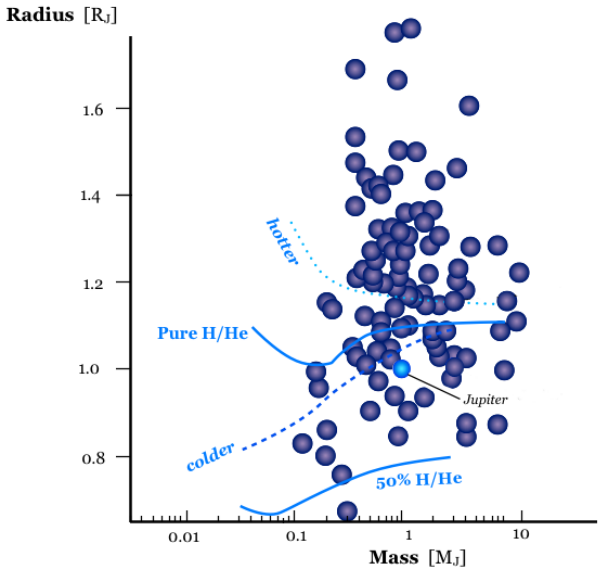

Figure 2.2: Mass-radius relation for hot Jupiters to date. The solid lines show model relations for planets with (50% H/He) and without a heavy core (Pure H/He), while the dashed lines show predictions for hot Jupiters closer or further from their star. Around half of the giant planets have radii that exceed predictions by any model. *Figure modified from [108], models from Jonathan Fortney.*

obscures a portion of the observed star's light, resulting in a small reduction in the apparent brightness of the star. A second decrease in flux can be measured as the planet moves around its orbit to pass behind the star, as the star blocks out the light from the planet's dayside. This is referred to as a *secondary eclipse*. If the planet is completely obscured during the secondary eclipse, this is termed an *occultation*. Figure 2.3 shows a schematic of a planet orbiting a star, and the measured flux at each phase of the planet's orbit. Typically, during the transit of a hot Jupiter, the measured drop in flux is around 1% of the total light of the system. In comparison, a secondary eclipse is around 10 times fainter, resulting in a decrease of $< 0.1 - 0.2\%$ of the total light.

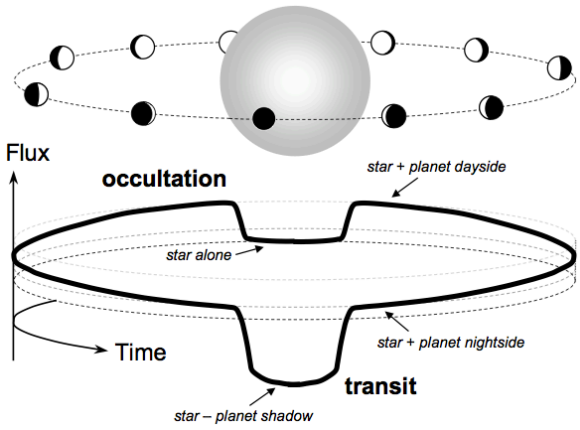

Figure 2.3: Schematic of a transiting exoplanet orbit. The planet blocks a fraction of the light from the star as it moves in front of it during a transit. After the transit, the total flux rises as the planet's dayside comes into view. During the occultation, the planet passes behind the star and a second drop occurs as the light from the dayside is blocked by the star. *Diagram from [142].*

2.2.1 Light Curve Shape

In this subsection we describe how the astrophysical properties mentioned in Chapter 1 relate to the shape of the light curve. We begin by describing the numerical and analytical models used for a general light curve shape for a uniform stellar disc. This is followed by presenting the details specific to the primary eclipse, including

the astrophysical parameters that can be obtained from the light curve shape and the effect of stellar limb darkening. Next, details relating to the secondary eclipse are given, which include the astrophysical parameters that can be obtained from the secondary eclipse, as well as the need for correcting for light travel time. Finally, the light curve model fitting processes used are described.

Numerical Calculation

Here we present the physically more intuitive numerical method employed in chapter 7 for calculating the light curve shape of a planet on a circular orbit. Consider an exoplanet, with radius R_p orbiting a star with radius $R_\star$, separated by a projected planet-star separation $R_{\rm cen}$ (see figure 2.4). The planet orbits the star at an inclination, i, with a semi-major axis, a, and an angular frequency $\omega = 2\pi/P$ radians/second, where P is the orbital period in seconds. After a time, t seconds, (where $t = 0$ is defined as the mid-transit, when orbital phase = 0) the planet sweeps out an angle ωt radians.

Applying Pythagoras' theorem, $R_{\rm cen}$ can be shown to be

$$R_{\rm cen} = a\sqrt{cos^2(i)cos^2(\omega t) + sin^2(\omega t)}. \tag{2.1}$$

Assuming the planet is passing between the Earth and the star, for each step in $R_{\rm cen}$ the area of the star obscured, A, is calculated. Figure 2.5 shows a diagram of the area obscured.

The area obscured, A, is calculated by considering a series of partial annuli, such as the one labelled s in figure 2.6.

The length of a half of the partial annulus is $s = r\theta$, where r is measured from the centre of the stellar disc and θ is the angle subtended by s. The total area eclipsed by the star is then given by

$$A = \int 2s\mathrm{d}r = 2\int r\theta \mathrm{d}r. \tag{2.2}$$

Using the cosine rule,

$$R_p^2 = r^2 + R_{\rm cen}^2 - 2rR_{\rm cen}\cos(\theta). \tag{2.3}$$

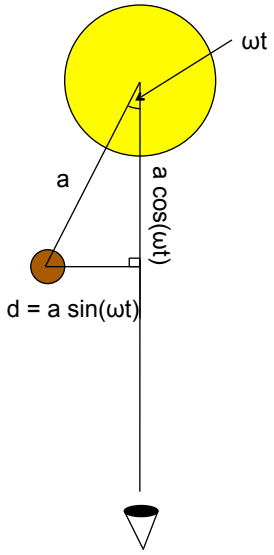

(a) Plan view

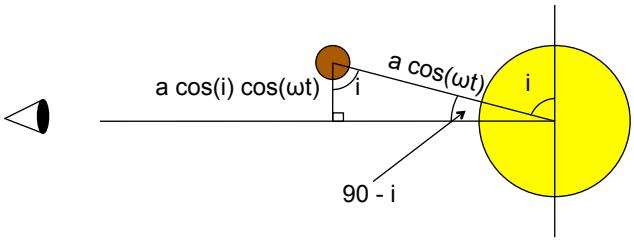

(b) Side view

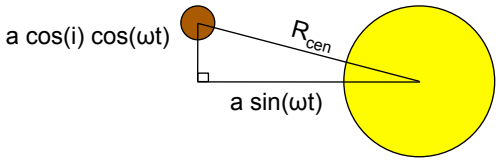

(c) Front view

Figure 2.4: Projected planet-star separation for numerical calculation of area obstructed during a transit. *Diagrams based on [121].*

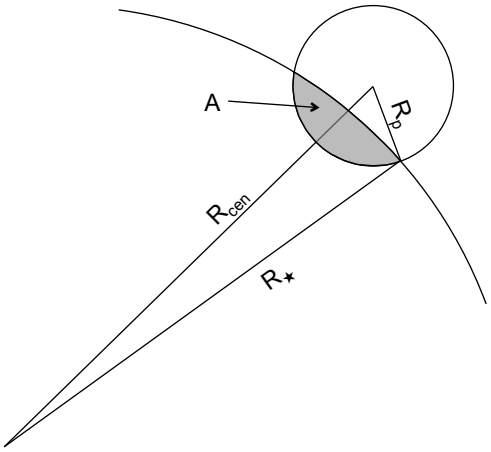

Figure 2.5: The geometry for calculating the area obscured during a transit. *Diagram based on [121].*

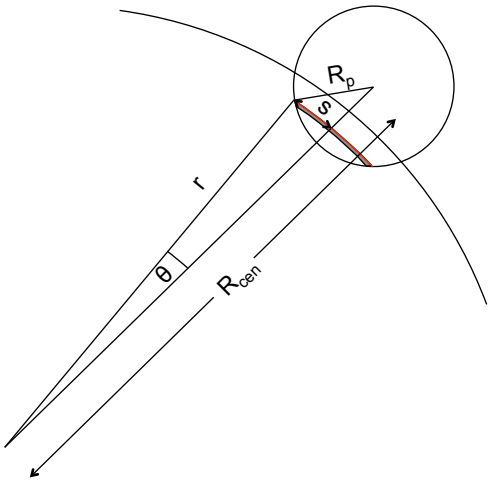

Figure 2.6: The geometry for numerically integrating to find the area obscured during a transit. *Diagram based on [121].*

Hence,

$$A = 2\int r\cos^{-1}\left(\frac{r^2 + R_{\text{cen}}^2 - R_p^2}{2rR_{\text{cen}}}\right)\mathrm{d}r. \tag{2.4}$$

The integration limits can be inferred from figure 2.5. When $R_{\text{cen}} > R_\star + R_p$, the whole planet is outside the stellar disk and the obscured area is zero. When $R_{\text{cen}} < R_\star - R_p$, the entire planet is within the stellar disc and the area obscured is πR_p^2. Between these two limits the planet is undergoing transit. For the purpose of the simulation, it is only necessary to loop from $R_{\text{cen}} = R_\star - R_p$ until $R_\star = R_{\text{cen}}$. This gives one half of the transit, and the entire transit is obtained through symmetry. For a stellar disc of uniform brightness, I_0, the area obscured is related to the fraction of flux lost, ΔF, simply as

$$\Delta F = I_0 A. \tag{2.5}$$

Figure 2.7 shows light curves generated through this method for orbital inclinations between 90° and 60°.

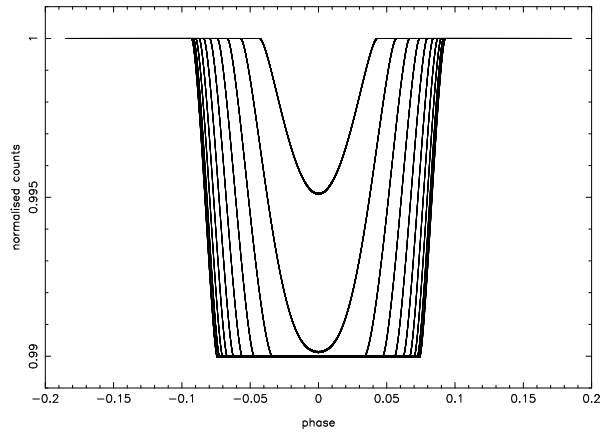

Figure 2.7: Light curves with varying inclination from 90° (outermost) and 60° in increments of 3° generated through through numerical integration for a planet crossing a star of uniform brightness, for a system with parameters $R_p = 0.7\times10^5$km, $R_\star = 7\times10^5$km, $R_p = 0.7\times10^5$km. At low inclinations the transit is partial, resulting in a rounded light curve. For higher values of inclination the light curve is flat.

Analytical Calculation

An analytical approach for calculating the area obscured is described by Mandel and Agol [88]. Consider the terms $z = d/R_\star$ and $p = R_p/R_\star$, as shown in figure 2.8. In this description, d is the distance between the star and planet centres as seen from the line of sight of the observer, $asin(\omega t)$, shown in figure 2.4 (a). As for the numerical calculation, outside of the transit, when $(1+p < z)$, the obscured area is 0, and when the star is fully occulted, $(z \leq 1-p)$, the obscured area $A = \pi R_p^2 = \pi R_\star^2 p^2$. The partially overlapping region, shown in green in figure 2.8 is obtained through geometry, and using the cosine rule:

$$\cos(\alpha) = \frac{p^2 + z^2 - 1}{2zp}, \tag{2.6}$$

and

$$\cos(\beta) = \frac{1 + z^2 - p^2}{2z}. \tag{2.7}$$

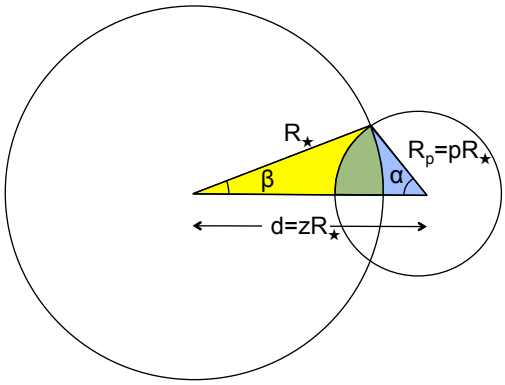

Figure 2.8: The geometry for analytically integrating to find the area obscured during a transit. Half of the area obscured, shown as the overlap of the yellow and blue arcs, is calculated from the sum of the two arcs minus the triangle formed through $R_p R_\star d$. *Diagram adapted from [88].*

The area obscured, A, is calculated as the sum of twice the areas of the two overlapping sectors with radius $R_\star$ and R_p respectively, and subtracting twice the area of the triangle formed through $R_\star$, $zR_\star$ and R_p (see figure 2.8),

$$\frac{A}{2} = \frac{R_\star^2 \beta}{2} + \frac{R_p^2 \alpha}{2} - \frac{z R_\star^2}{2} sin(\beta). \tag{2.8}$$

Rearranging equation 2.7 using a trigonometric identity gives:

$$sin(\beta) = \frac{\sqrt{(4z^2 - (1 + z^2 - p^2)^2)}}{2z}. \tag{2.9}$$

The obscured area is then found analytically from substituting equation 2.9 into 2.8 to be:

$$A = R_\star^2 \left(p^2 \alpha + \beta - \frac{\sqrt{4z^2 - (1 + z^2 - p^2)^2}}{2} \right). \tag{2.10}$$

To summarise, the ratio of the obscured to unobscured flux for a uniform source, $\Delta F/F$, is:

$$\Delta F/F = \begin{cases} 0 & 1+p < z \\ \frac{1}{\pi}\left[p^2\alpha + \beta - \frac{\sqrt{4z^2-(1+z^2-p^2)^2}}{4}\right] & \mid 1-p \mid < z \leq 1+p \\ p^2 & 1-p \geq z. \end{cases} \tag{2.11}$$

2.2.2 Primary Eclipse

Here we describe the shape of the primary eclipse light curve and describe the astrophysical parameters that can be obtained from it.

Limb Darkening

The main difference between primary and secondary eclipses is the presence of limb darkening during a primary eclipse, resulting in the light curve shape to appear rounded, rather than flat (see figure 2.9).

Limb darkening refers to the drop in intensity of the stellar disc moving towards the edges, caused by the decreasing density and temperature of the star with radius. Limb darkening arises because the Sun is not a solid, but rather a plasma, and photons emitted at different depths have a probability of being scattered or reabsorbed depending on the distance they travel. Figure 2.9 shows a broad-band optical image of the Sun, illustrating the drop in intensity and reddening of the disc towards the edges.

The probability of a photon being scattered or absorbed when passing through a medium is determined by the *optical depth*, τ. For light of a given wavelength travelling through a medium, the optical depth is defined as

$$\tau = \int_0^l \rho\kappa\cos(\gamma)\mathrm{d}l', \tag{2.12}$$

where ρ is the density of the medium, κ the opacity at the given wavelength, γ the angle to the normal and $\mathrm{d}l'$ the optical path. The observed intensity, I, after a given path as a fraction of the intensity at the source , I_0, is

$$I/I_0 = e^{-\tau}. \tag{2.13}$$

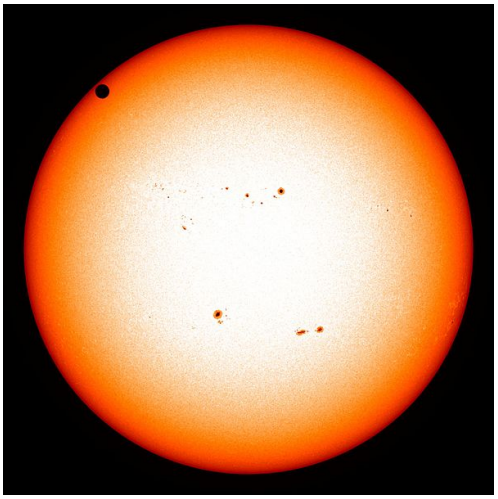

Figure 2.9: NASA image of the Sun in visible light taken during the 2012 transit of Venus showing the drop in intensity towards the edge of the disc. This effect is called limb darkening. *Image credit: NASA/SDO, HMI.*

Compared to light emitted normal to the line of sight of the observer from the star at a given depth h, light emitted near the limbs needs to travel an extra distance through the atmosphere, $\frac{h}{cos(\gamma)}$, depending on the angle between the normal to the line of sight of the observer, γ, illustrated in figure 2.10.
As the optical depth increases towards the limb of the star, the limb of the star appears dimmer. The exact form of limb darkening is different for each star and cannot be directly measured. Because of this, limb darkening functions have to be fitted individually to each star. The effect of limb darkening on the light curve is expressed in functions of $\mu = cos(\gamma)$.

The most widely used polynomial functions are the non-linear laws of Claret [27],

$$\frac{I(\mu)}{I_0} = 1 - u_1(1 - \mu^{1/2}) - u_2(1 - \mu) \tag{2.14}$$

and a polynomial (quadratic) law

$$\frac{I(\mu)}{I_0} = 1 - u_1(1 - \mu) - u_2(1 - \mu)^2, \tag{2.15}$$

where u_1 and u_2 are the limb darkening coefficients, dependent on effective temper-

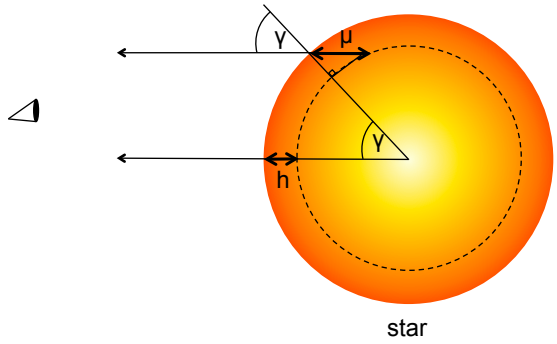

Figure 2.10: Cross section of a star indicating the path travelled for photons emitted from the centre of the stellar disc and at an angle γ to the line-of-sight of the observer. Both photons are emitted at a depth h, but the photon emitted at an angle γ travels an extra distance $\mu = h/cos(\theta)$ making it more likely to be absorbed.

ature, luminosity class and metallicity. Copperwheat et al. [29] have not found any difference in the quality of the fit between the two laws presented here, and in our light curve models in Chapter 4 we chose to adopt the second model.

The model light curve for the transit is thus numerically obtained by stepping through time and determining the instantaneous projected separation $R_{\rm cen}$, then calculating the ratio of obscured to unobscured flux. When including limb darkening, the flux from the star is calculated by multiplying by the chosen limb darkening function at each iteration step, before the ratio is calculated. Figure 2.11 shows the light curves of the same system as in figure 2.7, but in the presence of limb darkening in the V-band. Analytical equations for the light curve shape for a quadratic limb-darkening law have also been obtained by Mandel and Agol [88], which is implemented directly in the simulations in Chapter 4.

Science from the Primary Eclipse

A great wealth of information can be gained from the shape of the transit light curve, as mentioned previously in Chapter 1. Here, the details of these are presented. There are four primary observables that characterise the light curve. These are the transit depth, ΔF, the total transit duration t_T and the fully occulted transit time, i.e. the "flat" part of the transit t_F and the period, P. These can be used to derive five

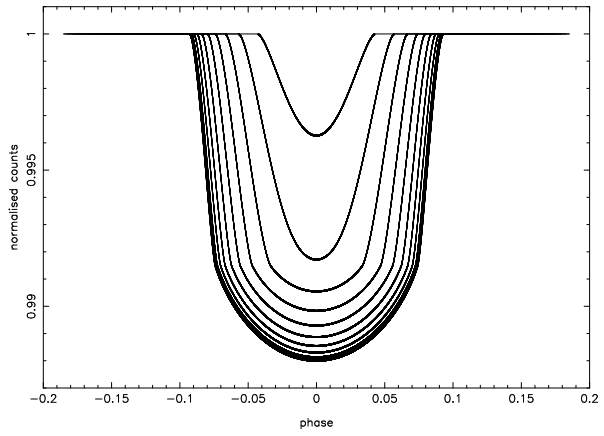

Figure 2.11: Light curves with varying inclination from 90° (outermost) to 60° in increments of 3° generated through through numerical integration for a planet crossing a star with limb darkening, with parameters $R_p = 0.7 \times 10^5$km and $R_\star = 7 \times 10^5$km. Limb darkening causes the shape of the bottom of the in-transit light curve to become rounded.

(degenerate) physical parameters: R_p, $R_\star$, i, a and $M_\star$, the stellar mass.

For the primary eclipse, the transit depth is

$$\Delta F \simeq \left(\frac{R_p}{R_\star}\right)^2, \tag{2.16}$$

which simply arises from the ratio of the projected disks of the planet and star. For a circular orbit, the parameters a and $\cos(i)$ are obtained from [123]:

$$\sin(t_T\pi/P) = \frac{R_\star}{a}\left(\frac{[1+(R_p/R_\star)]^2 - [(a/R_\star)\cos(i)]^2}{1-\cos^2(i)}\right)^{1/2} \tag{2.17}$$

$$\frac{\sin(t_F\pi/P)}{\sin(t_T\pi/P)} = \frac{([1-(R_p/R_\star)]^2 - [(a/R_\star)\cos(i)]^2)^{1/2}}{([1+(R_p/R_\star)]^2 - [(a/R_\star)\cos(i)]^2)^{1/2}}. \tag{2.18}$$

In addition to these three geometrical equations, the degeneracy between the five parameters can be broken via Kepler's third law:

$$P^2 = \frac{4\pi^2 a^3}{G(M_\star + M_p)}, \tag{2.19}$$

and the stellar mass-radius relation

$$R_\star = mM_\star^q, \tag{2.20}$$

where m is the constant coefficient for each stellar sequence, such as main sequence, giants etc., and for each stellar sequence, q describes the power law of the sequence, most frequently taken as $q = 0.8$ for F-K main sequence stars [31]. Thus the radius of the star can be obtained through spectral classification.

2.2.3 Secondary Eclipse

The secondary eclipse provides an estimate of the planet's day side equilibrium temperature and orbital eccentricity. Here we describe how these can be obtained from the light curve.

Day Side Equilibrium Temperature

The planet's day side equilibrium temperature is obtained from the depth of the secondary eclipse, which corresponds to the amount of light lost by the system, given by ΔF.

In the Rayleigh-Jeans limit, ΔF, approximates to [21]:

$$\Delta F = \frac{T_p}{T_\star}\left(\frac{R_p}{R_\star}\right)^2, \tag{2.21}$$

where T_p and $T_\star$ are the temperatures of the planet and star respectively.

Here we present how the change in flux is determined from the fractional change in the projected area of the system obscured, ΔA.

Before the transit, the total area observable is the sum of the projected area of the star, $A_\star$, and the projected area of the planet, A_p. During the ingress and egress, we see $A_\star + (A_p - A)$, and during mid-transit we only see $A_\star$. Figure 2.12 summarises this geometry.

For the simple mid-transit case, when the entire planet is obscured by the star, the fractional change in the area obscured $\Delta A_{\text{total}} = \frac{(A_\star + A_p) - A_\star}{(A_\star + A_p)}$. To obtain ΔF_{total},

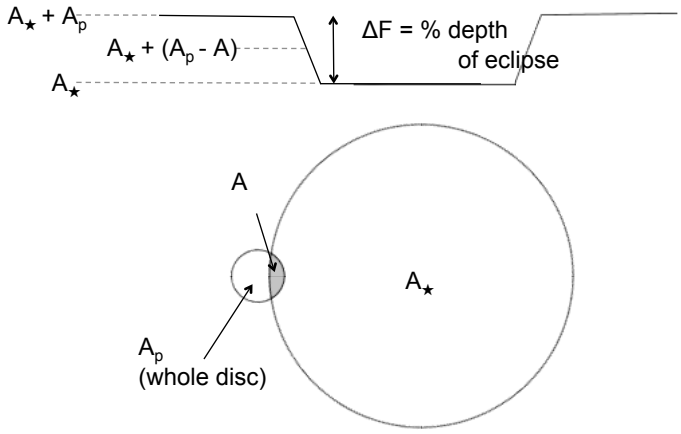

Figure 2.12: The geometry for calculating the fraction of flux obscured during the secondary eclipse.

let the flux emitted from the star be $F_\star$ and the flux of the planet F_p. Thus,

$$\Delta F_{\text{total}} = \frac{A_p F_p}{A_\star F_\star + A_p F_p}. \tag{2.22}$$

Rather than fitting the secondary eclipse depth when fitting the light curve, we fit a physically more intuitive term, x, defined as the ratio of the flux emitted per unit area of the star to the planet, so that $xF_p = F_\star$. This gives $\Delta F_{\text{total}} = \frac{A_p F_p}{A_\star x F_p + A_p F_p}$. Thus,

$$\Delta F_{\text{total}} = \frac{A_p}{A_\star x + A_p}. \tag{2.23}$$

To use this equation, knowledge of the values of A_p and $A_\star$ is needed. These follow from from R_p and $R_\star$ obtained from transit measurements.

For the case when the planet is undergoing ingress and egress, the change is given by the total projected area before eclipse minus the area during the eclipse, $(A_\star + A_p) - (A_\star - [A_p - A])$. From this, the fractional change in the area obscured $\Delta A_{\text{partial}} = \frac{A_\star + A_p - A_\star - A_p + A}{A_\star + A_p}$. As for the previous case, multiplying by the flux yields

$$\Delta F_{\text{partial}} = \frac{A}{A_\star x + A_p}. \tag{2.24}$$

The normalised model light curve is given by $1 - \Delta F$ (figure 2.12).

To summarise, the ratio of the obscured to unobscured flux, $\Delta F/F$, for the secondary eclipse can be expressed, similarly to the primary eclipse, as:

$$\Delta F/F = \begin{cases} 0, & if 1 + J < z \\ \frac{1}{\pi}\left[J^2\alpha + \beta - \frac{\sqrt{4z^2-(1+z^2-J^2)}^2}{4}\right], & |1-J| < z \leq 1+J \\ J^2 & 1 - J \geq z, \end{cases} \quad (2.25)$$

where J is defined as $J = \sqrt{\frac{p^2}{X+p^2}} = \sqrt{\Delta F}$, and $p = R_p/R_\star$.

The observed raw differential light curve however is not normalised to one, but has an offset according to the relative intensity of the target and comparison(s). For this reason, in order to fit the observed light curve, the normalised model light curve needs to be multiplied by a background model, b, ie.

$$\text{light curve} = b(1 - \Delta F). \quad (2.26)$$

The background is simply a fit, $b = c1 + (c2 \times \text{airmass})$, where $c1$ accounts for the offset and $c2$ corrects for any extinction changes due to differing colours of the target and comparison(s).

Eccentricity

The timing of the secondary eclipse reveals information about eccentricity of the exoplanet's orbit. The orbital phase of the midpoint of an exoplanet's secondary eclipse with respect to the primary transit is dependent only on the eccentricity, e, and the argument of the periapsis, ω, as $e\cos(\omega)$. A precise measurement of the phase thus gives a well defined, but degenerate, constraint on the two parameters. On its own, the the phase midpoint of the secondary eclipse is used to obtain a minimum eccentricity, and give a strong indication of whether the orbit is circular or elliptical. Individual values for e and ω can be obtained from the phase midpoint of secondary eclipse by combining with other methods, such as radial velocity measurements.

When fitting a light curve to the secondary eclipse, the phase midpoint, ϕ, has to be a free parameter. The phase midpoint of the secondary eclipse will be offset due to light travel time (Rømer delay) and any orbital eccentricity. In order to calculate the eccentricity, the effect of light travel must be corrected for. The light travel time is calculated as follows:

Consider the orbital geometry of the planet with respect to the star at primary transit and secondary eclipse (figure 2.13). For simplicity, for this section we define a phase, ϕ', which is zero at the ingress. At $t = 0$, a photon is just obscured by the planet at the start of the transit ingress originating from a star at a distance, d, from the observer. The transit is observed to start at time $T_{\text{transit}} = d/c$ as viewed from Earth, where c is the speed of light. At $t = 0.5 \times P$, a second photon leaves the planet, just at the moment it is eclipsed by the limb of the star. Thus the secondary eclipse will start at time $T_{\text{sec}} = 0.5 \times P + 2a/c + d/c$ after the transit, as seen from Earth. The separation in time between transit and eclipse, i.e. time between the first and second of the above photons arriving to Earth is

$$T_{\text{transit}} - T_{\text{sec}} = 0.5P + 2a/c. \tag{2.27}$$

This effect, known as the Rømer delay, must be corrected for when fitting the model light curve.

2.2.4 Light Curve Fitting

The two methods used for light curve fitting in this thesis are the Downhill Simplex method and the Markov chain Monte Carlo method, both of which involve a process of chi-squared minimisation to determine the best fit to the data. χ^2 is a statistical quantity commonly used to gauge the goodness of fit of a model with predicted values E_i, to a set of individual measurements with known errors $O_i \pm \sigma_i$. It is defined as:

$$\chi^2 = \sum_i \frac{(O_i - E_i)^2}{\sigma_i^2}. \tag{2.28}$$

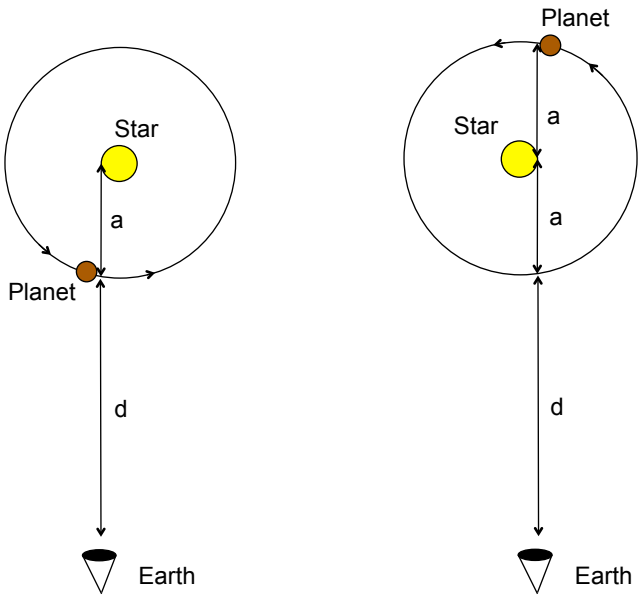

(a) View of orbit at the start of transit ingress. $\phi' = 0$.

(b) View of orbit at the start of secondary eclipse ingress. $\phi' = 0.5$.

Figure 2.13: Diagrams illustrating that during secondary eclipse, an extra factor of 2a/c needs to be added when timing the difference between the transit and secondary eclipse ingress. Equivalently, this factor needs to be added to the centre of the transit when predicting the centre of the secondary eclipse, since their durations must be equal, due to the extra distance light has to travel.

Downhill Simplex Method

We employ the Downhill Simplex method [97], also called the Nelder-Mead method or the amoeba method, which is a commonly used technique for finding the minimum of a function in multi-dimensional parameter space, adapted from Press et al. [111]. A *simplex* is an N_d dimensional geometrical figure consisting of N_d+1 vertices. In the case of a secondary eclipse, we fit four parameters, the eclipse depth, x (see section 2.2.3), the phase offset, ϕ, and two coefficients of airmass, c_1 and c_2, and so the simplex is a polygon with $N_d = 4$ dimensions. The basic idea is to move and change the shape of the simplex by a series of reflections, expansions and contractions, until it converges onto a minimum with the required level of tolerance.

To start the simplex, an initial guess of the range of the maximum and minimum of the parameters is given. The vertices of the initial simplex are defined by creating $N+1$ points starting from the minimum value for the point $P_{\rm min}$ in equal increments up to the maximum, $P_{\rm max}$:

$$P_i = P_{\rm min} + i \times (P_{\rm max} + P_{\rm min})/N_d, \tag{2.29}$$

where i is an integer between 1 and $N_d + 1$.

The function $f(P_i)$, given by equations 2.11 and 2.25 in section 2.2.3, is evaluated at each vertex, and the chi-squared of the fit is calculated. The first step is to rearrange the points $P_1, P_2, ...P_{n+1}$ so that $\chi^2(f(P_{n+1})) > \chi^2(f(P_2)) > \chi^2(f(P_1))$. A trial point, P_r, is generated by *reflection* across from the point with the highest value of χ^2, P_{n+1}, as

$$P_r = \bar{P} + \alpha(\bar{P} - P_{n+1}), \tag{2.30}$$

where $\bar{P} = \sum_i P_i/(N_d + 1)$ is the centroid and $\alpha = 1$ is the coefficient of reflection. The function is then evaluated at this point, and $\chi^2(f(P_r))$ is calculated. There are three possible outcomes:

1. If the chi-squared of the function at the new point is neither the best nor the worst, $\chi^2(f(P_1)) < \chi^2(f(P_r)) < \chi^2(f(P_n))$, P_n is replaced by P_r.

2. If the chi-squared of the function at P_r is the best, $\chi^2(f(P_r)) < \chi^2(f(P_1))$, then the direction of reflection is good and the next point, P_e is generated by *expansion*

as

$$P_e = P_r + \gamma(P_r - \bar{P}), \tag{2.31}$$

where $\gamma = 2$ is the coefficient of expansion. This is equivalent to trying an additional extrapolation by a factor 2. If $\chi^2(f(P_e)) < \chi^2(f(P_r))$, P_{n+1} is replaced by P_e, otherwise the expansion has failed and P_{n+1} is replaced by P_r.

3. If the chi-squared of the function at P_r is worse than the second-highest, $\chi^2(f(P_r)) > \chi^2(f(P_n))$, the polytope is assumed to be too large and the next new point, P_c, is generated by *contraction*

$$P_c = \bar{P} + \beta(P_{n+1} - \bar{P}), \tag{2.32}$$

where $\beta = 0.5$ is the contraction coefficient. If $\chi^2(f(P_c)) < \chi^2(f(P_{n+1}))$ the contraction has succeeded and P_{n+1} is replaced by P_c, otherwise the contraction is repeated.

This process is repeated until the maximum number of iterations is obtained or the change in the value of chi-squared between successive iterations is less that the required tolerance. For our amoeba routine, the maximum number of iterations is 300 and the tolerance is 1×10^{-6}. We also perform a second pass, with the claimed solution as one of the simplex vertices, to ensure the amoeba is not stuck in a local minimum.

Markov Chain Monte Carlo

The Markov chain is a stochastic process in Bayesian statistical modelling with the property that at a time t in the series, the probability of making a transition to any new state is dependent only on the current state of the process, X_t and is conditionally independent of the sequence of events that preceded it. The method for use in astrophysics is described in detail in Tegmark et al. [133] and applied to transit light curves in Holman et al. [63]. A Markov chain performs a random walk about the parameter space and eventually finds the region with the lowest χ^2. Once the chain converges, the sampling of the distribution of previous states is used to approximate the distribution of interest. The sequence of states is called the *chain*. The probability of moving to other points in the state space are described by a *transition kernel*. A typical transition kernel applies a Gaussian random number to

each parameter value, scaled by a set step size. If the new point has a lower χ^2 than the previous point, the jump is executed. If the new point has a higher χ^2, the jump is executed with a probability $\exp(-\Delta\chi^2/2)$. For the MCMC analysis performed in chapter 4, we employed the python MCMC fitting package pymc.

2.3 Seeing and Scintillation

Atmospheric turbulence causes aberrations in starlight with two important effects: seeing and scintillation. Seeing arises from phase fluctuations caused by refractive index variations in the atmosphere. Scintillation, however, arises as a second order effect as a result of the perturbed wavefront propagating to the telescope. In this section, we examine the theory of how seeing and scintillation arise, and examine their effects.

2.3.1 Atmospheric Turbulence and Seeing Theory

Atmospheric optical turbulence arises in a fluid when both dynamical turbulence and a refractive index gradient are present [134]. Processes which give rise to dynamical turbulence include: drag encountered by the air flow at the Earth's surface resulting in wind shear, convection due to differential heating, changes in temperature and velocity fields arising from changes of state, interaction of air masses with atmospheric fronts and obscuration of the air flow. The Earth's atmosphere is a mixture of gasses retained by gravity. It has no direct boundary, but gradually thins out until it reaches space. About 80% of the mass of the atmosphere is contained in the lowest $\sim$ 15km around the Earth, called the troposphere. This is where almost all weather phenomena occur. Temperatures decrease with height in the troposphere, until it reaches the next layer, the stratosphere, where the temperature begins to increase again with altitude due to heating from the Sun (thermal inversion). The boundary between the troposphere and the stratosphere is called the *tropopause*. It varies in height between 8–16km depending on the latitude and season. The majority of atmospheric scintillation arises from the high velocity turbulence around the tropopause (figure 2.14).

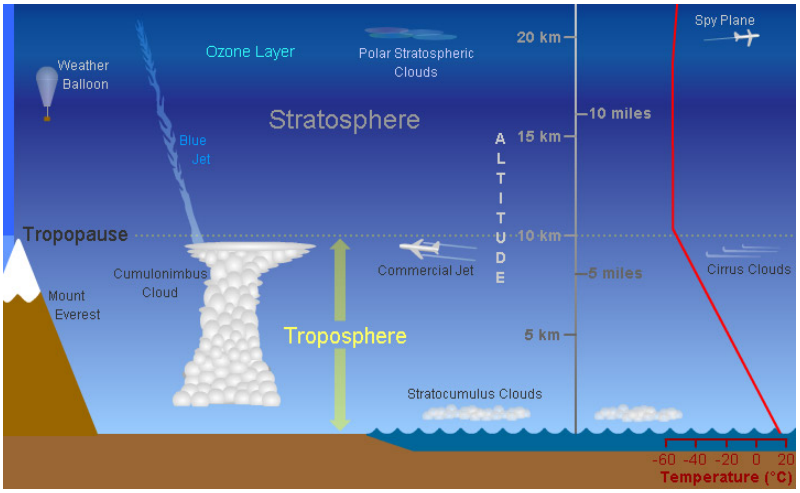

Figure 2.14: Diagram of the lower atmosphere containing the troposphere. Most scintillation arises from fast moving turbulence around the boundary between the troposphere and stratosphere. *Image credit: [120].*

The condition for mechanical turbulence is described by the Reynolds number, the ratio between the inertial and viscous forces

$$R_e = \frac{vl}{\nu}, \tag{2.33}$$

where v is the average velocity of the fluid, l the characteristic size and ν the kinematic viscosity. Laminar fluid motion occurs for lower values of R_e, whereas values of $R_e \gg 2000$ result in turbulent flow. Due to the low kinematic viscosity of air, the Reynolds number of the atmosphere always exceeds this critical value, allowing for the development of dynamical turbulence [82].

The atmosphere consists of layers of air with different refractive indices arising primarily from varying temperatures and to a lesser extent the water vapour content. Dynamical turbulence causes mixing of these layers, which leads to refractive index fluctuations. Light from astronomical objects arrives as flat wavefronts from space, until it encounters the refractive index fluctuations in the atmosphere. These fluctuations create random phase delays in different parts of the wave, resulting in a distorted wavefront. The geometric optical interpretation of this is that the phase perturbations act as positive or negative "lenses", changing the curvature of the wavefront.

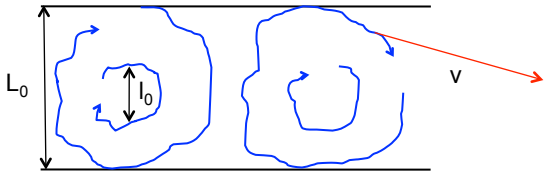

Figure 2.15: Kolmogorov "cascade". A turbulent layer of thickness L_0 moves between two zones of laminar flow. An eddy with characteristic size l_0 moves with a characteristic velocity v within this regime.

The most commonly used model used to describe the nature of the wavefront perturbations is the *Kolmogorov Model*, developed by Tatarski [131], based on the work of Kolmogorov [73, 74]. Observational evidence for the validity of the Kolmogorov model has been made by e.g. [98].

Consider a turbulent layer of thickness L_0 between two laminar zones (figure 2.15). In the Kolmogorov turbulence model, energy enters the flow at the *outer scale* length L_0. The eddies formed break into smaller eddies transporting part of their kinetic energy, until at about $R_e \approx 1$ it is lost by viscous dissipation at the *inner scale*, l_0. This is known as a *Kolmogorov cascade*. A mean value for the outer scale, $L_0 \approx 20$m, has been obtained by Wilson [139] and Ziad et al. [145], and l_0 has a typical value of around a few millimetres [99].

The velocity fluctuations caused by atmospheric turbulence can be described by a structure function, $D_v(\mathbf{r})$,

$$D_v(\mathbf{r}) = \langle (\mathbf{v}(\mathbf{r}') - \mathbf{v}(\mathbf{r}' + \mathbf{r}))^{\mathbf{2}} \rangle, \tag{2.34}$$

defined as the mean squared velocity difference between two points separated by distance $\mathbf{r}$. The angled brackets represent the ensemble average.

For small-scale fluctuations with size $l_0 < r < L_0$ viscous forces can be ignored and the behaviour of the turbulence is independent of the scale and geometry of the flow. This is called the *inertial range*. Within this range the structure function of the velocity fluctuations obeys a power law [134]

$$D_v(r) = C^2 r^{2/3}, \tag{2.35}$$

where the separation, $r = |\mathbf{r} - \mathbf{r}'|$, with $\mathbf{r}$ a 3-d vector, and C^2 the constant of proportionality.

In the Earth's atmosphere, both temperature and humidity vary with altitude. Mechanical turbulence causes mixing of air from different altitudes, causing variations in temperature and humidity of similar scale to the underlying turbulence. (For a medium in thermal equilibrium, optical turbulence does not arise as a result of physical turbulence.) The temperature fluctuations affect the density of air, there by causing changes in the refractive index, n. The refractive index of air changes with temperature, T (Kelvin) and pressure, p (millibars) as

$$(n-1)10^6 = 77.6p/T. \tag{2.36}$$

As local pressure fluctuations are negligible compared to the temperature fluctuations, the refractive index fluctuations are primarily caused by the temperature variations, and so can be expressed as

$$D_n(r) = C_n^2 r^{2/3}, \tag{2.37}$$

where $C_n^2(h)$ is the refractive index structure function, which relates to the refractive index fluctuations.

The magnitude of the modulation of optical phase of starlight propagating through the turbulence, ϕ, is described by the *phase structure function*, D_ϕ,

$$D_\phi(\mathbf{r}) = \langle [\phi(\mathbf{r}') - \phi(\mathbf{r}' + \mathbf{r})]^{\mathbf{2}} \rangle. \tag{2.38}$$

In the Kolmogorov turbulence regime in the near-field approximation (see section 3.3), this is given by [116]

$$D_\phi(\mathbf{r}) = 2.914\ k^2 \sec(Z)\ r^{5/3} \int_0^\infty C_n^2(h)\ dh \tag{2.39}$$

$$= 6.88 \left(\frac{|\mathbf{r}|}{r_0} \right)^{5/3}, \tag{2.40}$$

where the turbulence is described by $C_n^2(h)$ as a function of height, h, viewed at a zenith angle Z, $k = 2\pi/\lambda$ is the wavenumber and r_0 is the Fried Parameter [49], [117]:

$$r_0 = \left(0.423\ k^2 \sec(Z)\ \int_0^\infty C_n^2(h)\ dh\right)^{-3/5}. \tag{2.41}$$

r_0 is defined as the region of the wavefront over which the root mean square phase variations are less than 1 rad^2. The physical interpretation of the Fried parameter r_0, is that it is the critical pupil diameter under which a telescope becomes diffraction limited.

As r_0 is dependent on wavelength as $\lambda^{6/5}$, the wavelength at which r_0 is measured always be specified for seeing measurements. In our simulations, a wavelength of 0.55 μm is adopted as a standard.

The angular distance in the sky over which the turbulence pattern is statistically the same is defined by the *isoplanatic angle*, θ_0. In terms of r_0,

$$\theta_0 = 0.314\frac{r_0}{h_{\text{eff}}}, \tag{2.42}$$

where h_{eff} is the effective turbulence altitude

$$h_{\text{eff}}^{5/3} = \frac{\int_0^\infty C_n^2(h)h^{5/3}dh}{\int_0^\infty C_n^2(h)dh}. \tag{2.43}$$

The timescale of variation of turbulence is expressed by the *coherence time*,

$$\theta_0 = 0.314\frac{r_0}{v_0}, \tag{2.44}$$

where v_0 is the average velocity of the turbulent layer,

$$v_0^{5/3} = \frac{\int_0^\infty C_n^2(h)V^{5/3}dh}{\int_0^\infty C_n^2(h)dh}, \tag{2.45}$$

and V denoting the velocity profile.

2.3.2 Effects of Turbulence (1): Seeing

The Fried Parameter determines the *full width at half maximum* (FWHM) in arcseconds of the seeing disc expected to be produced by a larger telescope, assuming it is free of errors due to poor focus, optics and tracking. Starlight is distorted by the atmosphere to produce a rapidly altering *speckle image* at the telescope focus, which

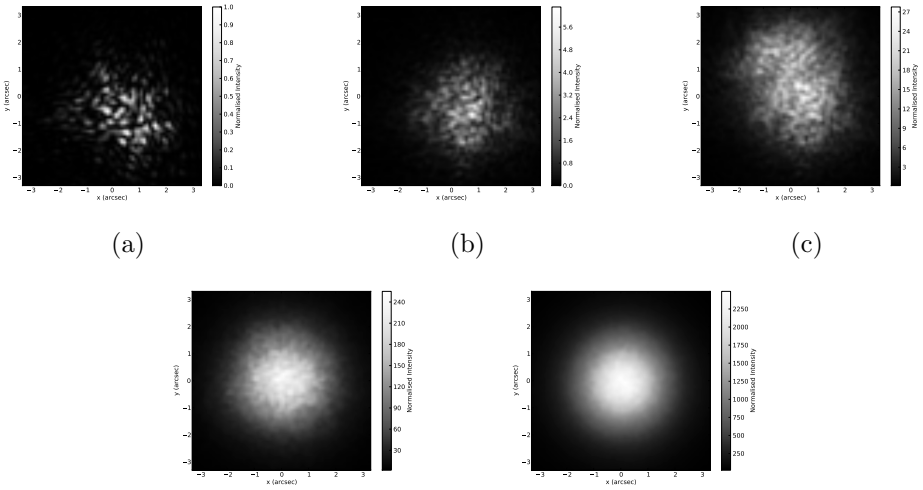

Figure 2.16: Speckle images averaging to produce a Gaussian PSF. Linearly adding instantaneous speckle images simulates how a Gaussian PSF is is built up from many instantaneous realisations of speckle images when a number of images are averaged that correspond to the length of typical exposure time. The images have simulated exposure times of 1ms, 10ms, 1s, 10s and 100s between (a) - (e) respectively.

averages approximately to a Moffat PSF [94] on longer exposure (1 - 100s). For a seeing-limited telescope, the angular diameter of the PSF is estimated numerically to be [41]:

$$\varepsilon_{FWHM} = 0.976\frac{\lambda}{r_0}. \tag{2.46}$$

Figure 2.16 shows how instantaneous speckle images average to a Moffat PSF over longer exposure times.

At good observing sites, ε is in the range of 0.5 to 2 arcsec [141]. In the absence of turbulence, or if the telescope diameter, D, is smaller than r_0, ε_{FWHM} is simply the size of the diffraction-limited Airy disc:

$$\varepsilon_{FWHM} = 1.028\frac{\lambda}{D}. \tag{2.47}$$

2.3.3 Effects of Turbulence (2): Scintillation

High altitude optical turbulence will cause the complex wavefront of the light from a star to fluctuate in both phase (seeing) and amplitude (scintillation). As the

perturbed wavefront propagates to the ground, interference of the light wave with itself creates a "flying shadow" pattern seen in the pupil. Figure 2.18 shows a simulation of the distribution of intensity of starlight at the telescope aperture. In a real atmosphere, the instantaneous shadow pattern will change due to the evolution of the turbulent layer. However, the timescale of this change is long compared to the crossing time of the layer over the aperture, $t_{\text{cross}} = D/V_{\perp}$, where $V_{\perp}$, is the horizontal windspeed of the turbulent layer. This scenario, in which the atmosphere is taken to be a fixed pattern translating, is known as in accordance with Taylor's hypothesis of frozen flow (see section 3.3).

The characteristic scale of the structures in the scintillation pattern ("flying shadows") is determined by the *Fresnel radius*,

$$r_F \approx (\lambda h)^{1/2}. \tag{2.48}$$

The Fresnel radius defines the size of the atmospheric "lenses" created due to turbulence, as well as the size of the flying shadows seen in the pupil. While both the strength of the turbulence, defined by $C_n^2(h)$, and the turbulence height determine the magnitude of the intensity fluctuations, the spatial scale, r_F, of the fluctuations is only dependent on h. Figure 2.17 shows the effect of increasing the height of the turbulent layer on the pupil image through simulation. As the wind moves this pattern across the pupil, the patches of higher and lower intensity moving into and out of the telescope pupil result in the intensity variations seen in the image plane. This same effect is registered by the naked eye as "twinkling". The resulting image intensity variations caused by the motion of the flying shadow pattern is shown in figure 2.18 (e).

A statistical way of quantifying scintillation is through the *scintillation index*, σ_I^2:

$$\sigma_I^2 = \sum \frac{\langle I^2 \rangle - \langle I \rangle^2}{\langle I \rangle^2}, \tag{2.49}$$

defined as the normalised variance of the intensity in the image, I, where $\langle\rangle$ denotes the time average.

For small telescope diameters, $D \ll r_F$, the scintillation index is determined using wave optics [116] as:

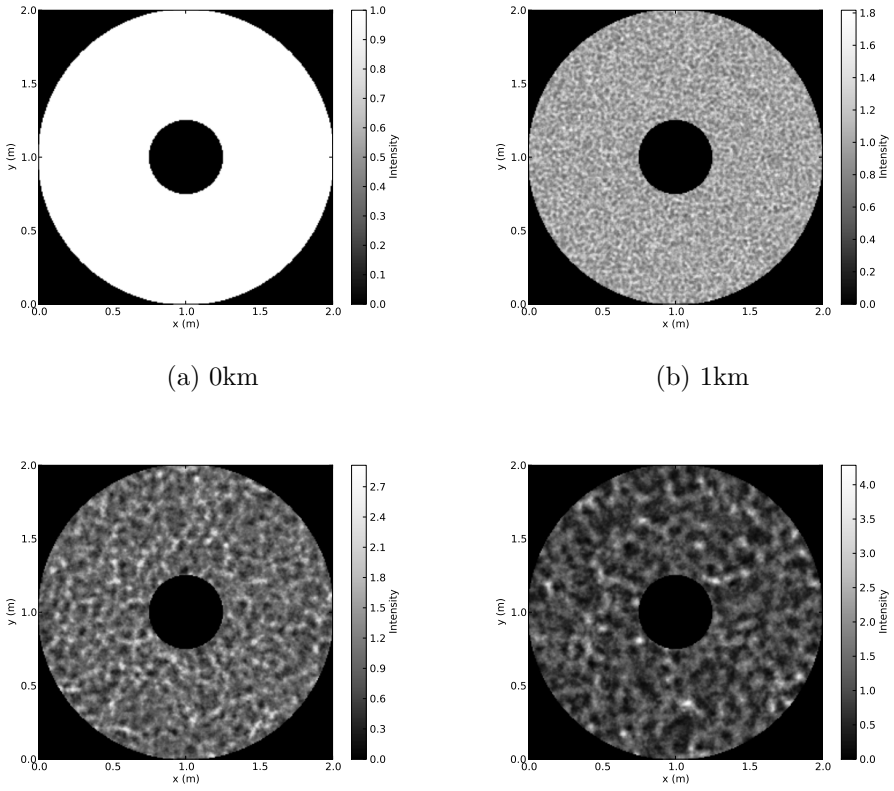

(a) 0km (b) 1km

(c) 5km (d) 15km

Figure 2.17: Simulated images showing the change in spatial scale of the flying shadow patterns with the height of the turbulent layer. Propagation distances between 0m (a) and 15km (d) are plotted. The longer the propagation distance, the larger the intensity variations and their spatial scale.

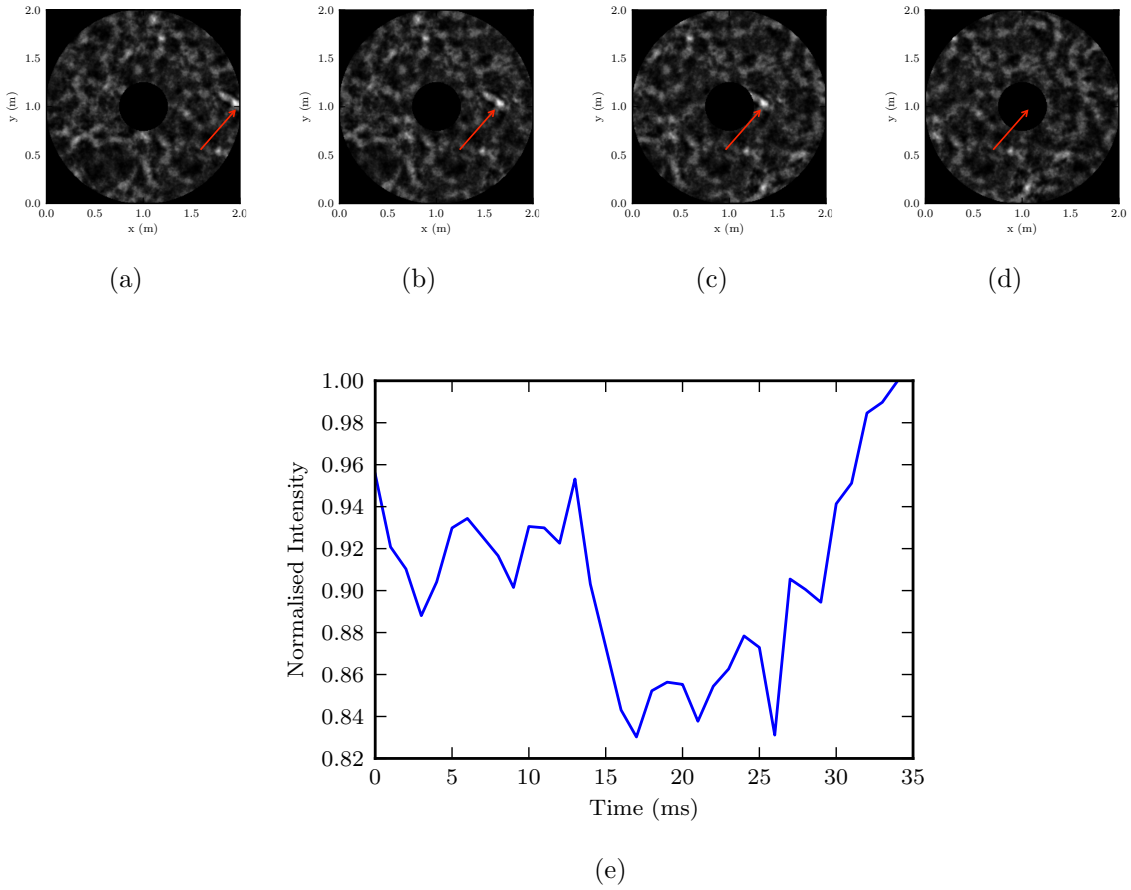

Figure 2.18: Simulated images showing how flying shadows cause image intensity variations. As the wind moves the flying shadow pattern along in the pupil plane (a) - (d), patches of higher and lower intensities move into and out of the pupil resulting in the corresponding total intensity variations in the image (e). The red arrows in the top figures (a) - (d) highlight a single bright patch as it crosses the telescope pupil. The intensity is measured to drop and rise again as the bright patch is obscured and reemerges from behind the secondary mirror.

$$\sigma_I^2 = 19.2\lambda^{-7/6}(cos(Z))^{-11/6}\int_0^\infty h^{5/6}C_n^2(h)\mathrm{d}h, \tag{2.50}$$

where λ is the wavelength and h is the atmospheric altitude.

For larger telescopes, with diameter greater than the characteristic scale of the turbulence, $D \gg r_F$, the high spatial frequency components of the intensity fluctuations are smoothed out, as described by Tatarski [131], Fried [49] and Young [143]. In this regime, scintillation is independent of the wavelength and the instantaneous σ_I can be determined from geometric optics as

$$\sigma_I^2 = 17.3\cos(Z)^{-3}\int_0^\infty h^2C_n^2(h)\mathrm{d}hD^{-7/3}. \tag{2.51}$$

The height squared term in equation 2.51 signifies that the high-altitude layers have a dominant contribution to scintillation.

For exposure times, $t_{\mathrm{exp}} \gg t_{\mathrm{cross}}$, the scintillation index is modified to [69],

$$\sigma_I^2 = 10.7\cos(Z)^{-3}\int_0^\infty \frac{C_n^2(h)h^2}{V_\perp(h)}\mathrm{d}hD^{-4/3}t_{\mathrm{exp}}^{-1}. \tag{2.52}$$

In this expression, the scintillation index is calculated from the integrated sum of the turbulence strength, $C_n^2(h)$, the horizontal windspeed, $V_\perp(h)$ and the height of each layer, as well as the telescope diameter and exposure time. For this reason, we require measurements of the wind speed, $V_\perp(h)$, to be able to model scintillation effects in long exposures.

There is no correlation between scintillation and angular seeing, as scintillation is strongly dependent on the height of the turbulence. In contrast, seeing has no height dependence. Typically, it is the lower layers of the atmosphere which contribute most to seeing, opposed to the high layers responsible for scintillation.

2.4 Other Sources of Noise on Photometry

Other than noise due to scintillation, sources of noise on photometry include shot noise due to photon bunching, shot noise due to the sky emission and noise due to the detector, which includes read noise, dark current and effects due to flat-fielding. The details of these can be found in e.g. Howell [64], and will be discussed in this

section. An additional seeing-related noise is introduced during the photometry procedure, known as, "aperture noise", which is described in chapter 5. In addition, the atmosphere may cause transparency variations that cannot be fully corrected by a comparison star due to spatial/temporal variations, e.g. cloud moving across the field of view. This will receive mention in chapter 6, and is not further examined here.

2.4.1 Photon Noise

Photon noise, also termed Poisson noise, or shot noise, is a basic form of uncertainty arising from the quantised nature of light. It is an inherent property of the signal and, as such, its magnitude is dependent on the signal. Photon noise is the dominant source of noise on targets that are not bright enough to be scintillation dominated, but not so faint as to be dominated by background and readout noise [90].

Photon detections behave as independent events that follow a random temporal distribution. Photon counting is a Poissonian process, where the probability that the number of counts, N, measured by a given detector element over an exposure time, $t_{\rm exp}$, equals a given value, k_c, is described by the probability distribution

$$P(N = k_c) = \frac{e^{-\lambda_p t_{\rm exp}} (\lambda_p t_{\rm exp})^{k_c}}{k_c!}, \tag{2.53}$$

where λ_p is the expected number of photons per unit time interval. It has the property that its variance equals the expected mean, $\sigma^2 = \mu$.

Photon noise increases with integration time as $\sigma \propto \sqrt{t_{\rm exp}}$. However, as $N \propto t_{\rm exp}$, the relative photon noise, $\sigma/N \propto 1/\sqrt{t_{\rm exp}}$.

2.4.2 Sky Background

Every pixel of a detector containing light from a target also contains light from the night sky. This light arises primarily from: light from the Moon, the Earth's atmosphere and zodiacal light.

- **Moonlight** has the most pronounced effect on the brightness of the optical sky background. Solar light is reflected by the moon and scattered by the Earth's atmosphere, mainly via Rayleigh scattering, with some contribution due to aerosols. Moonlight dominates in the near-UV and blue and decreases towards longer wavelengths, becoming negligible in the near-IR. Scattered light is strongly dependent on the phase of the moon, and because of this, the sky background can be classified based on the phase of the moon as: dark time (new moon $\pm 3-4$ days), grey time (half moon $\pm 3-4$ days) and bright time (full moon $\pm 3-4$ days).

- **Light from the Earths atmosphere** is caused by:
  - Light pollution, due to artificial lighting scattered by the atmosphere.
  - Airglow and auroral emission, highly variable and due to electronically and/or vibration-rotationally excited atoms and molecules (e.g. O_2, O, Na and OH) in the upper atmosphere.
  - Thermal continuum emission in the IR from the atmosphere, telescope and instruments. Thermal radiation becomes significant at the JHK bands and rapidly increases towards longer wavelengths ($> 2\mu$m).

- **Zodiacal light and gegenschein** are caused by reflection of solar light by interplanetary dust particles around 350-750nm in the ecliptic and in the "anti-Sun" direction due to back-scattering.

Noise due to sky brightness is a stochastic process, similarly to photon noise. Sky brightness is estimated simultaneously with the brightness of the target. It is usually measured in mags/arcsec^2. Table 2.1 gives an overview of the typical variation of sky brightness as a function of moon phase for different wavelengths, measured for La Palma [105]. In practice, sky brightness varies from site-to-site as well as with distance from the Moon, and the values presented are averages over Moon distance.

For targets brighter than $\sim$15 mag, sky background will not be an important source of noise [90]. Note that noise due to sky and dark current stays the same

Sky Brightness (mag/arcsec^2)					
Days from new moon	U	B	V	R	I
0	22.5	22.8	21.8	20.9	19.3
3	22.3	22.5	21.6	20.8	19.2
7	21.4	21.4	20.7	20.2	18.7
10	20.4	20.4	19.6	19.2	17.8
14	19.3	19.2	18.5	18.2	16.9

Table 2.1: Table of variation of sky brightness as a function of phase of Moon and wavelength in the optical for La Palma. Data from [105].

even after the mean sky and dark frame have been subtracted, since the shot noise from these sources will still be present.

2.4.3 Dark current

Even in the absence of signal, thermal effects spontaneously give rise to electron/hole pairs within the CCD pixels, which build up in the detector in a similar manner to the photo-electrons from the target, causing *dark current*. Cooling of the CCD drastically reduces the dark current, and the remainder can be subtracted from the frames during image processing. The noise due to dark current follows a Poisson distribution, and hence is proportional to the square root of the dark current.
As for photon noise, the same $\sigma/N \propto 1/\sqrt{t_{\rm exp}}$ applies for sky background and dark current.

For modern astronomical instruments that are cooled, dark current is very low. The dark current for both ULTRACAM [40] and the Durham-Sheffield *pt5m* telescope[1] CCDs when cooled to their respective operating temperatures of 233K and 248K is $< 0.05 e^-\text{pixel}^{-1} s^{-1}$.

[1] https://sites.google.com/site/point5metre/

2.4.4 Readout Noise

Readout noise, or just read noise, is noise originating from reading out the CCD and is independent of the signal level. Poissonian statistics do not apply to read noise as there is no signal associated with this noise source. The main source of read noise is caused by the measurement of charge in a capacitor via the correlated double sampling method (CDS). The faster the CDS is performed, the higher the uncertainty on the measurement. Smaller contributions to the readout noise arise from the electronics that amplify and convert an analogue signal to digital units, which is not perfectly repeatable. For the same amount of charge on a given pixel, the on-chip amplifier and analogue-to-digital converter will produce a statistical distribution of possible results centred on a mean value, whose distribution can be modelled with a Gaussian distribution. The electronics themselves inject unwanted electrons which end up digitised along with the pixel charge, causing random positive errors in the output. The resulting 1σ error from the combined effect of these is usually expressed in electrons root mean square (RMS). The read noise is independent of exposure time, but varies depending on the readout speed. For ULTRACAM, the readout noise is $3.5e^-$ in the slow and $5e^-$ in the fast readout modes, and $7e^-$ for *pt5m*.

2.4.5 Flat Fielding Noise

The quantum efficiency varies slightly from pixel to pixel due to differing areas, causing the pixels on the CCD each to have a slightly different sensitivity. This pixel non-uniformity is typically within $1\% - 2\%$ of the average signal. It can be corrected for by dividing the images by a calibration image of a uniformly-lit field, in a process called *flat fielding*, which also eliminates the effects of vignetting, dust on the telescope and other optical variations in the system. In reality, light from the star moves around on the detector due to tracking/guiding errors, and focus and seeing variations. Hence, imperfect flat fielding and image drift produces "flat fielding" noise in the light curve.

2.4.6 Noise Statistics

The signal-to-noise ratio (S/N) determines the fundamental precision limit σ for any photometric measurement. The equation for S/N is simply the ratio of the number of photo-electrons from the signal to the sum of the noise sources which combine in quadrature, [95]:

$$S/N = \frac{N_* t_{\rm exp}}{\sqrt{N_* t_{\rm exp} + n_{\rm pix}(N_{\rm sky} + N_{\rm dark} + N_{\rm read}^2)}}. \tag{2.54}$$

In the above equation, often called the *CCD equation*, N_* is the number of photo-electrons from the target per second, $N_{\rm sky}$ the photo-electrons from the sky background per second per pixel, $N_{\rm dark}$ the dark current per second per pixel, $N_{\rm read}$ the read out noise in electrons per pixel and $t_{\rm exp}$ is the exposure time. The sky, dark and read noise terms are multiplied by $n_{\rm pix}$, the number of pixels that the image of the star is spread over. This means that a smaller PSF will result in a higher S/N for a given exposure time.

2.4.7 Systematic Noise

As opposed to uncorrelated "white" noise resulting from Gaussian stochastic processes, systematic "red" noise on a light curve is noise that is correlated. The effect of systematic noise on planetary transits has been well studied previously [109]. Systematic noise is always present at a certain level in photometry. It can be intrinsic to the data, due to uncorrected instrumental effects and observing conditions, or it can arise from data reduction. Systematic trends in the data are likely caused by a combination of: changing airmass, atmospheric conditions, telescope tracking and rotation and flat-field errors. Red noise is particularly significant in transit surveys searching for planets, where it can limit the detection capability. If only white noise is assumed in the presence of red noise, the real S/N ratio of the transit will be overestimated, which can lead to false detection.

During observation, ensuring that the target PSF is always on the same pixels on the CCD reduces systematic noise which may arise due to inhomogineities between CCD pixels. During data analysis, the differential flux can be correlated with parameters including the pixel shift of the centre of the PSF, sky background and

rotator paratactic angle to determine the presence of correlated noise and correct fit to it. Methods of estimating red noise include RMS binning [109] and Gaussian processes [19]. Since there are currently several methods for the correction of red noise [130; 92], we will not examine it in detail in the scope of this thesis.

Chapter 3

Numerical Simulations of Atmospheric Scintillation

This chapter describes the atmospheric and instrument simulation code used for the work in the later parts of this thesis (chapters 4 and 5). The theory and methods for producing simulated wavefront perturbations and Fresnel propagation are discussed. The underlying assumptions and limitations of the simulation are described. The resolution and sampling of the data are discussed. The simulation is verified against theoretical predictions for turbulence strength, size of seeing disc and scintillation index.

3.1 Modelling Atmospheric Scintillation

The simulations used for calculating the amplitude and phase variations of a perturbed complex 2-D wavefront are from the Durham AO simulation framework [4]. This code was developed to calculate wave fronts in turbulent media for developing algorithms and systems for real time adaptive optics. Its theoretical basis are the methods outlined by Ellerbroek [45]. The atmosphere is modelled by a discrete number of layers placed at different altitudes. The phase modulations of a plane wavefront after passing through a turbulent layer are represented by a phase screen with a Kolmogorov power spectrum. A Fresnel diffraction kernel is used for handling propagation to the ground and calculating the final resulting complex

wavefront. The complex field is translated depending on the wind velocity profile at every step and a section of it is sampled to produce the intensity at the pupil plane. The turbulent layers are considered frozen as they move across the telescope pupil, in accordance with Taylor's approximation, described in section 3.3. The square of the Fourier transform of the pupil complex amplitude transmitted by the aperture function results in the image intensity. For the work performed in chapters 4 and 5, I have modified and incorporated the basic phase screen generator into a custom software, which I have written. Modifications to the simulation are the inclusion of wind speed and sampling rate, which allows simulation of finite exposure images, and the zenith angle. I have also written options for simulating photon noise, measuring the PSF, performing aperture slicing, obtaining image intensities from the complex phase and performing geometrical propagation.

3.1.1 Phase Screen Generation

The effect of turbulence on a complex field is described in detail by Roddier [116] and Dravins et al. [42, 43, 44]. The key steps are presented here for completeness. Consider a complex 2-D wavefront, U_0, with amplitude, A, and phase, ϕ,

$$U_0(x, y) = A(x, y)\exp(i\phi(x, y)), \tag{3.1}$$

incident on a single turbulent layer in the atmosphere between the heights of h and $h + dh$. For simplicity, the light is assumed to be of a single wavelength, λ, and the layer thickness is small enough for diffraction effects to be negligible over a distance dh, but larger than the correlation scale of the atmospheric inhomogeneities.

Due to refractive index variations, $n(\mathbf{x}, \mathbf{h})$, described in chapter 2, the wavefront experiences a phase shift, $\Delta\phi(\mathbf{x})$,

$$\Delta\phi(\mathbf{x}) = k \int_{h}^{h+dh} n(\mathbf{x}, \mathbf{z})\mathbf{dz}, \tag{3.2}$$

where k is the wavenumber.

For Kolmogorov turbulence, the spatial power spectrum of the phase variations is

$$\boldsymbol{\phi}(\boldsymbol{\kappa}) = \boldsymbol{\kappa}^{-11/3}. \tag{3.3}$$

In the simulations, the phase modulated screens are generated by filtering Gaussian white noise by a spatial power spectrum, $\Phi(\kappa)$, to obtain a random field with the correct second order statistics. The Gaussian noise is simply a complex field with a zero mean and unit variance, of the form $(r(\boldsymbol{\kappa}) + ir'(\boldsymbol{\kappa}))$, where $\boldsymbol{\kappa}$ is the spatial frequency variable.

Hence, the atmospheric phase screen, $P(x, y)$, is computed as

$$P(x,y) = c \cdot Re\left(\mathscr{F}\left[\sqrt{\boldsymbol{\Phi}(\boldsymbol{\kappa})}(r(\boldsymbol{\kappa}) + ir'(\boldsymbol{\kappa}))\right]\right), \tag{3.4}$$

where $\mathscr{F}$ denotes the 2-D Fourier transform and c is a scaling factor. The scaling factor allows the strength of each layer to be expressed in terms of the Fried parameter, r_0,

$$c = \frac{0.1517}{\sqrt{2}}\left(\frac{W}{r_0}\right)^{5/6}, \tag{3.5}$$

where W is the width of the phase screen. This definition of c results in a phase screen expressed in radians of phase at a given wavelength λ. The Fourier transform in equation 3.4 is implemented using a Fast Fourier Transform (FFT), and the result is a phase screen which is periodic. The implications of this are that the phase screen is required to be significantly larger than the telescope aperture diameter, as well as larger than the outer scale of the turbulence L_0. In the Kolmogorov regime, where $L_0 = \infty$, the simulations will always underestimate the amount of turbulence in the low order modes. Figure 3.1 shows the effect of Kolmogorov turbulence on a wavefront after propagating through the atmosphere, based on simulation. The phase variations exhibit fractal properties between the inertial ranges $l_0 < r < L_0$.

A real atmosphere will often consist of several thin layers between different heights h_i and $h_i + \Delta h_i$. For each layer, as long as the phase fluctuations are small, $\Delta\phi(\mathbf{x}) \ll \mathbf{1}$ (referred to as the *weak-perturbation regime*), the effects of all the turbulence layers are linearly additive. Typical turbulence profiles at a good observing site show that scintillation is dominated by the high altitude layers (e.g. [135], 75%). Because of this, for simplicity we only consider the effect of wavefront propagation through a single turbulent layer.

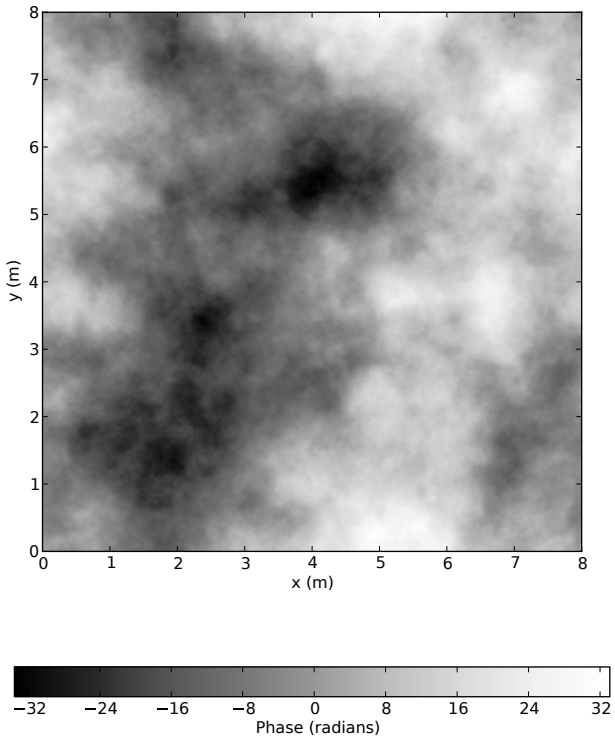

Figure 3.1: Phase variations arising from Kolmogorov turbulence. An initially flat wavefront is multiplied by a phase aberration map such as this one in order to give rise to an corrugated wavefront. The magnitude of the phase change depends on the intensity of the turbulence.

3.1.2 Optical Propagation

After experiencing phase distortions by the turbulent layer, the wavefront propagates to the ground through free space. Since the wavelengths considered are much smaller than the size of the wavefront perturbations, the Fresnel (near-field) diffraction regime can be applied.

Fresnel Propagation

The phase change resulting from passing through optical turbulence is carried out as a multiplication of the field, $U(x, y)$ and the complex exponential of the atmospheric phase screen in equation (3.4).

Fresnel propagation is a spatial filtering operation, implemented through a convolution between the incident complex field and a Fresnel propagation kernel, $K(x, y, z)$:

$$K(x, y, z) = \frac{i}{\lambda z}\exp(ikz)\exp\left(\frac{ik}{2z}\left[(x - x') + (y - y')\right]^2\right). \tag{3.6}$$

The Fresnel integral [54] for an optical field at a point (x, y), after passing through the nth atmospheric layer is:

$$U_n(x', y') = \iint_{-\infty}^{\infty} U_0(x, y)\frac{i}{\lambda z}\exp(ikz)\exp\left(\frac{ik}{2z}\left[(x - x') + (y - y')\right]^2\right)dx'dy', \tag{3.7}$$

where z is the propagation distance, $k \equiv \frac{2\pi}{\lambda}$, and λ is the wavelength. The vectors (x, y) and (x', y') indicate the coordinates of the initial and final propagation positions.

An alternative way of expressing the Fresnel integral is through a convolution

$$U_n(x', y') = U_0(x, y) \otimes K(x, y, z), \tag{3.8}$$

where the symbol $\otimes$ indicates convolution. In the simulation, the convolution is carried out as the Fourier transform

$$U(x', y') = \mathscr{F}^{-}\left[\mathscr{F}(U_n(x, y) \times \mathscr{F}(K(z))\right], \tag{3.9}$$

where $\mathscr{F}^{-1}$ indicates the inverse Fourier transform. The pupil intensity is obtained from the real component of the complex field, $\mathrm{Re}(U)$.

Since Fresnel propagation is carried out as a multiplication in Fourier space, the finite extent of the phase screen can give rise to edge effects, which appear as a series of diffraction rings around the edge of the screen. To ensure that these edge effects are not present in the final pupil intensities, the phase screens are always produced four times larger than the extent of the pupil images required.

Geometrical Propagation

Simulating full Fresnel propagation is slow and computationally intensive. Where only phase aberrations are of interest, we make use of a much faster geometrical propagation code. This method is valid under weak scintillation conditions (see section 3.3). Geometrical propagation allows the examination of the seeing disc, while the intensity of all resulting images stays constant. The complex phase screen at the ground, U_g, is obtained by simply summing the phase shift $\Delta\phi_n$ from every layer n for a total number of m layers:

$$U_g(x', y') = U_0 \sum_{n=0}^{m} \exp(i\Delta\phi_i(x, y)). \tag{3.10}$$

The Image Plane

The required telescope aperture is 'sliced' from the complex field at the ground. This is done by multiplying the matrix of the complex field by a pupil mask.The pupil intensity is the square of the absolute value of the complex field. The intensity at the image plane is obtained from the square of the absolute value of the Fourier transform of the complex. To avoid aliasing, the pupil intensity is oversampled by a factor of 2.

3.2 Simulating the Photon Noise

In this section, the method for scaling the image intensity according to the total number of photons in the telescope aperture is described. The total number of photons are required when adding photon noise onto the image. It is calculated as:

$$\text{photons} = \text{bandwidth} \times \text{throughput} \times \text{rate factor} \times t_{\text{exp}} \times \pi(D/2)^2/10^{-m/2.5}), \quad (3.11)$$

where t_{exp} is the exposure time, D is the telescope diameter and m is the apparent magnitude of the simulated target. Below, we describe the terms for the instrument throughput, bandwidth and rate factor from the star.

Throughput

Throughput is defined as the ratio between the photo-electron flux detected by the instrument and the incoming flux of photons above the atmosphere in cm^{-2}. The throughput is calculated as the combination of the transmission of the atmosphere, telescope mirror(s), instrument, filter and the quantum efficiency of the detector. The typical range of throughput for a good CCD system in the optical is between 30% - 50% [39; 124; 112]. Throughout our simulations we employ a constant value of 0.4 for the total throughput.

Bandwidth

Every photometric system has a well-defined range of wavelengths, which is determined by the filters used. In the optical, the UBVRI passbands devised by Bessell [8] are the most commonly used, which have bandwidths as described in table 4.2. In the infrared, the transparency of the Earth's atmosphere is limited except in windows, which typically determine the bandwidth. Unless otherwise stated, we used a value of 900Å in the camera simulations, corresponding to the bandwidth of the V filter.

Rate Factor

The rate factor is the measure of the number of photons from the star at the top of the atmosphere per pixel per unit area of telescope per unit wavelength interval. Values for the rate factor depend on the wavelength and are presented in table 4.2.

3.3 Model Assumptions and Limitations

The key assumptions and model limitations are presented in this section. Their impact on the validity of the simulation are examined.

Kolmogorov Power Spectrum of Turbulence

One of the main assumptions of the simulation is that the power spectrum of the phase variations follows a Kolmogorov distribution everywhere at all times. There is observational evidence from space-based scintillation measurements and balloon-borne temperature readings which suggest that the atmosphere does not always behave this way [34; 53; 146]. These results show that the turbulence in parts of the atmosphere follows an arbitrary non-Kolmogorov power law which is more suitably described by a generalised von Karman spectrum with a gradient that is less than 11/3. However, such a behaviour typically occurs for low wind speeds, when the spatial scale of the turbulence is not properly sampled. A generalised power spectrum [11] can be used to describe the atmospheric turbulence in this case. Within the scope of this work we only consider Kolmogorov turbulence, which is the most prevalent and typically used for adaptive optics simulations e.g. [68].The Kolmogorov power law also does not hold for strong turbulence, therefore the scintillation model is not expected to produce valid results for small Fried parameters. However, this is not expected to be a problem when modelling good observing sites.

Finite Outer Scale

The equations of Kolmogorov are not valid on scales larger than the outer scale, L_0, and smaller than the inner scale, l_0. Fluctuations caused near the inner scale have very little energy and can safely be ignored. For fluctuations on a longer scale than L_0, the telescope aperture acts as a spatial filter, as long as $D < L_0$. However, measurements of L_0 [145] have shown that L_0 can vary in scale between 1m and 100m. For the higher values of D/L_0, the Kolmogorov model overestimates the scintillation.

More generalised models exist for taking into account the effect of the outer

scale, such as the von Karman model [113], sometimes used for adaptive optics simulations for extremely large telescopes. For the scope of this work, where we are interested in scintillation, which is particularly significant in the small telescope regime ($D < 8$m), we find it reasonable to assume that the effect of the finite size of the outer scale will be negligible in the vast majority of cases.

Thin Screen Approximation

For the purpose of the simulations, we assume that the thickness of layers is small compared to the propagation distance. Observations using SCIDAR [140] have shown that optical turbulence is in the form thin turbulent layers. Since the main cause of optical turbulence is wind shear which happens in a thin region between layers of different velocities, a thin screen approximation is reasonable to make.

Weak Turbulence

Strong turbulence at high altitude will cause scintillation to saturate i.e. the scintillation index does not increase with increasing turbulence [55]. However, for a good observing site under favourable conditions the turbulence strength will be weak ($\Delta\phi(\mathbf{x}) \ll \mathbf{1}$).

Frozen Flow

The frozen flow hypothesis [132] is frequently applied in the investigation of fluid flow physics. It states that the turbulence is stationary, or "frozen", over the timescales of the crossing time of the turbulent layer. Several experimental measurements of atmospheric turbulence [61; 38] have shown that atmospheric structures higher than the ground layer are long lived and are suitable for Taylor's approximation. While some velocity dispersion is expected, and according to [42] the shadow pattern will not remain coherent during the order of the one second it takes for the pattern to fly across the aperture, this temporal evolution of the shadow pattern will not affect the order-of-magnitude estimate of the scintillation index. Velocity estimations using SCIDAR (verified by e.g. [3]) rely on temporal correlations between turbulence patterns (see chapter 5), which would not work if the frozen flow hypothesis did not

hold true. Turbulence from the ground-layer does not propagate far enough to cause intensity variations, and can be disregarded for the purpose of scintillation studies.

3.3.1 Exposure Time

The length of the exposure that can be simulated from a phase screen is limited by its finite extent. Longer exposure images can be produced by averaging several shorter exposure phase screens. This can be done as the scintillation arises mainly from the smaller scale variations in intensity, so combining intensity variations from multiple screens does not affect the overall statistics of the intensity variance considered, in most cases.

3.4 Simulation Prerequisites and Model Verification

The output of the simulation is tested against the analytical equations of to verify its suitability for simulating scintillation and to establish the regimes where the scaling laws break down.

3.4.1 Sampling

Atmospheric turbulence is continuous in both the temporal and spatial extent. When modelling the turbulence in discrete elements, it is important that the intensity variations are correctly sampled. This is discussed below.

Temporal Sampling

The number of phase screens required for a given exposure duration depend on the temporal sampling. The temporal sampling rate is chosen so that the statistics of the scintillation are properly sampled. Since we do not require the power spectrum of the intensity variations, Nyquist sampling is not required.

In the simulations, temporal sampling is performed by adjusting the step size of the movement of the flying shadow pattern. For a simulation of a telescope of

diameter D and resolution n_{pup} the step size is calculated as

$$\text{step size} = dt \times \frac{V_{\perp} \times n_{\text{pup}}}{D}, \tag{3.12}$$

where dt is the sampling rate in Hz and $V_{\perp}$ is the wind velocity perpendicular to the line of sight of the telescope.

Spatial Sampling

For a signal to be spatially well sampled, the resolution of the images must satisfy the Nyquist sampling condition, which states that the smallest spatial scale present must be resolved by at least two elements. For the pupil intiensities, the smallest scale, δr_{min}, is determined by the Fresnel radius, r_F, given by:

$$\delta r_{\text{min}} \leq \frac{\sqrt{\lambda h}}{2}. \tag{3.13}$$

A frequent assumption is that scintillation develops at propagation distances of 2km or more, so for visible wavelength, $\delta r_{\text{min}} \leq 1.6$cm. In the majority of the simulations, we take $h = 10$km, so that $\delta r_{\text{min}} \leq 3.5$cm. In the pupil plane, the spatial sampling is obtained from:

$$\text{spatial sampling in pupil} = \frac{D}{n_{\text{pup}}}. \tag{3.14}$$

In the image plane,

$$\text{simulated image scale} = \frac{\lambda}{2D} \times 206265\text{"/pixel}. \tag{3.15}$$

When simulating a 2m telescope with a resolution of 256 pixels, the pixel size is 0.78cm, which is lower than the required δr_{min}. For a seeing of $r_0 = 10$cm, this results in 12 pixels/r_0 patch. The effect of under-sampling the spatial resolution is shown in figure 3.2.

For small values of r, the phase structure function matches that of the Kolmogorov model well. Due to the outer scale imposed by the finite size of the screen, the phase structure function approaches that of a von Karman model towards large values of r.

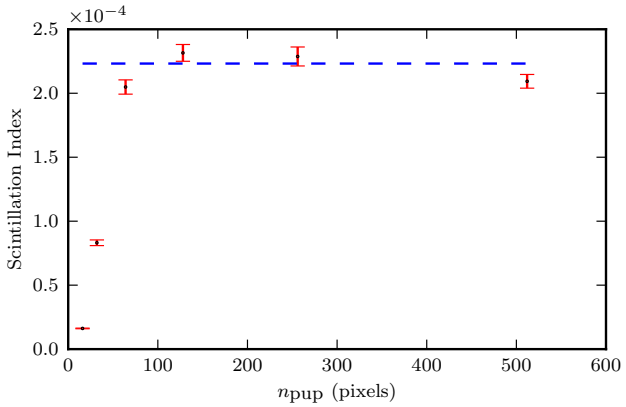

Figure 3.2: Scintillation index estimate as a function of telescope resolution for a 2m telescope, for different screen resolutions, with turbulence at 10km. The figure shows that if the flying shadow pattern in the telescope pupil is not sampled correctly, the value of the scintillation index is underestimated, as shown by the first 3 points. The blue dashed line shows the best-fit value for scintillation index, excluding the first 3 points. The sampling required is at least 126 pixels, corresponding to a resolution of 1.6cm.

3.4.2 Image FWHM

The FWHM of the simulated long-exposure images were tested to ensure correct behaviour of the simulation. For different values of r_0, 20 10s images were generated. Figure 3.3 shows the measured FWHM against the ratio of r_0/λ. In the Kolmogorov model, the angular diameter of the PSF is expected to be $\varepsilon_{FWHM} = 0.976\frac{\lambda}{r_0}$. However, as with the structure function, the outer scale, L_0 in the simulation will affect the outcome of the FWHM. The size of the FWHM in the von Karman regime, ε'_{FWHM} depends on L_0 as given by [89]

$$\varepsilon'_{FWHM} = \varepsilon_{FWHM}\sqrt{1 - 2.183(r_0/L_0)^{0.356}}. \tag{3.16}$$

For the simulation values of r_0=10cm and an outer scale of 8m, one would expect a gradient of $\varepsilon'_{FWHM} = 0.72$", which is in agreement with the best fit gradient to the simulation data of 0.74±0.04".

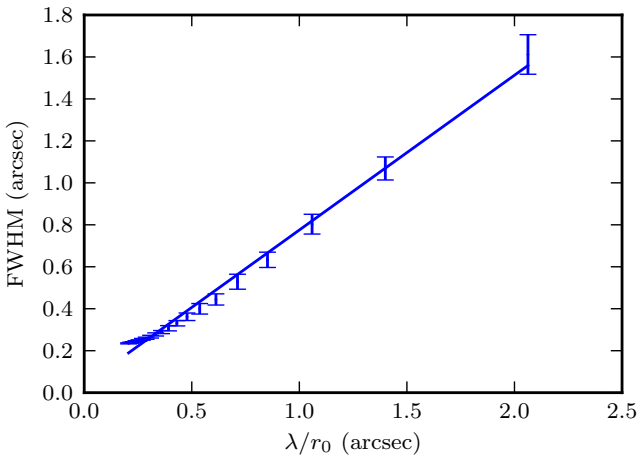

Figure 3.3: FWHM of point spread function of simulated image compared to the ratio of λ/r_0. The data are best fit with a straight line of gradient 0.74±0.04.

3.4.3 Power-law dependences of Scintillation

The dependence of scintillation on turbulence intensity, turbulence height and telescope diameter was tested for the short exposure regime ($t_{\text{exp}} < D/V_{\perp}$). In this regime, the scintillation index follows the power laws described by equation 2.45. Expressing this in terms of r_0 using the definition from equation 2.51:

$$\sigma_I^2 \propto D^{-7/3} h^2 r_0^{-5/3}. \tag{3.17}$$

The following results were obtained from 50 sequences of 300 images each, for a telescope of D=2m and a telescope resolution of 1cm/pixel.

Propagation Height Dependence

The dependence of scintillation index on the height of the turbulent layer was investigated between a height range of 0.5km and 2.5km (Figure 3.4).

The data are best fit with a straight line of gradient 1.8 ±0.1, showing simulation agrees with the theoretical value of 2 within the statistical uncertainties of the simulation.

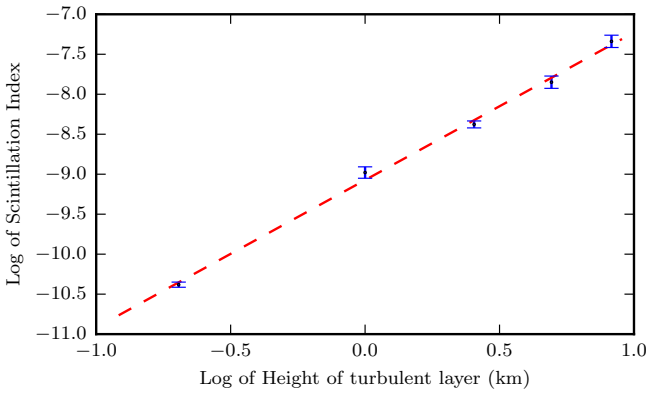

Figure 3.4: Best-fit height dependence of scintillation index (dashed line) for the short exposure regime from simulation points. The gradient is 1.8±0.1, which matches theoretical power law of 2 within 2 s.d.

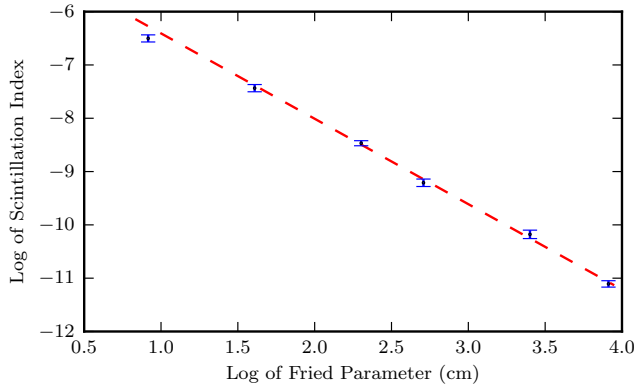

Figure 3.5: Dependence of scintillation index on r_0 for the short exposure regime from simulation. Gradient 1.59 ± 0.06 matches theoretical power law within 2 s.d.

Turbulence Strength Dependence

The change of scintillation index with Fried parameter, r_0 to the -5/3 power (equation 3.17) was investigated for a range of values of the Fried parameter between 2.5cm and 50cm for a constant height of 10km. Figure 3.5 shows the results obtained.

Note how for small values of r_0, the simulation underestimates scintillation due to the break down of the weak scintillation approximation (see section 3.3). For values of r_0 of 5cm or more, as expected for a good observing site, the best fit line of gradient, 1.59 ± 0.06 agrees with theory within the statistical uncertainties of the simulation.

Telescope Diameter Dependence

The dependence of scintillation index on telescope diameter was tested by considering a range of diameters between 0.5m and 8m for turbulence regimes between poor and excellent seeing. The results are summarised in figure 3.6.

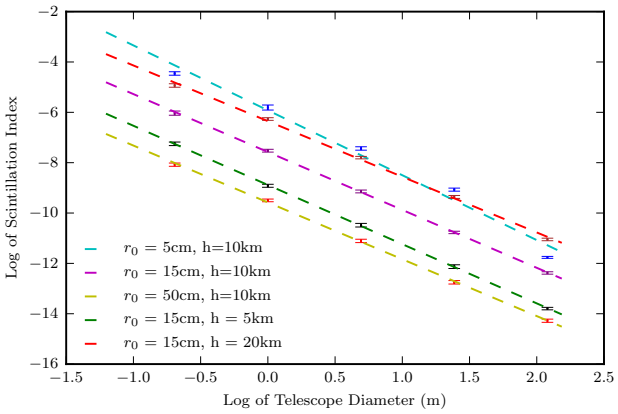

Figure 3.6: Dependence of scintillation index on D for the short exposure regime, for a range of height and r_0 values. All gradients agree with the 7/3 power law within the statistical uncertainties of the simulation.

All results agree with the expected 7/3 power law the statistical uncertainties of the simulation.

3.5 Conclusion

In this section we presented the underlying theory of the simulations used in later parts of the thesis. The methods used for generating and propagating complex phase screens were presented. The underlying assumptions and limitations of the simulation were discussed. Tests to confirm the validity of the simulations were performed. These included measuring the resulting FWHM and investigating the behaviour of the measured scintillation index from the simulations. The conditions for accurate sampling in the temporal and spatial domains were discussed and tested. These showed the simulation to be suitable for modelling the effects of scintillation based on the theory presented.

Chapter 4

The Contribution of Scintillation to Noise in High Time Resolution Ground-Based Photometry

4.1 Introduction

The decrease in flux during an exoplanet transit is small compared to the flux of the host star ($\sim 1\%$ for the transit of a hot Jupiter and $\sim 0.2 - 0.1\%$ for the secondary eclipse). For this reason, bright stars, which provide a high signal, are ideal candidates. Indeed, several of the next-generation of transit searches, such as TESS and NGTS will focus on finding planets around bright stars of magnitude 13 or greater, due to the ease of follow-up for such objects from the ground. However, scintillation sets a fundamental limitation on the precision that can be obtained for exoplanet transit photometry from the ground. While adaptive optics has been successfully used to provide diffraction-limited imaging, the first generation of instruments for correcting for the intensity fluctuations caused by scintillation are only currently in development [102]. For these instruments, understanding the regimes where scintillation is the dominant source of noise is essential.

Previous work on the detection limits of fast photometry has been performed by Mary [90] and Southworth et al. [128], who try to break down noise on a light curve into constituent parts and investigate the relative contributions of scintillation and

photon noise through statistical analysis of scintillation. However, these have been for an atmosphere with a turbulence profile averaged over time. Measurements of atmospheric turbulence using, for example, SCIDAR (SCIntillation Detection And Ranging) have shown that a more accurate representation of atmospheric turbulence is one which consists of a number of discrete layers displaying Kolmogorov statistics [136]. The actual noise due to scintillation can vary considerably from night to night depending on the magnitude of the high-altitude turbulence.

This chapter consists of two main parts. In the first part, the effect of atmospheric turbulence on the noise on the light curve is investigated. To begin, the values of scintillation estimated for an average atmosphere are compared to the estimates of scintillation obtained from values of the refractive index structure constant, $C_n^2(h)$, for discrete layers, measured using SCIDAR on La Palma. To follow, the analytical power-law dependence of scintillation on the telescope diameter and exposure time of is tested through simulation. These relations will be later compared to real data in Chapter 6. Using the discrete layer approach, the contribution of scintillation to the noise on photometry is examined for different target magnitudes and turbulence strengths. The magnitudes where scintillation becomes a limiting source of noise are discussed. The effect of scintillation noise towards the near-infrared wavelengths is also examined.

In the second part of this chapter, we examine the effect of scintillation noise on the uncertainty of the measured astrophysical parameters of exoplanets. This is carried out using Markov-chain Monte Carlo fits to simulated light curves. The aim of this part of the chapter is to show how reducing noise on light curves improves the measurement errors on the transit parameters.

4.2 Averaged Versus Instantaneous Scintillation

When estimating the contribution of scintillation to the overall noise budget in photometry, astronomers most frequently use the relation given by Dravins (1998) [44], originally formulated by Young (1967) [143] for the intensity variance, σ_I^2:

$$\sigma_I = 0.004 D^{-2/3} (\sec \mathrm{Z})^{7/4} e^{-h/h_0} / (2t)^{1/2}, \tag{4.1}$$

where D is the diameter of the telescope aperture in metres, Z is the zenith distance, h is the altitude of the observer above sea level in metres , $h_0 \simeq 8000$ m is the atmospheric scale height and t the exposure time in seconds. This approximation is derived through geometric-optics and assumes an atmosphere with a $C_n^2(h)$ profile which is averaged over time. All previous work on the detection limits of fast photometry have used equation 4.1 for an averaged atmosphere when estimating the noise due to scintillation. The actual noise due to scintillation, however, can differ considerably from this value depending on the magnitude of the high altitude turbulence . A more accurate way to quantify the amount of noise due to scintillation is by measuring the instantaneous atmospheric $C_n^2(h)$ profile. The equation for calculating scintillation index from a measurement of $C_n^2(h)$ is Kenyon et al. [69]

$$\sigma_I = 10.7 \left[\int_0^\infty \frac{C_n^2(h) h^2}{V_\perp(h)} \mathrm{d}h \right]^{1/2} D^{-2/3} t^{-1/2}. \tag{4.2}$$

This is valid for telescope diameters larger than the Fresnel radius $D >> r_f$ and for exposure times longer than the crossing time for the flying shadow pattern $t > D/V_\perp$. Previous measurements by Kornilov et al. [75] using MASS instruments have shown that the magnitude of the scintillation index varies by a factor of 2 between the 1st and 3rd quartiles of the overall seeing distribution for a number of observatories. For ease of comparison with our simulations, as well as to provide a simple means for quantifying optical turbulence, we introduce the term $C_n^2(10000)$. This is the turbulence strength, C_n^2, of a single layer at 10km that would give rise to the measured scintillation index if all of the scintillation originated from this layer. Figure 4.1 shows a histogram of the distribution of the measured scintillation on La Palma, measured from 20 nights of turbulence profiling using the SCIDAR instrument [102]. Table 4.1 summarises the statistics of the seeing distribution.

Taking the ratio of the value of σ_I calculated from equation 4.1 and 4.2, it can be shown that on average, Dravins' equation underestimates scintillation by a factor of 2. Figure 4.2 illustrates this. For the calculation, the value of $h = 2332$, the altitude in metres of the Roque de Los Muchachos Observatory was used.

As $C_n^2(10000)$ varies considerably from night to night, it is important not to rely on a single averaged expression to estimate the noise from scintillation, but to

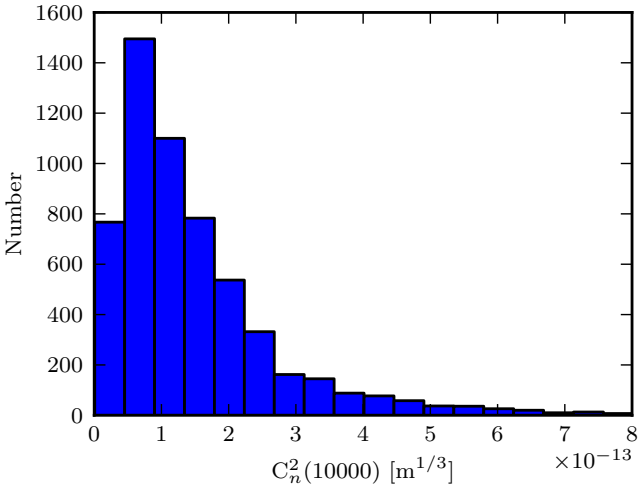

Figure 4.1: Histogram showing total scintillation index converted to an equivalent C_n^2 at 10km for La Palma from 20 nights of observation using Stereo-SCIDAR.

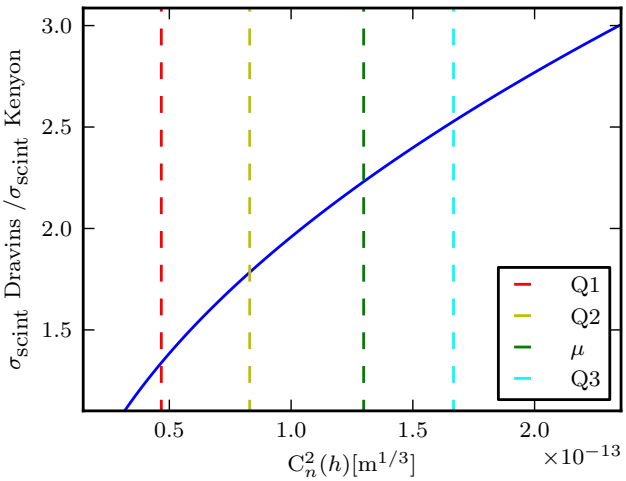

Figure 4.2: Applying an average atmosphere estimate to calculate the noise due to scintillation causes the scintillation noise to be underestimated by a factor of 2 on average for the turbulence profiles measured on La Palma. This is seen from the intersection of the mean line with the ratio of $\sigma_{\text{scint Dravins}}/\sigma_{\text{scint Kenyon}}$. The red, yellow, green and cyan dashed lines indicate the C_n^2 profiles for the first quartile, second quartile (median), mean and third quartile of the seeing distribution respectively.

Quartiles	$C_n^2(10000)$ ($\times 10^{-15}$ m$^{1/3}$)	r_0 at 550 nm (cm)	magnitude below which scintillation dominates
Q1	46.7	56.7	9.71 ± 0.02
Q2	83.0	40.1	10.36 ± 0.02
Q3	166.7	26.4	11.05 ± 0.02
μ	129.8	30.7	10.85 ± 0.02

Table 4.1: Distribution of $C_n^2(10000)$ for La Palma. $C_n^2(10000)$ is the turbulence of a single layer at a height of 10km that gives rise to the same measured scintillation index as the sum of the scintillation indices resulting from of every individual layer at each different altitude. The rightmost column shows the corresponding V-magnitude limits below which scintillation dominates, obtained from simulation (see section 4.6).

determine it case-by-case depending on the turbulence in the atmosphere.

4.3 Verification of Analytical Models of Scintillation

According to the relations of Young [143], Dravins et al. [44] and Kenyon et al. [69], scintillation follows the relation:

$$\sigma_I \propto D^{-2/3} t^{-1/2} \tag{4.3}$$

This equation states that the scintillation, quantified by the index, σ_I, is dependent on telescope diameter D to the power $-2/3$ and exposure time t to the power $-1/2$. In this section, we investigate whether the results from the simulation described and tested in Chapter 3 follows these relations. This is done in order to confirm the validity that our simulation results behave as predicted on longer timescales, and to show that the results from the simulation and the theoretical equations of Kenyon et al. [69] can be used interchangeably.

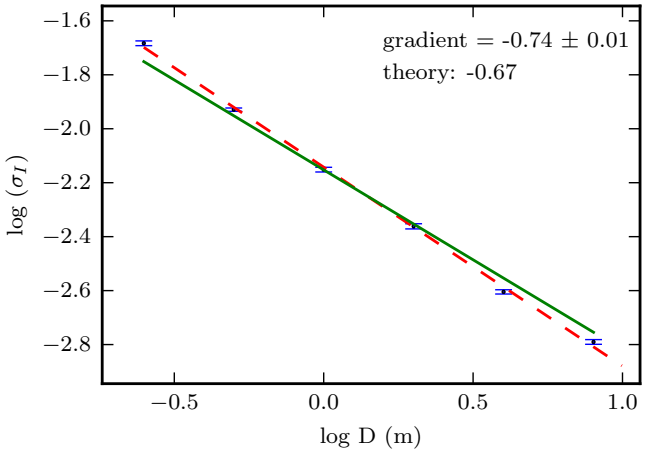

Figure 4.3: Dependence of scintillation index on telescope diameter, showing the simulation results (blue dots) and theory (equation 6.3 – green solid line) for images produced with a short exposure time of 1s. The red dashed line is the best fit to the simulation points.

4.3.1 Dependence on Telescope Diameter

In Chapter 3, the dependence of scintillation index on telescope diameter was investigated for instantaneous intensity images. As explained in Chapter 2, real observations consist of many instantaneous speckle images averaged over a finite exposure time. The telescope diameter-dependence of the scintillation index of these finite exposure images is investigated through simulation. The scintillation index arising from 100 simulated images is measured 10 times for telescope diameters ranging between 0.25m and 16m. This was carried out for images of short, 1s, and long, 50s, exposure times, for scintillation arising from a single layer with r_0 of 10cm at 10km. The size of the phase screen was set so that the pixel size is constant for each telescope diameter.

The results of the simulation are compared to the analytical expression of Kenyon et al. [69] in Figures 4.3 and 4.4.

The estimates of the scintillation index from the simulation agree with the theoretical equations within 3σ or better for telescope sizes smaller than 4m. However, the obtained gradient is close to, but not in perfect agreement within error. The deviations for large telescope diameters is due to the finite outer scale imposed by

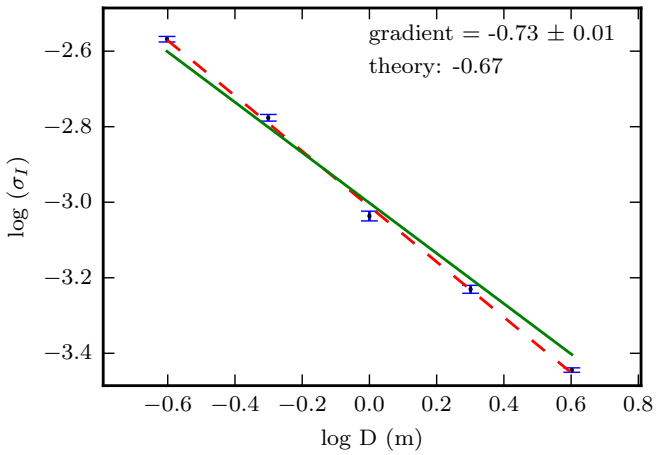

Figure 4.4: Dependence of scintillation index on telescope diameter, showing the simulation results (blue dots) and theory (equation 6.3 – green solid line) for images produced with a long exposure time of 50s. The red dashed line is the best fit to the simulation points.

the finite size of the complex field. This causes the simulations to overestimate the the variation of scintillation with telescope diameter for large values of D. However, within the range of telescope diameters investigated (0.5m – 4m), the amount of scintillation predicted by the simulation is in good agreement with theory.

4.3.2 Exposure Time Dependence

For a constant telescope diameter of 2m, the effect of simulating increased exposure time on the scintillation index was tested, shown in Figure 4.5. The results show the simulation and theory agree within 3 standard deviations, except at very short exposure times, where the value for scintillation tends to the short exposure regime (equation 2.51).

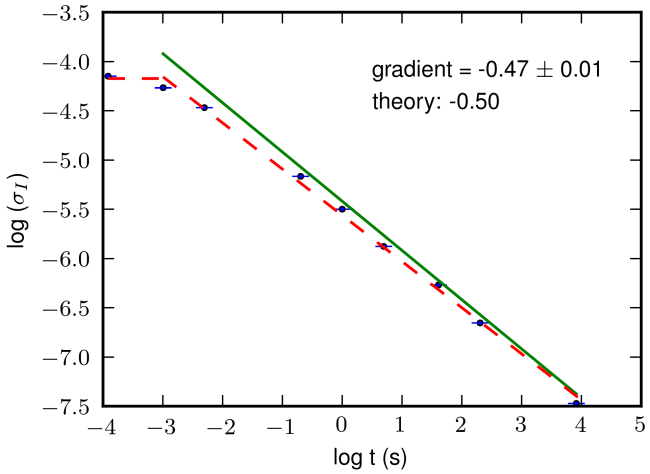

Figure 4.5: Dependence of scintillation index on exposure time showing the simulation results (blue dots) and theory (equation 6.3 – green solid line) for a 0.5m telescope. The red dashed line is the best fit to the simulation points. At very short exposure times, the value for scintillation tends to the short exposure regime.

4.4 The Independence of Scintillation Noise and Photon Noise

Given that shot noise depends on the intensity of the image and since scintillation affects the intensity of the image, it is important to verify that the scintillation noise and photon noise can be treated independently before applying the equations of scintillation to simulate observation. For this test, photon noise, caused by the quantum nature of light, was simulated by assigning photons to the individual images according to equation 3.11 in chapter 3. Random Poisson noise was then applied to each pixel of the output scintillation-containing images from our simulation. The independence of Poisson noise and scintillation was tested by calculating the resulting normalised variance or "equivalent scintillation index" to the result of this full numerical simulation, to combining scintillation and the analytically calculated error due to shot noise in quadrature. We performed this comparison for scintillation resulting from turbulent layer of r_0=10cm, 20cm and 30cm. The simulated and calculated results are all in good agreement, as seen in figure 4.6 for the case of r_0=20cm. This indicates that photon noise and scintillation noise can be added in

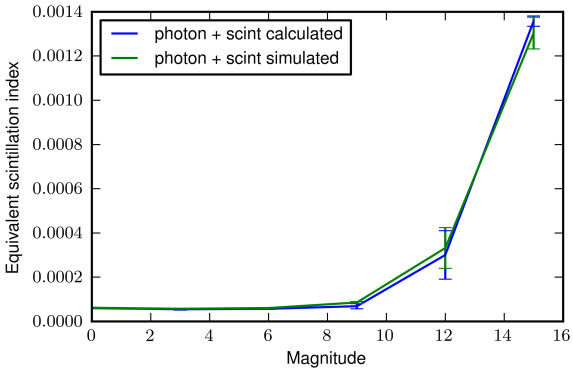

Figure 4.6: Comparison between simulated scintillation and photon noise (blue) and simulated scintillation photon noise added in quadrature (green) for a 0.5m telescope and 1s exposure times for an r_0 of 20cm.

quadrature and treated independently for the range of conditions investigated here.

4.5 Comparison of Sources of Noise on ULTRACAM Photometry

Modern instruments, such as ULTRACAM [40], have a low read-out noise of 3 electrons per pixel. For these instruments, the limiting sources of noise when observing bright targets are photon noise and scintillation. Figure 4.7 shows the relative contribution of scintillation, photon noise, read noise and sky background for ULTRACAM on a 4.2m telescope, when observing an 11th magnitude star in the V-band through a turbulent layer at 10km with an r_0 of 10cm at an airmass of 1.2 and bright moon.

From this, we can see that the relative contribution of read noise and sky background are indeed negligible, and photon noise and scintillation noise are the dominant sources of noise on observation.

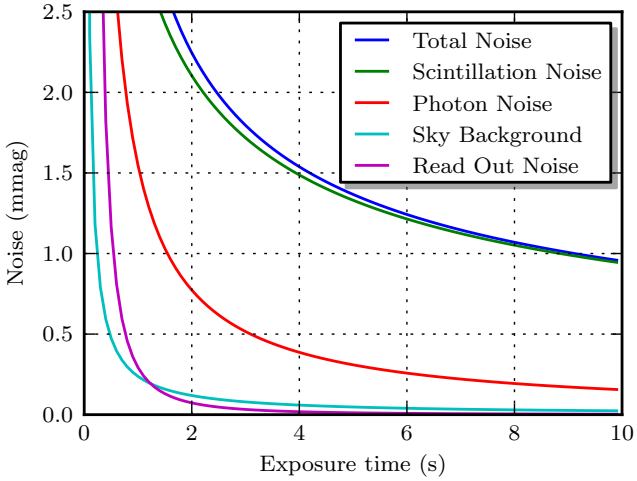

Figure 4.7: Diagram showing the contribution of scintillation noise to photometry compared to photon noise, sky background and read noise as a function of exposure time for a turbulent layer at 10km with $r_0 = 30.7$cm when observing an 11th magnitude target on a 4.2m telescope in the V-band using ULTRACAM. The dominant sources of noise on the observation are photon noise and scintillation.

4.6 When Are Ground-Based Exoplanet Transits Scintillation Dominated?

In this section, we investigate the effect of increasing turbulence strength on the brightness above which scintillation dominates the photometric noise budget. We make the simplifying assumption that all atmospheric scintillation arises from a single high-altitude layer at 10km. Figures 4.8 and 4.9 show the ratio of scintillation noise to photon noise for a 0.5m and 4.2m telescope respectively, for the V-band, with black lines indicating the limit where scintillation becomes the dominant source of noise (i.e. $\sigma_{\rm scint} > \sigma_{\rm phot}$). This is independent of exposure time, as both scintillation noise and photon noise scale as $t^{-1/2}$.

The ratio of scintillation noise to photon noise only has a weak $D^{-1/3}$ dependence, as photon noise scales as D^{-1} and scintillation noise scales as $D^{-2/3}$. Nevertheless, this does have an effect on the magnitude at which scintillation dominates, as seen by the difference between the two figures. For an atmosphere with a turbulence strength of r_0=20cm at 10km, using a 0.5m telescope, scintillation becomes the

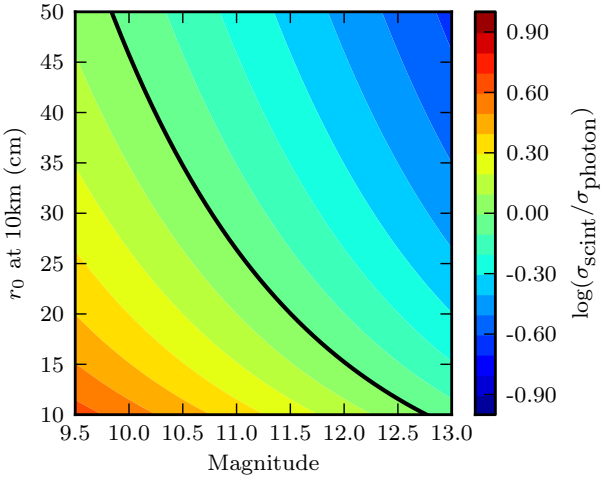

Figure 4.8: Ratio of scintillation noise to photon noise for a 0.5m telescope for varying V-magnitude and r_0 at 10km. The black line shows the boundary for the regime where scintillation becomes the dominant source of noise in photometry.

dominant source of noise at V=11.50, compared to V=13.05 for a 4.2m telescope.

Figure 4.10 shows a histogram of the magnitudes of the currently known transiting exoplanets (as of April 2014)[1]. These exclude the Kepler data, which are all faint. The coloured dashed lines indicate the magnitudes at which scintillation will become the limiting source of noise for varying values of high altitude turbulence, r_0 at 10km, in the visible band. This shows that for an atmosphere with r_0=20cm at 10km, scintillation dominates at $V < 13$, which is the case for $\sim 70\%$ of these planets. For all observations, the elevation of the target significantly effects the contribution of scintillation to the noise. Figure 4.11 shows how the limiting magnitude changes for r_0=20cm for zenith angles of 20°, 40° and 60°. This shows that changing the Zenith distance from 0° to 60° has the effect of shifting the limit where scintillation dominates by 0.7mag.

In table 4.1, we presented the values for the distribution of $C_n^2(10000)$ for the observing site of Observatorio el Roque de Los Muchachos on La Palma. For these measurements, the magnitudes at which scintillation becomes the dominant source of noise on observation is plotted in figure 4.12. This shows that on La Palma, scintillation dominates for targets of magnitude V=10.36 or less, on average.

[1]http://exoplanet.eu

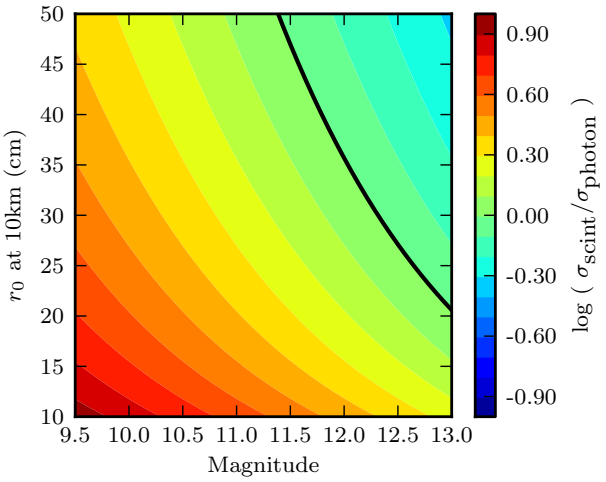

Figure 4.9: Ratio of scintillation noise to photon noise for a 4.2m telescope for varying V-magnitude and r_0 at 10km. The black line shows the boundary for the regime where scintillation becomes the dominant source of noise in photometry.

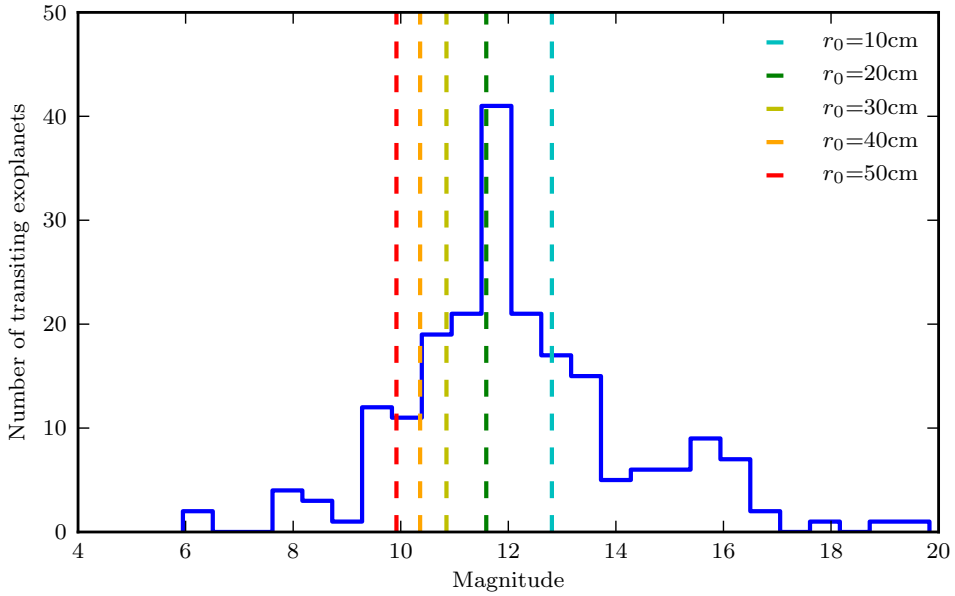

Figure 4.10: Histogram showing the V-band magnitude distribution of known transiting exoplanets. Scintillation noise dominates to the left of the vertical dashed lines, for a 0.5m telescope.

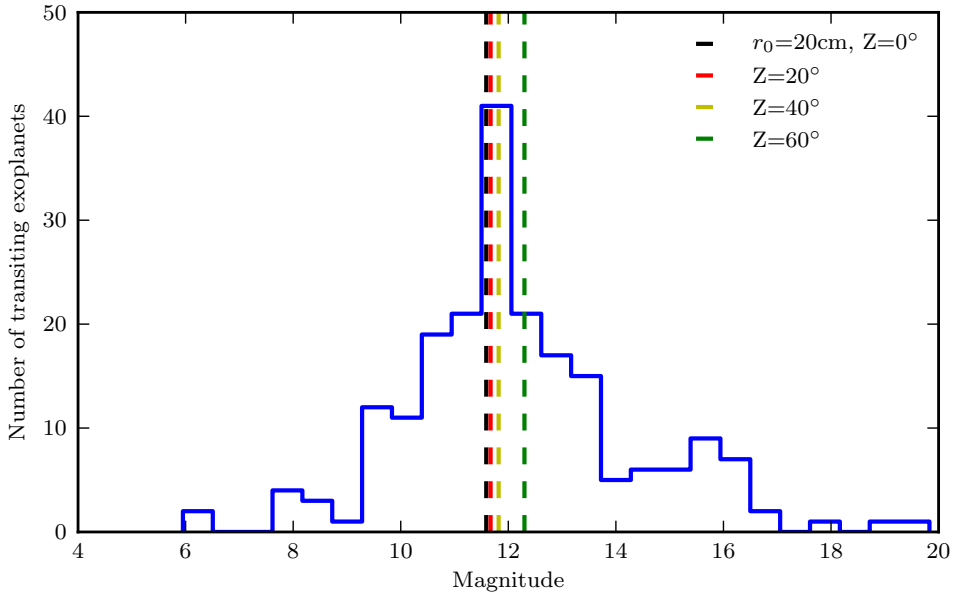

Figure 4.11: Effect of zenith angle on magnitude beyond which scintillation dominates for a 0.5m telescope plotted over the histogram showing the V-band magnitude distribution of known transiting exoplanets. Scintillation noise dominates to the left of the vertical dashed lines.

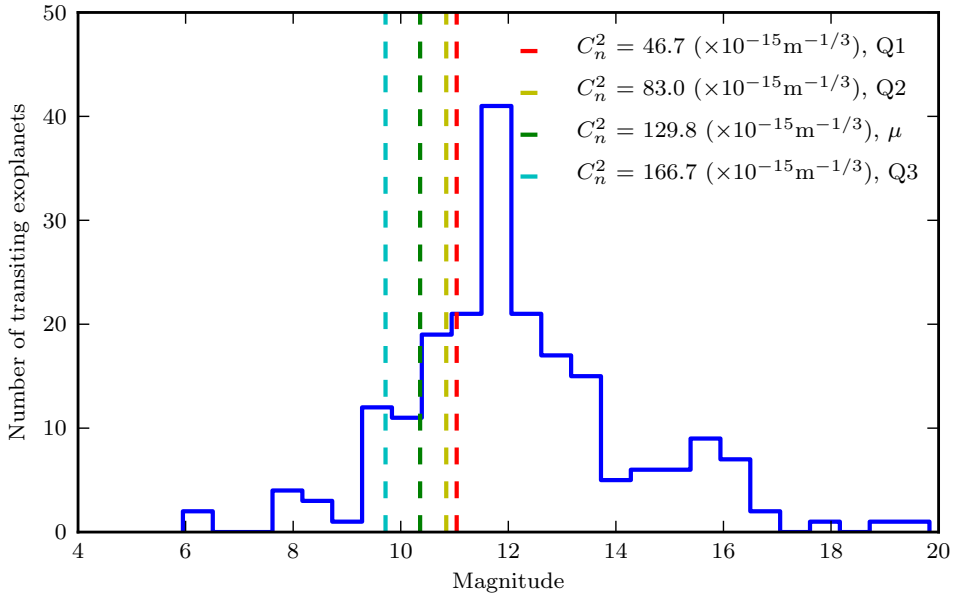

Figure 4.12: Scintillation noise dominates to the left of the vertical dashed lines indicating the $C_n^2(10000)$ for the turbulence profile for La Palma for a 0.5m telescope, plotted over a histogram showing the V-band magnitude distribution of known transiting exoplanets. The dashed lines indicate the first, second and third quartiles and mean of the turbulence distribution.

4.6.1 Scintillation at Near-Infrared Wavelengths

All of the tests performed so far have been for the V-band. In this section, the effect of wavelength on scintillation index is examined and the magnitudes where scintillation dominates are determined as a function of wavelength. Seeing, as quantified by r_0, scales with wavelength as $\lambda^{6/5}$, resulting in better seeing in the infrared than the visible. Scintillation is independent of wavelength when the telescope diameter is much greater than the Fresnel radius, r_F, defined in chapter section 2.3.3, and scales as $\lambda^{-7/6}$ otherwise (equation 2.51). When $D >> r_f$, the size of the individual "flying shadows" is much less than the telescope diameter. The resulting intensity pattern is spatially well averaged within the telescope pupil, rather than being dominated by individual shadows, allowing scintillation noise to be independent of wavelength. As an example, for a dominant turbulent layer at 10km in the K-band, $r_F = 15$cm. For telescope sizes of approximately 1m and larger, scintillation will therefore be largely independent of wavelength, for the visible and infrared.

Measurements of the secondary eclipse require observations in the near-infrared, as the thermal emission of exoplanets are in these wavelengths. In the infrared, thermal emission from the telescope, instrument and sky contribute significantly to noise and cannot be ignored as for optical observations. In the J-band the sky is 1000 times brighter and in the K and H-bands it is 10000 times brighter than in the optical. Previous measurements, by e.g. Wainscoat and Cowie [138] and Phillips et al. [107] show that infrared sky brightness fluctuates by the order of a factor of 2 with time depending on the temperature of the atmosphere, and also varies considerably depending on the observatory site. As such, any calculation involving sky brightness in the infrared can only be approximate.

For the purpose of investigating scintillation towards the near-infrared, we adopt the values stated in figure 4.2. While the value of throughput varies between instrument and waveband, for the purpose of our calculations we have assumed a constant value of 0.4 for the throughput (see section 3.2). Changing the throughput from 0.4 to 0.8 has the effect of shifting the object magnitude where scintillation becomes the limiting source of noise to be fainter by 0.76mag. Figure 4.13 shows how scintillation noise as a fraction of the total noise scales with wavelength for an atmosphere

with r_0=20cm for a 4.2m telescope. The total noise includes the combination of photon noise, sky noise and scintillation noise in quadrature. This figure shows that scintillation continues to be a problem for observations of magnitude $\sim$ 12 or less, even at wavelengths of 2.22μm. Therefore, correction for scintillation in the near infrared is worthwhile.

Band	Central Wavelength (μm)	Bandwidth‡ (μm)	Flux Density* (photons/cm^2/s/Å)	Sky Brightness (mag)
B	0.44*	94	1461	18.4§
V	0.55*	88	999	18.2§
R	0.64*	138	726	17.4§
I	0.79*	149	487	17.9§
z'	0.90§	137	251	18.3§
J	1.26†	213	190	15.3*
H	1.60†	307	92	14.1*
K	2.22†	390	45	11.9*

Table 4.2: Central wavelength, bandwidth, flux density of a mag 0 star above the atmosphere and sky brightness for a bright moon for different colour bands. The z' band is included for comparison with our observation in Chapter 7. Values from * [8], † [17], § [40], * [107], ‡ [9].

4.6.2 The Contribution of Scintillation to Noise on Observation

In the previous part of this section, we have shown scintillation noise relative to other sources of noise. Here, we show the total noise with exposure time and magnitude, in figures 4.14 and 4.15 respectively, calculated for a 4.2m telescope with an exposure time of 6s. Using these values, one can estimate the absolute root-mean-square error for a given observation. The figures show that the total fractional root-mean-square error on an observation is typically of the order of 0.001. The range of possible total

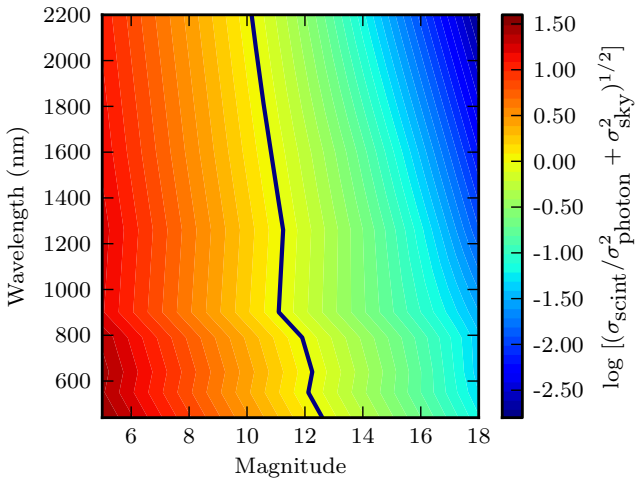

Figure 4.13: Variation of the ratio of scintillation noise to non-scintillation noise with wavelength for 6s exposure times on a 4.2m telescope. The black line shows the magnitude at which scintillation becomes the dominant source of noise. The rapid drop-off in the top-right corner is due to the sky background noise increasing at longer wavelengths.

values for σ_{total} are later used in section 4.7.6 when deciding the range of values for $\frac{\Delta F}{F}/\sigma_{\text{total}}$.

4.7 The Effect of Scintillation on Astrophysical Parameters

In section 4.3, we have shown that our simulations of scintillation match the analytical equations of Kenyon (equation 6.3) well. In this section, we produce simulated transit light curves of example systems to investigate the effect of scintillation noise noise on the astrophysical parameters derived from exoplanet transit light curves. For this, we apply the results from section 2.3.3 that scintillation noise is uncorrelated on the timescales of the observation, is independent of photon noise (section 4.4), and can be expressed by the analytical equation 6.3, assuming a given wind velocity and atmospheric turbulence strength.

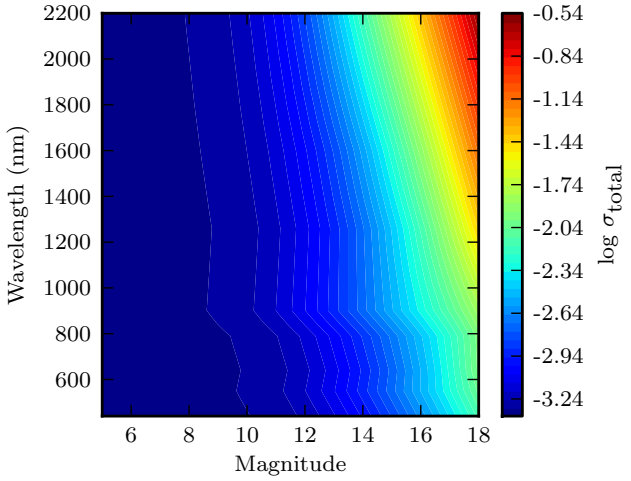

Figure 4.14: Total root-mean-square noise for a 6s exposure on a 4.2m telescope as a function of wavelength.

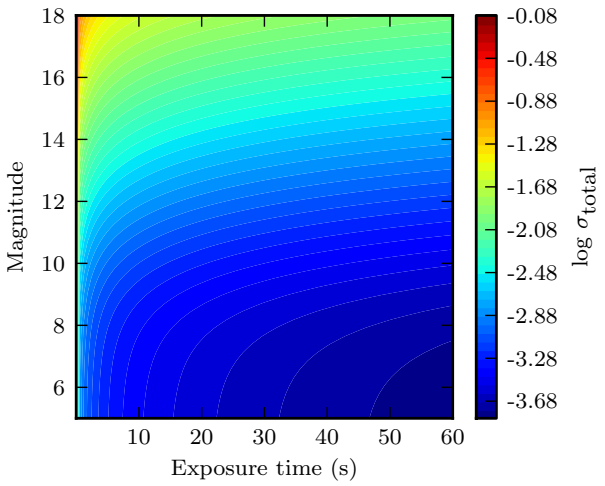

Figure 4.15: Total root-mean-square noise at 550nm on a 4.2m telescope as a function of exposure time.

4.7.1 Modelling Synthetic Transit Light Curves

We generated synthetic light curves for different example real system parameters using the Mandel-Agol [88] analytical expression and a quadratic limb-darkening law (see section 2.2.2). We simulated observational data by taking these model light curves and adding random noise in intervals of exposure times of 6s, typical for transit photometry. The random noise was produced by first scaling the synthetic light curves by the number of photons predicted for the observation, calculated using equation 3.11 and the parameters in table 4.3. From this, we applied Gaussian noise with a standard deviation corresponding to the scintillation index, followed by random Poisson noise to simulate the shot noise.

We subsequently performed Markov-Chain Monte Carlo fits to the data, described in section 2.2.4. Our results were produced from 10 chains of 15000 steps with a burn-in of 1000. We fitted 4 free parameters, the planetary radius, R_p, the stellar radius, R_{star}, the inclination, i, and the limb-darkening coefficient u_2, in accordance with the method outlined in Copperwheat et al. [29]. The mass ratio, period, and offset from time of mid-transit and u_1 were fixed. The literature values for the input parameters were obtained from exoplanet.eu. The observational parameters were set to those typical for an exoplanet observation: summarised by Table 4.3. We note the value chosen for r_0 corresponds to a situation with strong turbulence.

We did not include any airmass variation in our simulated light curves. A threshold was applied where appropriate, e.g. to prevent the inclination from being greater than 90°. The starting parameters for the MCMC were determined by an initial AMOEBA downhill simplex fit. The accuracy of the noise on the data simulated and the χ^2 error contour obtained were compared to the values obtained from observational data of the primary transit of WASP-12b made by [29].

4.7.2 Deep transits

In our first test, we selected five bright targets, where the difference between the in and out of transit brightness is more than 10 millimags: WASP-12b, TrES-3b, HAT-

Parameter	Value
D	4.2m
$t_{\rm exp}$	6s
r_0	0.1m
h	10km
v	10 $\rm ms^{-1}$
λ	550nm
bandwidth	900Å
rate factor	1000
throughput	0.4

Table 4.3: Simulation parameters for MCMC analysis.

P-30-WASP-51b and KELT-3b. We compared the spread of the MCMC fits of the astrophysical parameters on their artificial light curves with and without scintillation noise. An example synthetic light curve is shown in figure 4.16 for WASP-12b, with simulated data, demonstrating the effect of scintillation noise on the scatter. Figures 4.17, 4.18 and 4.19 show the results obtained for WASP-12b for the effect of scintillation noise on the scatter on the parameters of R_{star}/a, i and u_2 as a function of R_p/a. The results are summarised in table 4.4. Of the parameters, removing scintillation has the biggest effect on the limb-darkening coefficient, u_2: removing scintillation improves the error on u_2 by a factor of 5 on average. This is because u_2 has the smallest effect in the overall shape of the light curve, mainly affecting its curvature. For the rest of the parameters, removing scintillation improves the uncertainty by a factor of 4 on average.

While it is currently impossible to completely remove scintillation noise from ground-based photometry, results by Osborn et al. [104] have shown that using the Conjugate-Plane Photometer it is possible to reduce it down to the level of photon noise. Reducing scintillation in this manner could be an effective alternative to placing telescopes in space. The cyan dots in figure 4.16 show the case where scatter on the simulated data of WASP-12b has been corrected down to the level

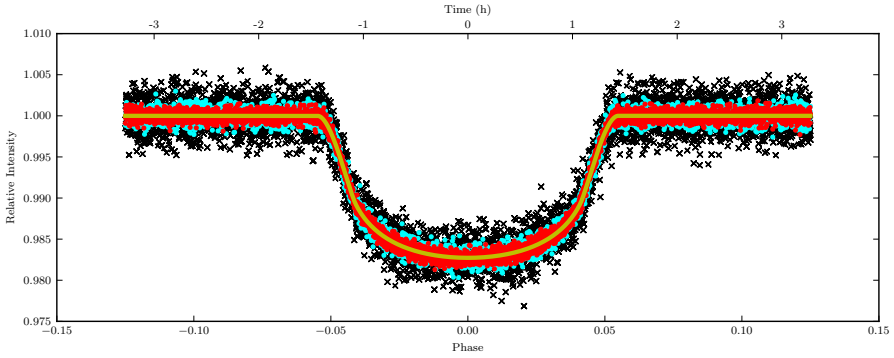

Figure 4.16: Synthetic light curve of the WASP-12b transit in the V band, for a 4.2m telescope under seeing conditions corresponding to an r_0=10cm at 10km. The yellow line shows the simulated light curve and the black crosses indicate simulated data points with photon noise and scintillation based on a 4.2m telescope with a 6s exposure time. The red dots show a light curve without any scintillation noise present, only photon noise. The cyan dots demonstrate a scenario where scintillation has been reduced to the level of photon noise.

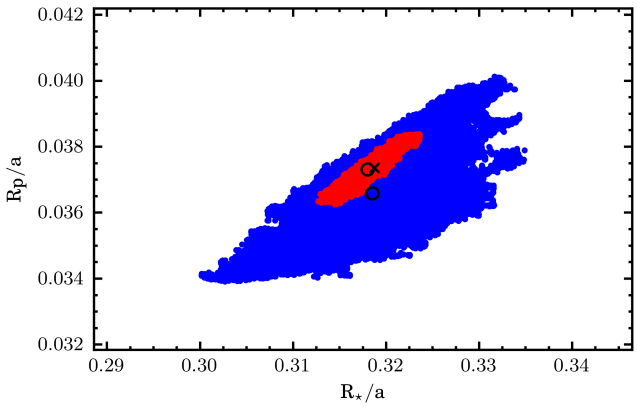

Figure 4.17: The distribution of the results from the MCMC runs for fitting the light curve of WASP-12b in the V-band. The planetary radius, R_p/a, is plotted against the stellar radius, $R_\star/a$. The blue and red points show the distribution of the results with, and without the presence of scintillation, respectively. The blue and red circled points show the mean of the respective distributions, while the black cross shows the starting parameters based on which the the model light curve was produced.

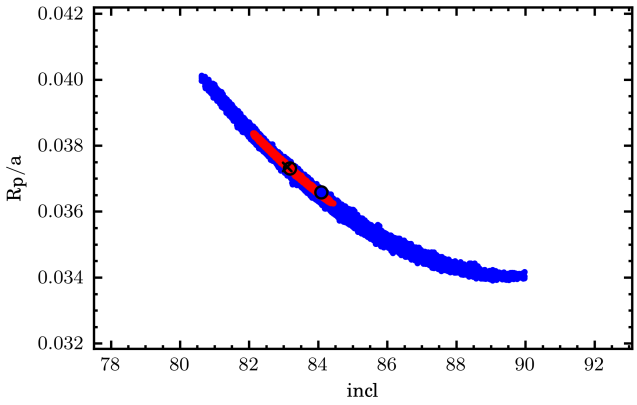

Figure 4.18: The distribution of the results from the MCMC runs fitting the light curve for of WASP-12b for the planetary radius, R_p/a, against the orbital inclination, i. The blue and red points show the distribution of the results with, and without the presence of scintillation, respectively. The blue and red circled points show the mean of the respective distributions, while the black cross shows the starting parameters based on which the the model light curve was produced. The figure shows how the planetary radius is highly correlated with the inclination.

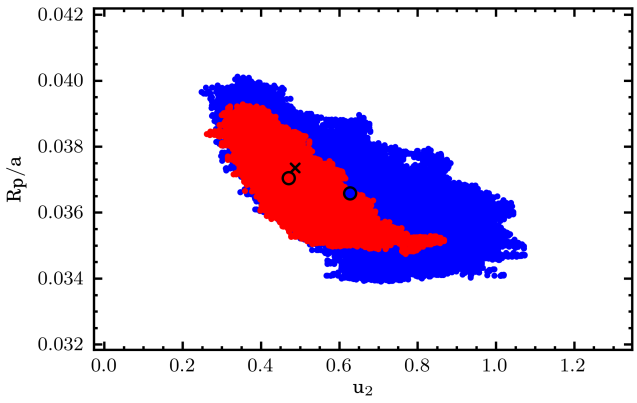

Figure 4.19: The distribution of the results from the MCMC runs for fitting the light curve for of WASP-12b for the planetary radius in units of the semi-major axis, R_p/a, against the limb-darkening coefficient, u_2. The blue and red points show the distribution of the results with, and without the presence of scintillation, respectively. The blue and red circled points show the mean of the respective distributions, while the black cross shows the starting parameters based on which the the model light curve was produced.

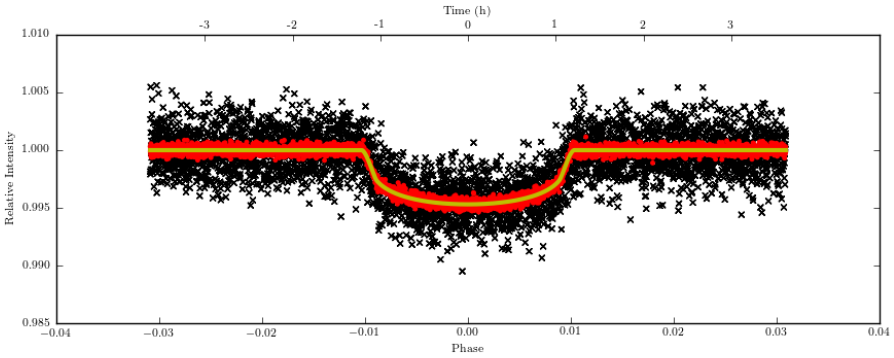

Figure 4.20: Synthetic light curve of the HAT-P-11b transit in the V band, for a 4.2m telescope under seeing conditions corresponding to an r_0=10cm at 10km. The yellow line shows the simulated light curve and the black crosses indicate simulated data points with photon noise and scintillation based on a 4.2m telescope with a 6s exposure time. The red dots show a light curve without any scintillation noise present, only photon noise.

of photon noise. This figure shows that reducing scintillation on bright targets can improve the scatter on the data significantly. The improvements obtained for the four planets investigated when completely removing scintillation and when reducing scintillation down to the photon noise level are also summarised in table 4.4. This shows that for a deep transit, reducing scintillation noise down to the level of photon noise improves the uncertainty of the astrophysical parameters by a factor of 2 on average, producing an improvement half as good as observing from space.

4.7.3 Intermediate and Shallow Transits

We performed the MCMC test for a transit of intermediate depth of 5 milli-magnitudes. Figure 4.20 demonstrates the effect of reducing scintillation noise down to the level of photon noise on the light curve of HAT-P-11b. Figure 4.21 gives an example for the confidence contours obtained for the parameters R_{star}/a vs. R_p/a.

For a shallow transit, where the transit depth is of the order of a milli-magnitude or less, the effect of reducing scintillation for the case of the bright, V=6.3 star HD 97658, and for the fainter, V=11.7 star CoRoT-7b was also investigated. The

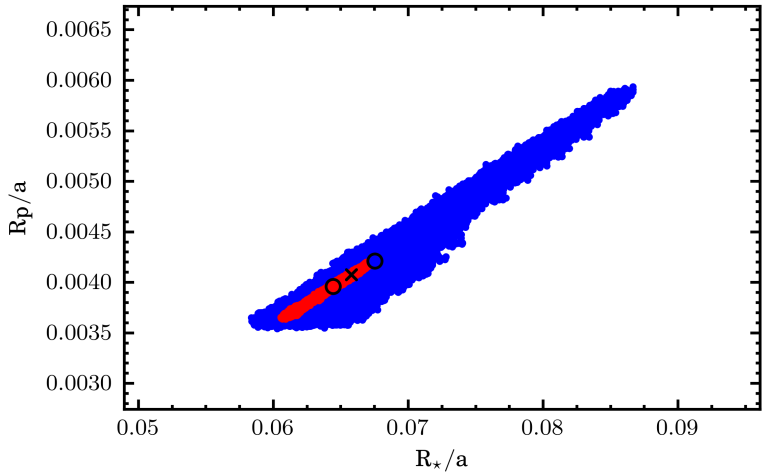

Figure 4.21: The distribution of the results from the MCMC runs for fitting the light curve of HD 97658b in the V band. The planetary radius, R_p/a, is plotted against the stellar radius, $R_\star/a$. The blue and red points show the distribution of the results with, and without the presence of scintillation, respectively. The blue and red circled points show the mean of the respective distributions, while the black cross shows the starting parameters based on which the the model light curve was produced.

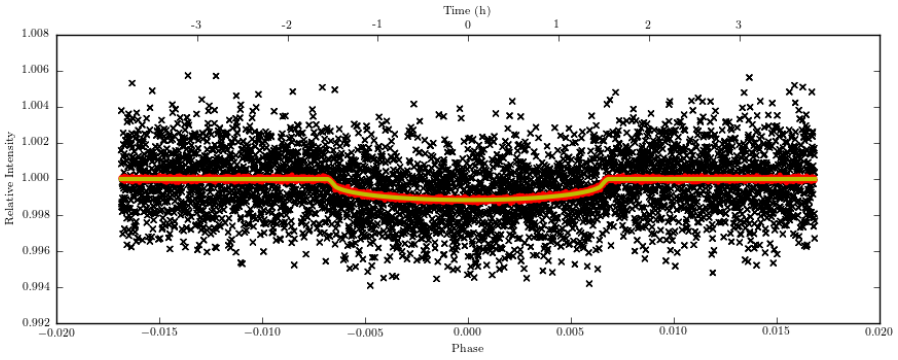

Figure 4.22: Synthetic light curve of the HD 97658b transit in the V band, for a 4.2m telescope under seeing conditions corresponding to an r_0=10cm at 10km. The yellow line shows the simulated light curve and the black crosses indicate simulated data points with photon noise and scintillation based on a 4.2m telescope with a 6s exposure time. The red dots show a light curve without any scintillation noise present, only photon noise.

effect of reducing scintillation to the level of photon noise in the light curve of HD 97658b is demonstrated in figure 4.22. An example of the resulting MCMC fit is shown in figure 4.23. The results of correcting for scintillation for moderate and marginal detection are summarised in table 4.5. The improvement in noise for HAT-P-11b is similar to that of KELT-3b, of comparable brightness, indicating that the improvement is independent of detection depth. For the bright target, HD 97658b, the improvement is up to a factor of 23 for u_2, suggesting scintillation correction can be highly beneficial for bright targets. However, it should be remembered that for the tests, both target and comparison were assumed to be of the brightness of the target star. In practice, it is very difficult to find two stars of V$\sim$ 6 in the same field of view.

4.7.4 Red Optical Wavelengths

The effect of reducing scintillation for HAT-P-11b in the I and z' bands was examined. While scintillation is weaker in these bands, the target is brighter at these wavelengths (V=9.6 compared to z'=7.9), resulting in an overall greater improve-

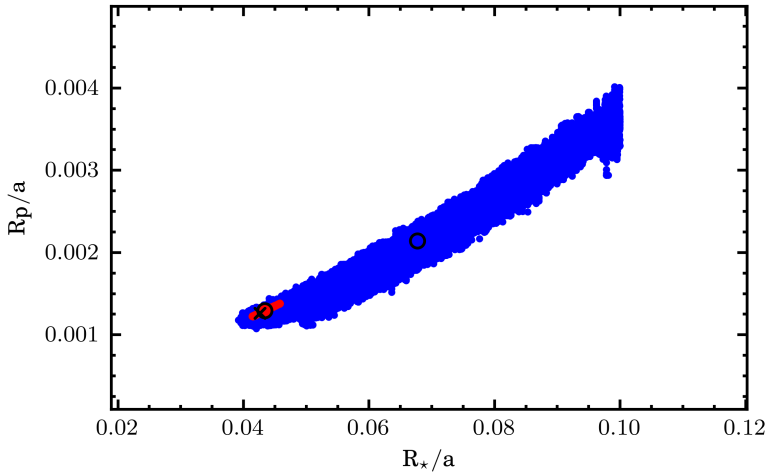

Figure 4.23: The distribution of the results from the MCMC runs for fitting the light curve of HD 97658b in the V band. The planetary radius, R_p/a, is plotted against the stellar radius, $R_\star/a$. The blue and red points show the distribution of the results with, and without the presence of scintillation, respectively. The blue and red circled points show the mean of the respective distributions, while the black cross shows the starting parameters based on which the the model light curve was produced.

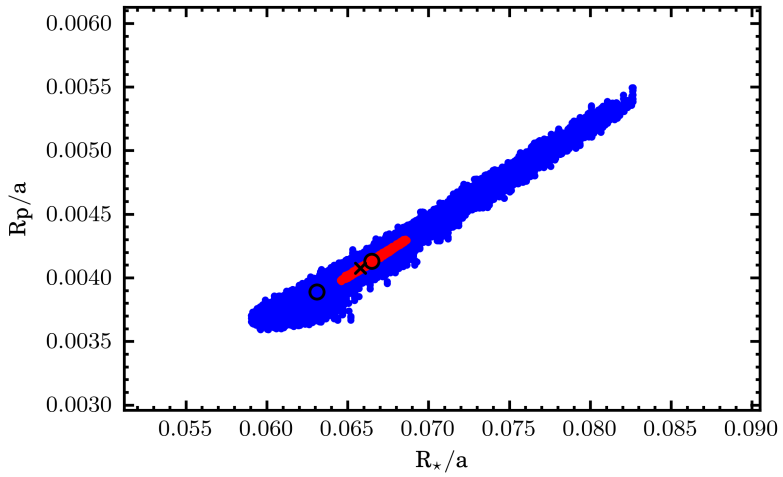

Figure 4.24: The distribution of the results from the MCMC runs for fitting the light curve of HAT-P-11b in the I band for the planetary radius, R_p/a against the stellar radius, $R_\star/a$ a. The blue and red points show the distribution of the results with, and without the presence of scintillation, respectively. The blue and red circled points show the mean of the respective distributions, while the black cross shows the starting parameters based on which the the model light curve was produced.

ment. Figures 4.24, 4.25 and 4.26 illustrate the effect of reducing scintillation down to photon noise level at this wavelength, and the results obtained are summarised in table 4.5. For this target, reducing scintillation in the z' band improves on the uncertainty of the astrophysical parameters by up to a factor of 3, compared to the V band.

4.7.5 The Secondary Eclipse of WASP-12b in the z' band

In this section, we modelled the effect of scintillation noise on the secondary eclipse of WASP-12b in the z' band. The aim of this demonstration is to show that we can simulate the noise on observational data (see chapter 7), and determine the improvement scintillation correction has on a secondary transit. Our free parameters are the eclipse depth and phase offset from transit midpoint (see section 2.2.3). In order for the light curve to be directly compared to the data obtained in chapter 7, we scaled the mean of the simulated light curve to that of our raw data, and set the length of the out-of-transit regions of the light curve to be of similar length

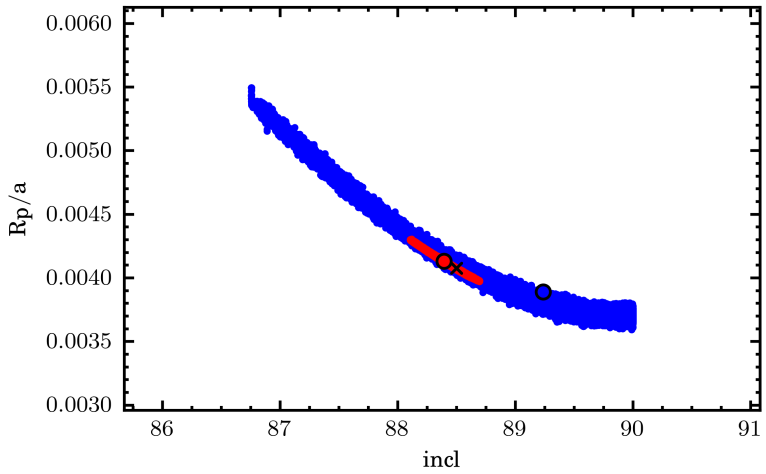

Figure 4.25: The distribution of the results from the MCMC runs for fitting the light curve of HAT-P-11b in the I band for the planetary radius, R_p/a against i. The blue and red points show the distribution of the results with, and without the presence of scintillation, respectively. The blue and red circled points show the mean of the respective distributions, while the black cross shows the starting parameters based on which the the model light curve was produced.

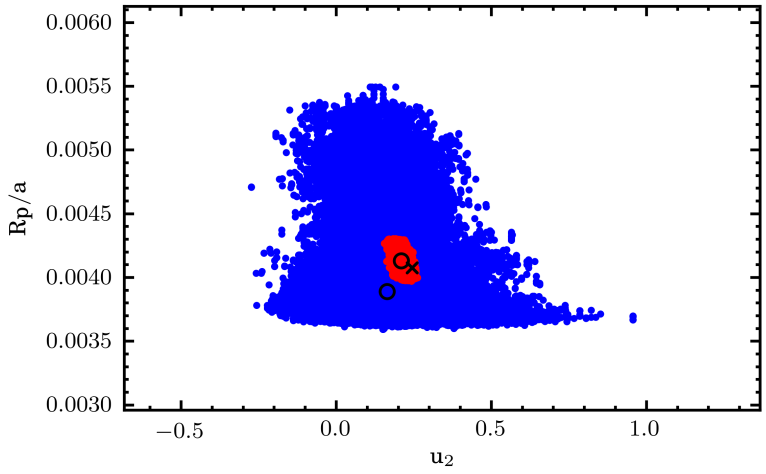

Figure 4.26: The distribution of the results from the MCMC runs for fitting the light curve of HAT-P-11b in the I band for the planetary radius, R_p/a against u_2. The blue and red points show the distribution of the results with, and without the presence of scintillation, respectively. The blue and red circled points show the mean of the respective distributions, while the black cross shows the starting parameters based on which the the model light curve was produced.

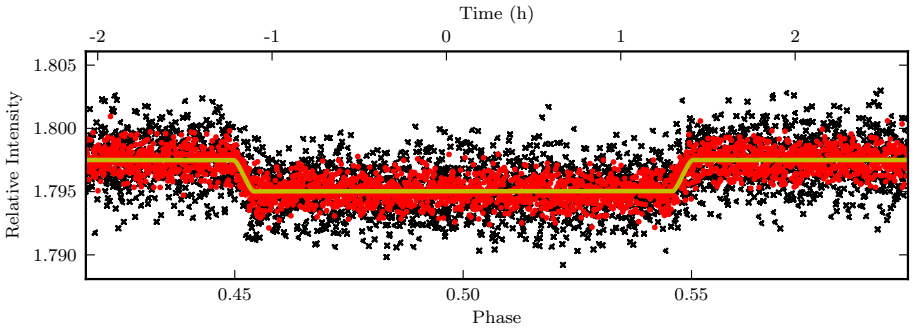

Figure 4.27: Synthetic light curve of the WASP-12b secondary eclipse in the z' band, for a 4.2m telescope under seeing conditions of r_0=20cm at 10km. The yellow line shows the simulated light curve and the black crosses indicate simulated data points with photon noise and scintillation. The red dots show a light curve without any scintillation noise present, only photon noise.

as in our observation. Figures 4.27 and 4.28 show the simulated light curve and resulting contour plots respectively. We find that the scatter on the simulated data is well matched to the scatter on the observational data of the secondary eclipse of WASP-12b on the WHT (see chapter 7). This shows that using the equation 6.3 and the value of the average turbulence profile, we can make a good estimate of the scintillation noise on observational data. However, this is not a rigorous comparison; for a more accurate comparison see chapter 6. For this data, scintillation causes an increase in uncertainty in the astrophysical parameters by a factor of 1.5, identical to the improvement obtained for the R_p/a parameter for the transit of WASP-12b.

4.7.6 Generalised Results

Up to now, we have shown the improvement on the astrophysical parameters with improving scintillation for specific cases. In this section, we generalise the results obtained. Different scenarios where scintillation is a varying fraction of the total noise were explored, based on the possible values found in figure 4.13. For a transit observation, the quality of the data can be quantified by the ratio of relative change in flux to noise, or $\frac{\Delta F}{F}/\sigma$. Here, F is the total flux from the system and ΔF is the observed change of flux during the transit and σ_{tot} is the total root-mean-square noise. This way, the effect of increasing the contribution of scintillation noise to

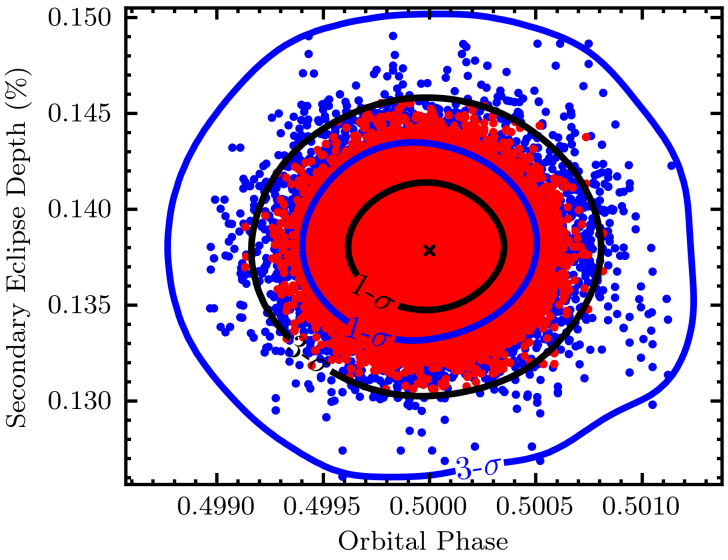

Figure 4.28: The distribution of the results from the MCMC runs for fitting the secondary eclipse light curve of WASP 12b in the z' band for the eclipse depth and orbital phase. The blue and red points show the distribution of the results with, and without the presence of scintillation, respectively. The black cross shows the starting parameters based on which the the model light curve was produced and the black and blue contours show the 1-σ and 3-σ confidence contours for the red and blue distributions respectively.

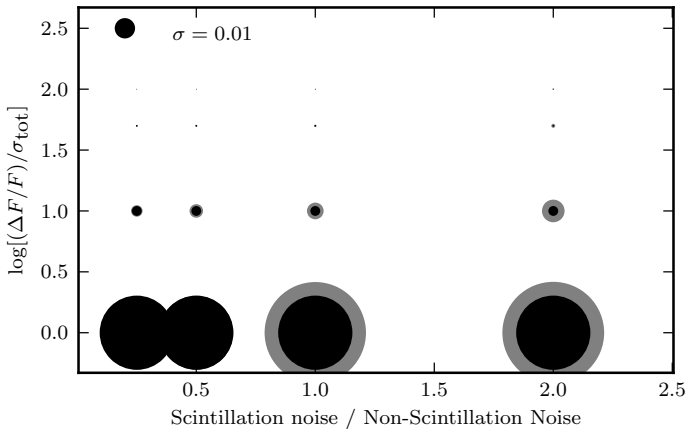

Figure 4.29: The effect of scintillation noise on the size of the one standard deviation error on the planetary radius, R_p/a. The black circles indicate the size of 1 standard deviation error without scintillation noise for varying fractional transit depth expressed in units of $\sigma_{\rm total}$. The grey circles indicate the size of 1 standard deviation error due to the amount of scintillation expressed on the x-axis.

a system of known $\frac{\Delta F}{F}/\sigma_{\rm tot}$ can be investigated, through the effect it has on the standard deviations of the astrophysical parameters of the system.

Simulated light curves were created for values of $\frac{\Delta F}{F}/\sigma_{\rm tot}$ of 1, 10, 50 and 100, corresponding to eclipse depths between 0.1 - 10 millimag for values of $\sigma_{\rm other}$ of 0.0003 that is obtained for an observation of $t_{\rm exp} = 6$s, $D = 4.2$m and V=11.69mag. This was converted to a ratio of eclipse depth to noise according to $\frac{\Delta F}{F} = 1 - 2.5^{-\Delta m}$. The ratios of scintillation to non-scintillation noise were varied between 0.25 - 2. The results were obtained from 30 Markov-Chains of 15000 steps and a burn-in of 1000. Figures 4.29-4.32 show the fraction of the noise on the astrophysical parameters due to scintillation as a function of relative eclipse depth, $\frac{\Delta F}{F}/\sigma$, and scintillation fraction. The radius of the circles correspond to one standard deviation of the distribution of the parameters examined.

From these diagrams we can get a visual representation of the effect of scintillation noise on the astrophysical parameters. The standard error on these results is 10%. The results show that the worsening of the scatter of the astrophysical parameters is directly proportional to the increase of scintillation noise in the light curves for all parameters.

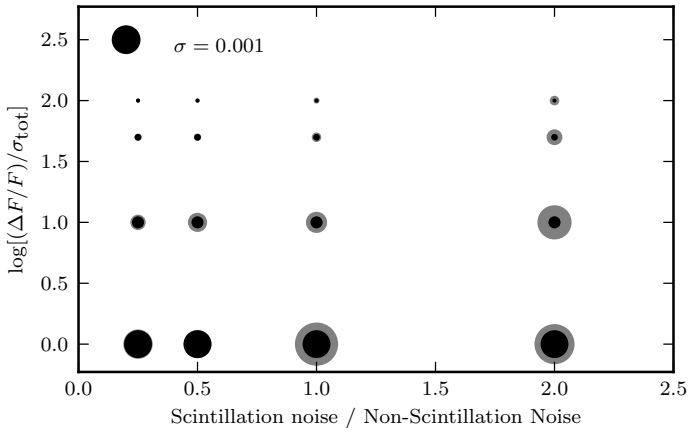

Figure 4.30: The effect of scintillation noise on the size of the one standard deviation error on the stellar radius, $R_\star/a$. The black circles indicate the size of 1 standard deviation error without scintillation noise for varying fractional transit depth expressed in units of $\sigma_{\rm total}$. The grey circles indicate the size of 1 standard deviation error due to the amount of scintillation expressed on the x-axis.

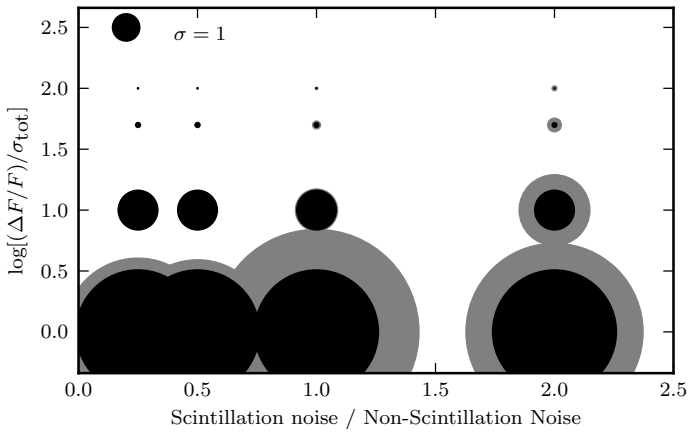

Figure 4.31: The effect of scintillation noise on the size of the one standard deviation error on the inclination. The black circles indicate the size of 1 standard deviation error without scintillation noise for varying fractional transit depth expressed in units of $\sigma_{\rm total}$. The grey circles indicate the size of 1 standard deviation error due to the amount of scintillation expressed on the x-axis.

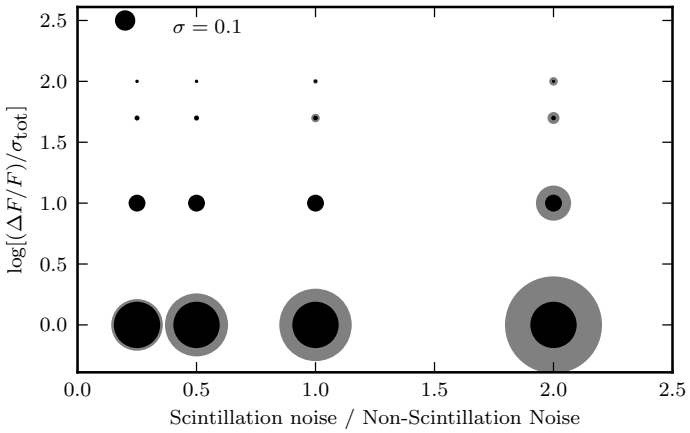

Figure 4.32: The effect of scintillation noise on the size of the one standard deviation error on the limb-darkening coefficient. The black circles indicate the size of 1 standard deviation error without scintillation noise for varying fractional transit depth expressed in units of $\sigma_{\rm total}$. The grey circles indicate the size of 1 standard deviation error due to the amount of scintillation expressed on the x-axis.

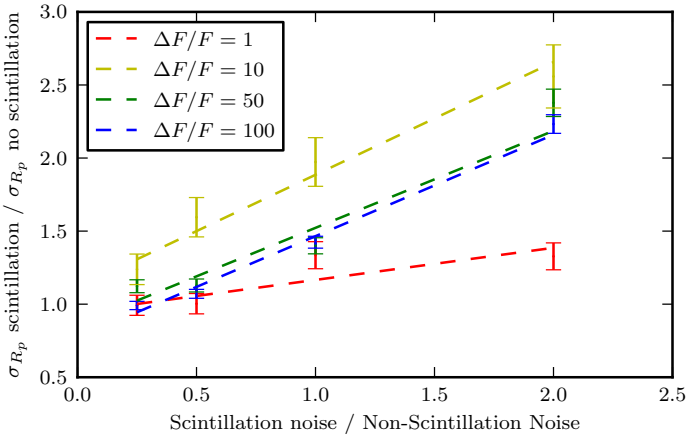

Figure 4.33: Relative change of noise on planetary radius as a function of the relative change of noise on light curve, for different values of $\Delta F/F$.

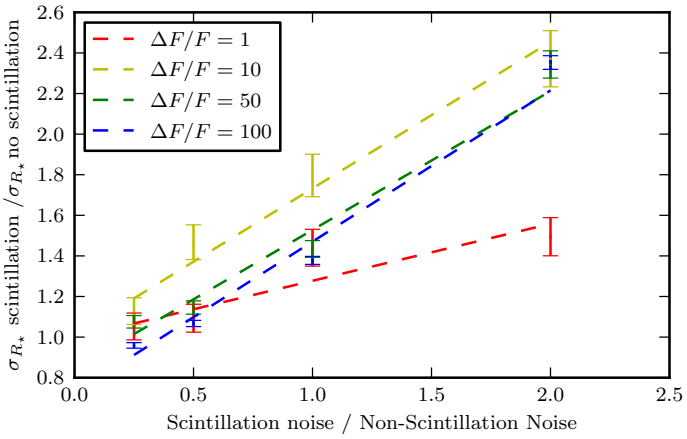

Figure 4.34: Relative change of noise on stellar radius as a function of the relative change of noise on light curve, for different values of $\Delta F/F$.

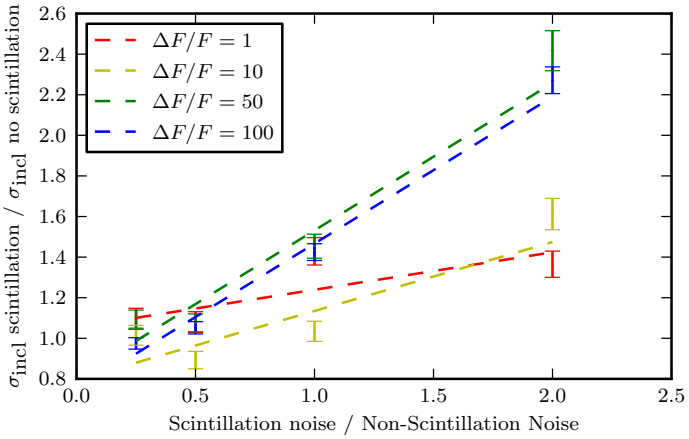

Figure 4.35: Relative change of noise on orbital inclination as a function of the relative change of noise on light curve, for different values of $\Delta F/F$.

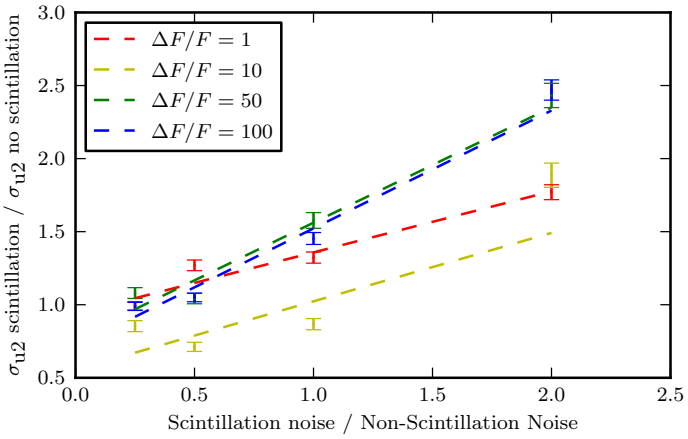

Figure 4.36: Relative change of noise on the limb-darkening coefficient as a function of the relative change of noise on light curve, for different values of $\Delta F/F$.

Figures 4.33-4.34 give the summary of the MCMC results obtained. They show that the noise on the astrophysical parameters scale similarly with scatter on the light curve. On average, the noise on the astrophysical parameters varies linearly with the scatter on the light curves with a gradient of 0.73. This means that reducing the noise on light curve by a factor of 2 causes a factor of $\sim$1.5 reduction on the noise on all astrophysical parameters. However, for lower S/N, the improvement of the noise on the parameters with the reduction of scintillation is much less. This is because for low S/N, the extent of the scatter is limited by the boundary conditions imposed in the simulation (e.g. inclination must never exceed 90°). The average gradient for each individual parameter is presented in table 4.6. When calculating the average, only gradients where $\Delta F/F$ was large enough so that the boundary conditions do not limit the full extent of the scatter were used.

4.8 Summary

In this chapter we investigated the effect of scintillation noise on ground-based transit photometry by simulation. We found that scintillation becomes the limiting source of noise for targets brighter than $V = 10.4$ for the average value of turbulence measured for a 0.5m telescope at La Palma. We compared our simulation to analytical expressions and found them to be in good agreement. We showed that

by calculating scintillation index based on the average atmosphere model of Dravins et al. [44], we underestimate the scintillation noise for La Palma by a factor of 2 on average. We examined the effect of scintillation on the astrophysical parameters for transit and secondary eclipses in the visible and red-optical. We found that overall, the errors on the light curve arising from scintillation increase linearly the scatter on the astrophysical parameters within a gradient in the range of 0.68 – 0.80.

System	Properties			Improvement Factor							
				Scintillation Removed				Scintillation = photon noise			
	V mag	$R_p/R_\star$	$\sigma_{\rm scint}/\sigma_{\rm total}$	R_p/a	$R_\star/a$	incl	u_2	R_p/a	$R_\star/a$	incl	u_2
KELT-3b	9.8	0.092	0.99	4	5	6	7	3	3	4	4
WASP-51b	10.42	0.103	0.98	4	4	4	5	1.5	1.4	2	2
WASP-12b	11.69	0.117	0.95	3	3	4	6	1.5	1.4	2	2
TRES-3b	12.4	0.164	0.91	3	4	2	3	2	2	2	2

Table 4.4: Exoplanetary systems with values of $R_p/R_\star > 0.9$, and hence $\Delta F/F$ of 0.008, or greater. Together with the brightness of the targets, this produces a deep detection of 10millimag or more (see section 4.7.2). The table shows the magnitude, planet-to-star radius ratio, fraction of scintillation noise to total noise for the case of a 4.2m telescope, 6s exposure time and seeing of r_0=10cm at 10km. Detector and sky parameters are negligible compared to scintillation and photon noise and not included. The results for the ratio of the standard deviation of the MCMC distribution for light curves with and without scintillation, as well as with scintillation reduced to the level of photon noise are presented for the free parameters: planetary radius R_p/a, stellar radius $R_{\rm star}/a$, inclination and limb-darkening coefficient. The values for the ratios were obtained from the average of 10 Markov-Chains of 15000 steps with a burn-in of 1000. The typical standard deviation between chains is 1.

System		Properties			Improvement Factor			
	Band	Magnitude			Scintillation = photon			
		in band	$R_p/R_\star$	$\sigma_{\rm scint}/\sigma_{\rm total}$	R_p/a	$R_\star/a$	incl	u_2
HAT-P-11b	V	9.59	0.062	0.992	4	4	3	7
HAT-P-11b	I	8.2	0.062	0.997	5	5	7	9
HAT-P-11b	z'	7.9	0.062	0.998	10	9	11	23
HD 97658b	V	6.27	0.030	0.9996	18	16	5	23
HD 97658b	I	6.84	0.030	0.9992	14	14	8	15
COROT-7b	V	11.7	0.017	0.95	1.2	1.3	1.2	2

Table 4.5: Exoplanetary systems with values of $R_p/R_\star < 0.6$, and hence $\Delta F/F$ of 0.004, or greater. Together with the brightness of the targets in the visible and infrared, this produces an intermediate or shallow detection (see section 4.7.3). The table shows the magnitude, planet-to-star radius ratio, fraction of scintillation noise to total noise for the case of a 4.2m telescope, 6s exposure time and seeing of r_0=10cm at 10km. Detector and sky parameters are negligible compared to scintillation and photon noise and not included. The results for the ratio of the standard deviation of the MCMC distribution for light curves with and without scintillation, as well as with scintillation reduced to the level of photon noise are presented for the free parameters: planetary radius R_p/a, stellar radius $R_{\rm star}/a$, inclination and limb-darkening coefficient. The values for the ratios were obtained from the average of 10 Markov-Chains of 15000 steps with a burn-in of 1000. The typical standard deviation between chains is 1.

Parameter	Dependence on Scatter of Light Curve
R_p/a	0.679 ± 0.008
$R_\star/a$	0.714 ± 0.006
incl	0.72 ± 0.01
u_2	0.80 ± 0.01

Table 4.6: Dependence of astrophysical parameters on scatter on light curve.

Chapter 5

Aperture Photometry and Speckle Noise

Aperture photometry is the standard method for measuring object flux from astronomical CCD images. Photometric observations allow us to gain useful information about the properties of exoplanets, including the radius, semi-major axis, inclination, temperature and periodicity (see section 2.2.2). It is expected that the photometry procedure contributes to the noise on observation, and because of this, we investigate its effect using simulation. This chapter is divided into two parts: the first part describes the procedure for performing aperture photometry, and the second part is an investigation into the effect of "speckle noise", noise caused by the speckling of the point spread function (PSF) due to seeing. For this, we investigate the size of the photometry aperture required to optimise the effect of speckle noise through simulation.

5.1 Aperture Photometry

The simplest technique for carrying out photometry is through aperture photometry, which involves counting the total flux contained within a circle, or *aperture*, around the object in the image. There are three main steps involved in performing photometry: finding the object centre, measuring the sky background level and calculating the flux of the object. Figure 5.1 shows an example of of aperture photometry being

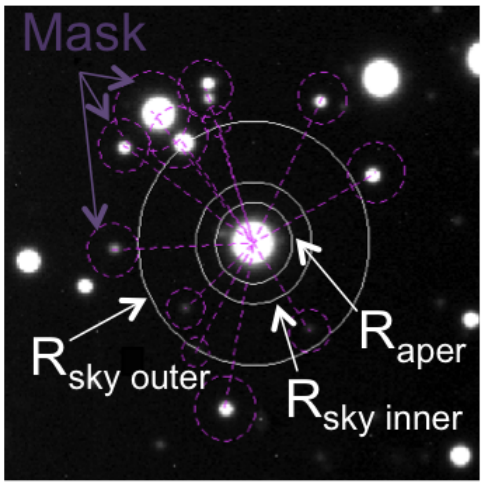

Figure 5.1: Aperture photometry carried out on a CCD image of WASP-12. The total flux from the target is measured from the innermost white circle, $R_{\rm aper}$. The signal from the sky is measured using a median or clipped mean from the sky annulus defined by the two outer circles $R_{\rm sky\ inner}$ and $R_{\rm sky\ outer}$. In a crowded field, fainter background stars are masked out of the sky area, shown by the dashed magenta circles.

performed on an object.

A second way of obtaining the total signal from a target is through profile fitting, whereby the PSF of a star is fitted by a matching mathematical function. The flux is obtained from the integrated area under the function. Profile fitting is not suitable for use for exoplanet photometry where the images are often heavily defocussed so that the PSF shape resembles more a "doughnut" than a Moffat profile. This is done to allow longer integration times without saturation and to reduce the effects of pixel sensitivity variations across the stellar profile [128].

5.1.1 Object Centering

The search for the centre of the PSF begins with an initial manual input of the centre of the search. Within a search radius, several methods can be used to locate the image centre. The simplest method used in turbulence profiling, is the location of the image *centroid*. For a PSF described by a function $I(x, y)$, the centroid in the

x-direction is defined as

$$\text{cen}_x = \frac{\int x\ I(x,y)\ dx\ dy}{I_{tot}}, \tag{5.1}$$

where I_{tot} is the total flux within the search area. This method is implemented when searching for the image centre in the latter part of the chapter.

A more robust way of obtaining the object centre is through fitting a function, such as a Moffat distribution, defined as [94]:

$$f(r) = \frac{h}{(1 + (r/\alpha)^2)^\beta}, \tag{5.2}$$

where h determines the height and α the width of the fit. A Moffat profile has more extended wings than a Gaussian, due to the extra parameter β, which controls the extent of the wings. The estimate for the centre of the PSF is then obtained from the centre of the profile. This method is implemented in all the analysis performed on exoplanet transits.

5.1.2 Sky Background Estimation

Measuring and subtracting the sky background is a necessary step in photometry, which ensures any gradient present in the sky background is removed. The sky background is estimated from the flux inside an annulus placed around the object. The size of the annulus needs to be carefully chosen so that it is large enough to provide a good statistical measurement of the sky brightness, but not so big for the background level to be contaminated by neighbouring stars. In crowded fields, it is unavoidable to have a few faint background stars fall within the sky annulus. In this case, the background stars can be masked out so as not to be included in the sky background estimate. The inner radius of the sky aperture is chosen to be larger than the photometry aperture, to avoid contamination of light from the target star. A robust way of measuring sky background is via a "clipped mean" method, where values that are more than 3σ from the mean are rejected and then refit. This removes the possibility of contamination from cosmic rays, hot pixels and faint stars.

5.1.3 Flux measurement

Measurement of flux is typically done by comparing the flux of the target relative to the flux of one or more comparison stars. The process is called *differential photometry*. Note that differential photometry can not be used to correct for scintillation effects, as the size of the isoplanatic patch is too small ($\sim$ 0.6") in the optical and infrared compared to the typical separation of the source and calibration stars (typically 1' or more). The flux of the target is simply the sum of the signal from each pixel inside the aperture, with the sky background subtracted. Finding the best size for the aperture is one of the main concerns in aperture photometry. This size needs to be chosen so that as much light from the star as possible is included within the aperture. However, too large an aperture will be contaminated by neighbouring objects and the sky, and have increased detector noise. An optimum aperture size of around 1.5 times the full width at half maximum (FWHM) of the target was determined by Naylor [96]. It is critical to use the same radius of aperture for both target and comparison, so that the same percentage of light is lost out of the aperture.

5.2 Speckle Noise

In chapter 2, we have shown that the PSF is built up from many instantaneous speckle images. For very poor values of seeing, the PSF can even appear amorphous, which may skew the centroid position. At any one point in time, if the aperture size is chosen to be too small, seeing will cause some of the speckles to fall outside of the aperture. A different fraction of light will fall outside the target aperture to the comparison star aperture i.e. the shape of the PSF at the source and calibrator are different, as it is outside the isoplanatic patch. This contributes an additional source of intensity fluctuations in the observation, which is not accounted for in a standard error budget. In contrast to scintillation noise, which originates in the pupil plane, the source of speckle noise is in the image plane. For this reason, speckle noise results from turbulence at all altitudes, including the ground-layer, whereas scintillation only results from the high layers. Figure 5.2 is an illustration of an aperture placement where some of the speckles from the image fall outside of the

photometry aperture.

5.2.1 Instantaneous Intensity Variance

The effect of changing the photometry aperture was investigated for a simulated turbulence with $r_0 = 10$cm at 10km altitude using a 2m telescope. The amount of intensity variance in the image, σ_2, was measured inside a photometry aperture centred at the centroid of the image PSF, for instantaneous exposures ($t_{\text{exp}} = 0.01\text{ms} \ll V_\perp/D$ see section 2.3.3). Figure 5.3 shows the diagram of intensity variation against aperture size as a fraction of the theoretical seeing FWHM.

The figure indicates that speckle noise is significant up to aperture radii of 2.5× the FWHM. This means that in 1" seeing, ensuring that the photometry aperture is at least 2.5" large will guarantee that the effect of aperture noise is negligible. This value is small compared to the photometry aperture sizes used in aperture photometry. For example, in a 1" seeing, for a plate scale of 0.3"/pixel, the FWHM is 3.3 pixels across, so having a photometry aperture of at least 4.2 pixels radius will ensure that speckle noise is negligible. Increasing the aperture much further than this value is not advised, as it will cause the sky and detector noise to increase.

5.2.2 Finite Exposure Time Intensity Variance

The normalised intensity variance inside a photometry aperture was investigated in a similar manner to the previous section, but for finite exposure times, instead of instantaneous intensities. For this, several instantaneous speckle images were averaged to obtain the desired exposure time (see section 2.3.2).

The Power within the Photometry Aperture

The flux inside the photometry aperture and the normalised intensity variances were compared in the presence and absence of scintillation. Seeing without scintillation corresponds to a situation where strong ground-layer turbulence dominates. The perturbed wavefront is not far enough from the observer to be able to propagate and develop into scintillation, but it does contribute to the corrugation of the PSF.

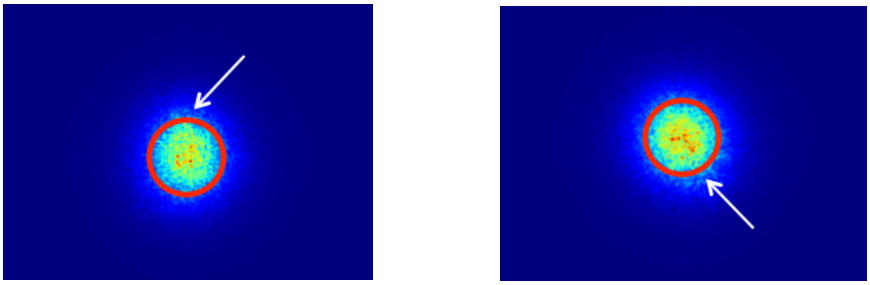

(a)

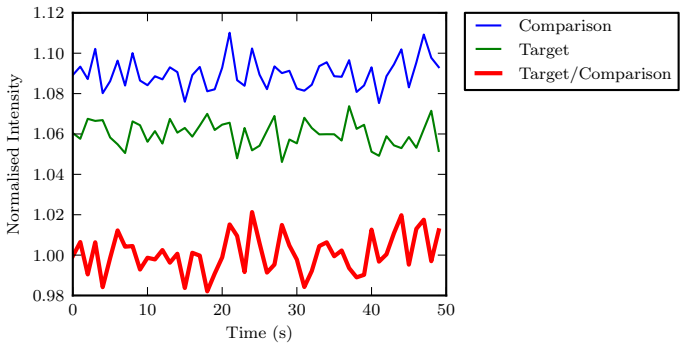

(b)

Figure 5.2: False-colour images of two simulated, 1s exposure images of a star with a photometry aperture in red demonstrating the process of differential aperture photometry (figure a). The intensities have been arbitrarily offset for clarity. The arrow shows some of the speckles falling outside of the photometry aperture due to seeing and scintillation. Figure b shows the corresponding intensity variations measured. As we are only investigating the effect of speckle noise in this section, effects due to shot noise from the target and sky, and detector noise have not been included. The red line shows the final intensity measured after performing differential photometry. The intensities have been arbitrarily offset for clarity.

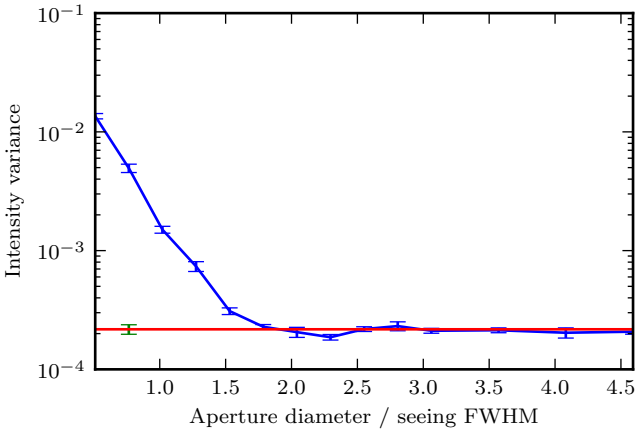

Figure 5.3: Normalised intensity variance of a PSF within an aperture as a function of aperture diameter, in units of seeing FWHM (blue line). At small aperture diameters, the intensity variance is dominated by speckle noise. Past a critical radius, the intensity variations reach the scintillation noise floor (red line).

The simulations performed were for a turbulence strength of $r_0 = 10$cm at 10 km height for 0.5s exposures using a 2m telescope. The telescope diameter was chosen to be as large as possible, without being computationally cumbersome. The exposure time was chosen to be long enough for $t_{\text{exp}} > D/V_{\perp}$. Each point consists of the average of 20 intensity variances each obtained from 100 images, for aperture radii increasing in 0.25" increments.

Figure 5.4 shows the results obtained. From this we can see that, on average, the measured fraction of flux contained within the aperture is identical for both scintillation and non-scintillation scenarios. This is expected, as scintillation does not affect the shape of the seeing disc. We found that for aperture radii of 12×FWHM or greater, more than 99% of the flux is contained within the aperture. In the absence of scintillation, increasing the photometry aperture size will continue to improve the normalised intensity variance, although beyond 6×FWHM improvement is negligible. In the presence of scintillation, intensity variance is initially identical to the non-scintillation case, as in both instances the speckle noise dominates for small apertures. However, at aperture sizes of 2.5×FWHM, speckle noise becomes negligible compared to scintillation noise (seen where the blue and red lines

intersect).

5.2.3 Exposure Time and Turbulence Strength Dependence

We investigated the effect of speckle noise as a function of exposure time and turbulence strength. Figures 5.5 - 5.7 show the amount of normalised intensity variance due to speckle noise for values of r_0 of 5cm, 10cm and 20cm at 10km, respectively. The figures were created by measuring the average of 20 intensity variances each obtained from 100 images, for aperture radii increasing in 10 pixel increments. The radius where aperture noise becomes negligible compared to the scintillation is measured from the horizontal line on the plots where the intensity variance does not increase further with increasing aperture radius. For very strong values of the turbulence strength, parameterised by a single layer of r_0=5cm at 10km, the speckle noise is found to be present at aperture sizes of around 6.5×FWHM. For strong turbulence of r_0=10cm at 10km, speckle noise is present up to aperture sizes of 4.0×FWHM and for average levels of turbulence up to 2.3×FWHM.

Speckle Noise in Differential Photometry

During differential photometry, the normalised variances combine according to standard error propagation. For targets of equal magnitude, this means that the normalised variance increases by a factor of two. The dashed cyan line in figure 5.4 shows the normalised variance calculated for differential photometry of the data for blue line from simulation.

5.3 Conclusion

In this chapter, the procedure for performing aperture photometry was described. The concept of speckle noise was introduced and discussed. The effect of the noise due to aperture photometry was investigated for both instantaneous (0.01s) and short finite exposure times (up to 0.5s) using simulation. It was found that for finite exposure times in good seeing speckle noise contributes to noise in photometry for aperture sizes of up to approximately 2.3×FWHM.

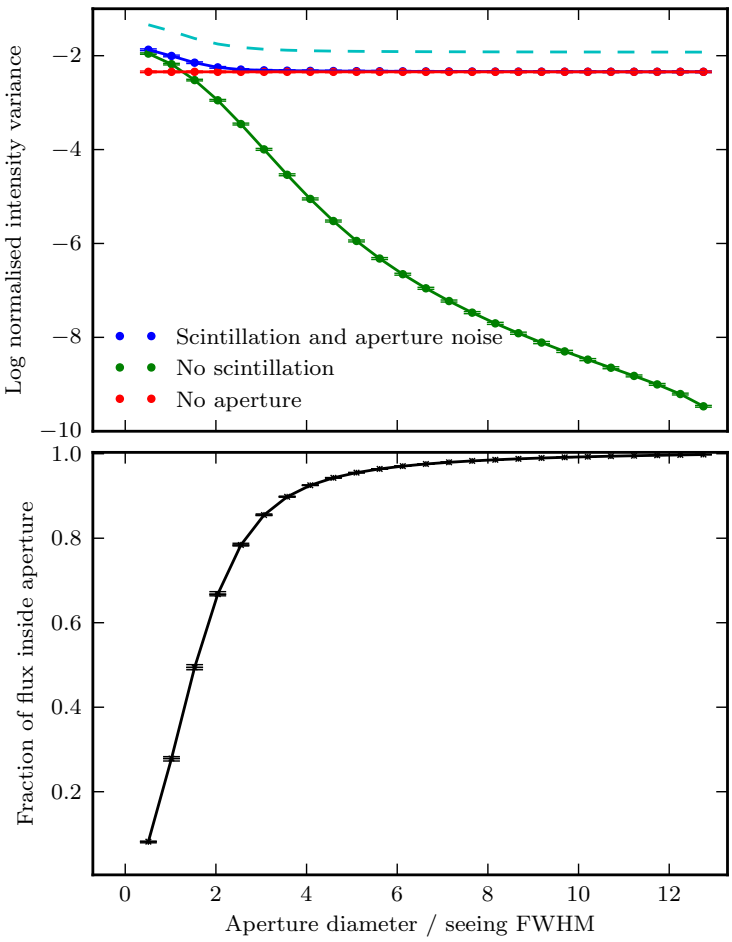

Figure 5.4: Normalised intensity variance (top panel) and flux enclosed (bottom panel) within the photometry aperture as a function of aperture size, for an exposure time of 0.5s with a strong turbulence profile of r_0=10cm. In the top panel, the red line represents the scintillation limit, the blue line shows the intensity variance due to the photometry aperture in the presence of scintillation and the green line shows the effect of the photometry aperture in the absence of scintillation. The cyan dashed line shows the normalised intensity variance for differential photometry. The resulting variance is 2 times that of the variance on the individual images. The bottom panel shows that the flux enclosed within the photometry aperture in the presence and absence of scintillation as a function of aperture size are identical.

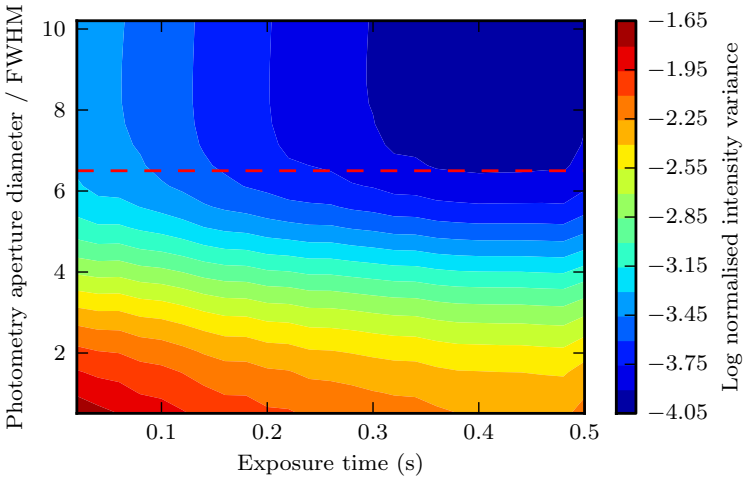

Figure 5.5: Normalised intensity variance as a function of photometry aperture radius size and exposure time, for a very strong turbulence profile of r_0=5cm at 10km. The red line indicates where vertical cross-section of the intensity variance flattens out for longer exposures, indicating that speckle noise is present up to an aperture size of around 6.5×FWHM.

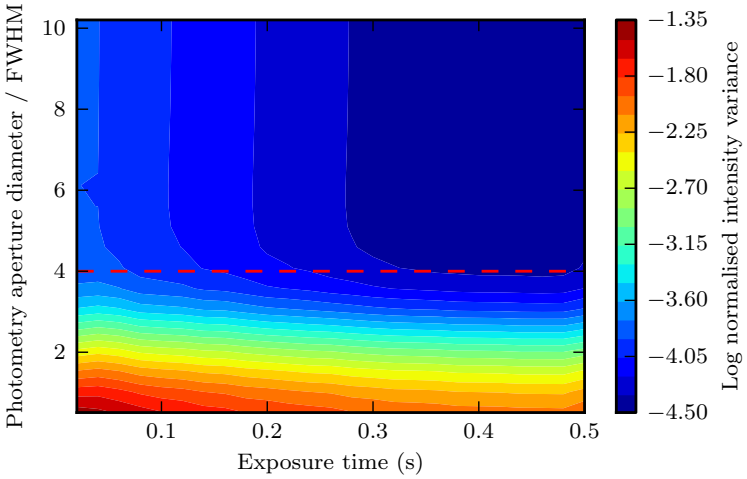

Figure 5.6: Normalised intensity variance as a function of photometry aperture radius size and exposure time, for a strong turbulence profile of r_0=10cm at 10km. The red line indicates where vertical cross-section of the intensity variance flattens out for longer exposures, indicating that speckle noise is present up to an aperture size of around around 4.0×FWHM.

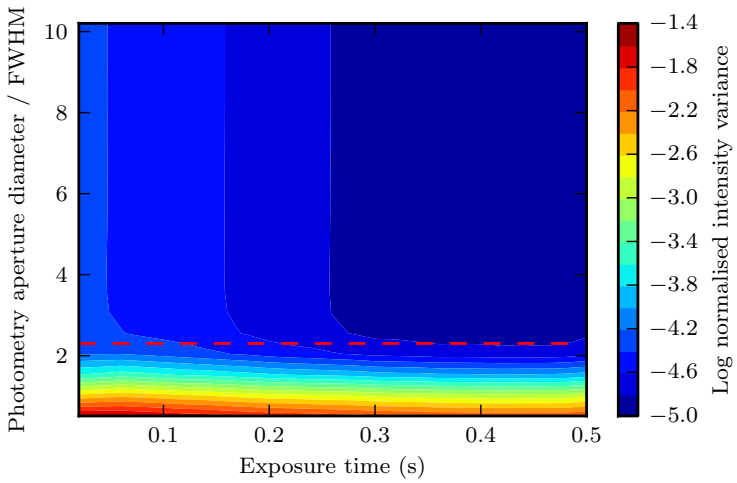

Figure 5.7: Normalised intensity variance as a function of photometry aperture radius size and exposure time, for a weak turbulence profile of r_0=20cm at 10km. The red line indicates where vertical cross-section of the intensity variance flattens out for longer exposures, indicating that speckle noise is present up to an aperture size of around 2.3×FWHM.

Chapter 6

Turbulence Profiling for the Prediction of Scintillation Noise

6.1 Introduction

The ability to predict the amount of noise in observations due to scintillation, given an understanding of the atmosphere, is a crucial test for our understanding of scintillation. An accurate real-time knowledge of the amount of noise due to scintillation can aid a more efficient scheduling of observations. In this chapter, we investigate the effect of scintillation on observations, by comparing estimates of scintillation from turbulence profiling using SCIDAR on the 1.0m Jacobus Kapteyn Telescope (JKT) and the 2.5m Isaac Newton Telescope (INT) on La Palma with measurements of the intensity variations obtained from simultaneous photometry using ULTRACAM on the 4.2m William Herschel Telescope (WHT) and the 0.5m Durham-Sheffield robotic telescope, *pt5m*, on the same site. The results of three nights of simultaneous observation on the 2013-07-20, 2014-03-15 and 2014-03-16 are presented. The ULTRACAM observations were taken by Vik Dhillon, and the reduction and analysis performed by the author. The SCIDAR observations were taken by James Osborn and the author, with the reduction of the data to obtain $C_n^2(h)$ profiles and velocity measurements performed by James Osborn.

6.2 The Stereo-SCIDAR Instrument

The stereo-SCIDAR is an optical triangulation technique, described in detail in Osborn et al. [103] and Shepherd et al. [125], based on SCIDAR (SCIntillation Detection And Ranging) [72] [50] and the instrument design of the Conjugate-Plane Photometer by Osborn et al. [102]. A schematic of the Stereo-SCIDAR configuration is shown in figure 6.1. Part of the incoming light from a binary star, with an angular separation of θ passes through the same high altitude turbulent layer, at an altitude h. The resulting intensity pattern at the telescope aperture contains two copies of the same wavefront aberration separated by a distance $h\theta$. The turbulence strength and wind direction are determined from the covariance of the intensity patterns measured for each star. Mathematically, for two random variables X and Y, the covariance is defined as

$$\mathrm{cov}(X, Y) = \langle (X - \mu_X)(Y - \mu_Y) \rangle = \langle XY \rangle - \mu_X \mu_y, \tag{6.1}$$

where $\mu_X = \langle X \rangle$ and $\mu_Y = \langle Y \rangle$ are the respective means. The *spatial cross covariance* is the measure of the strength of correlation between two fields at the same time, but separated in space. In the spatial covariance function of the images, there will be a peak corresponding to the separation $h\theta$, with the amplitude related to the turbulence strength. The *temporal auto covariance* of an image is the covariance of one image with itself with a time offset. Measurement of the temporal covariance allows the calculation of the velocity of the turbulent layer as it crosses the field of view of the telescope pupil.

6.3 Turbulence Profiling using Stereo-SCIDAR

Due to the requirement for the projection of the telescope aperture at the turbulent layer to overlap for the two stars, the maximum height a layer can be observed using stereo-SCIDAR is $h_{\max} = D/\theta$, where D is the diameter of the telescope. The field of view of the stereo-SCIDAR instrument on the INT is 1', allowing the observation of targets of typical angular separation 25" − 30" and the measurement of layers of heights up to 26km. An example of the typical pair of raw pupil-plane images

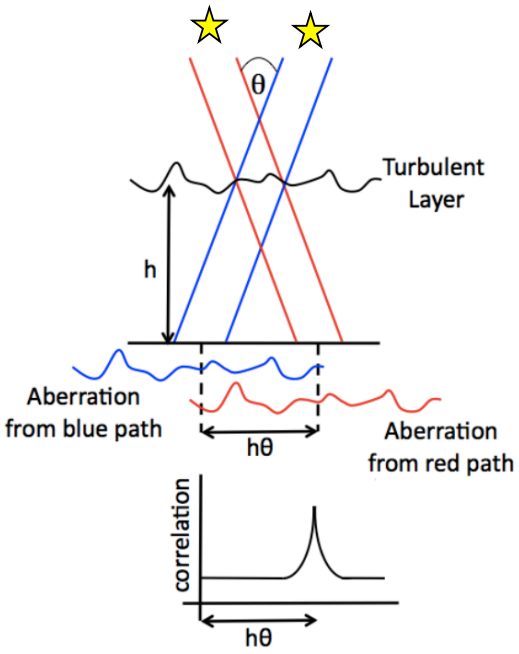

Figure 6.1: Schematic illustrating the Stereo-SCIDAR principle. Light from a double star of angular separation θ passes through a turbulent layer at height h. Within the instrument, the pupil images are separated onto two detectors. A part of the light from the two stars travels through the same patch of turbulence, causing the same aberration to appear in both pupil images separated by a distance $h\theta$. The amplitude of the turbulence is determined by the amplitude of the correlation peak. *Diagram from [100].*

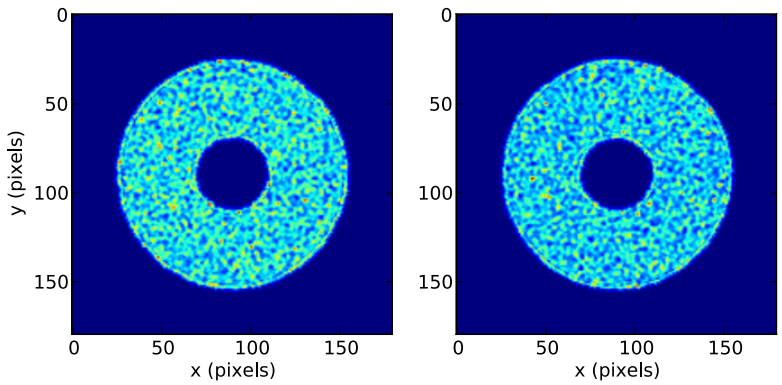

Figure 6.2: Pupil images of a double star recorded using stereo-SCIDAR on the INT.

measured by the stereo-SCIDAR is shown in figure 6.2. These pupil images are normalised and their spatial cross-covariances are calculated. Figure 6.3 shows a typical covariance.

For a single turbulent layer, the normalised spatial cross covariance function $B(\vec{r})$ is related to the refractive index structure constant, $C_n^2(h)$ via [125]

$$B(\vec{r},z) = 3.9\times10^{-2}2\pi k^2 C_n^2 \mathrm{d}h \int_0^\infty f^{-8/3}\sin^2(\pi\lambda Z f^2) J_0(2\pi r f)\mathrm{d}f \qquad (6.2)$$

where k is the wave-number of the light from the star, f is the spatial frequency of the atmospheric turbulence, λ the wavelength, Z is the zenith angle and J_0 a Bessel function of the first kind. C_n^2 is adjusted to the zenith by dividing by the airmass.

The height of the turbulence is determined from the distance of the covariance peak from the centre, r, through $h = r/\theta$. The conversion between r in pixels and metres is obtained from the resolution of the pupil, n_{pup}, as $r(\mathrm{m}) = r(\mathrm{pixel})\times D/n_{\mathrm{pup}}$.

Wind velocities of the strongest turbulent layers are obtained by calculating the temporal cross-covariance function of the frames with a time delay. Wind speed and direction are obtained from measuring vectors between the peaks in cross-covariance

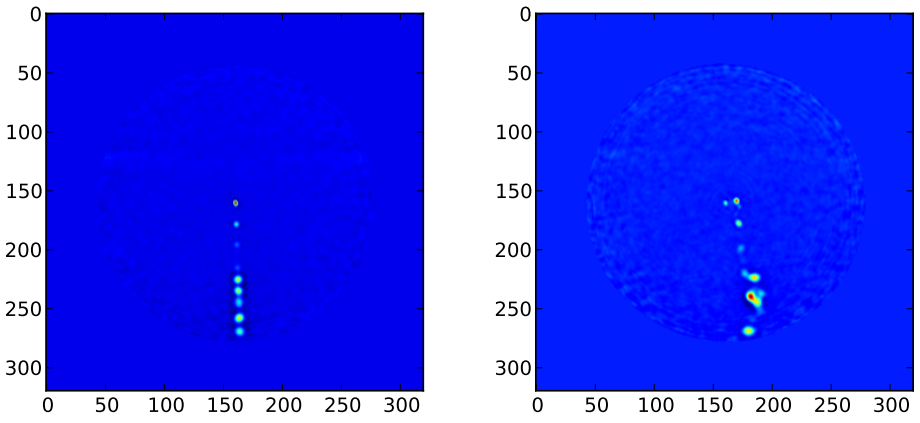

(a) (b)

Figure 6.3: Cross-covariance functions between pupil images. Hotter colour corresponds to stronger correlation. (a) shows the instantaneous cross-covariance between the pupils. The magnitude of the covariance peak is related to the refractive index structure constant, $C_n^2(h)$, whilst the distance from the centre of the plot at (160,160) is related to the altitude of the turbulent layer. (b) shows the cross-covariance between one of the pupils and the other shifted in time by 20ms. Measuring the magnitude and direction of the shift of the peak from the origin gives a value for the wind velocity associated with each turbulent layer.

of temporally adjacent frames. The speed is simply the length of the vector, $\bar{v}$, in metres divided by the time delay. The wind direction is determined from the angle between the new position of the peak in the cross-correlation plot and the old position at vertical, $\theta_{\rm xcov}$. During observation, the double star is aligned perpendicular to the parallactic angle, PA. The wind direction, θ_v, is then given by $\theta_v = PA + \theta_{\rm xcov}$. The wind velocity, v, is measured in the plane of the pointing of the telescope. It is converted to the perpendicular velocity at zenith, $V_\perp$, through $V_\perp = V/\cos(\theta_{\rm xcov})$.

6.4 Scintillation Index from Turbulence Profiles

Given the measurement of $C_n^2(h)$ and $V_\perp(h)$ from SCIDAR, the expected scintillation index for a photometric observation on a telescope of diameter D, exposure time $t_{\rm exp}$ and zenith angle Z can be calculated from [69],

$$\sigma_{\rm scint} = 10.7 \left[\int_0^\infty \frac{C_n^2(h) h^2}{V_\perp(h)} {\rm d}h \right]^{1/2} D^{-2/3} t_{\rm exp}^{-1/2} \cos(Z)^{-3/2}. \qquad (6.3)$$

The total expected noise, σ_I is obtained by combining the estimates for photon noise and system noise with $\sigma_{\rm scint}$ for both target and comparison in quadrature.

6.5 Scintillation Estimates from SCIDAR

In order to make estimates of the scintillation index, an accurate profile of the wind speeds of every layer is needed. Velocity estimates are only possible when the covariance peaks in both frames can both be distinctively resolved by the SCIDAR algorithm. This means that only the strongest layers, approximately 6% of the total C_n^2 measurements have velocities associated with them. For the rest of the measurements of C_n^2, a wind velocity was assigned based on the average velocity of the layer. This was obtained as follows: The SCIDAR wind velocity estimates for the entire night are combined and sorted by height. The list of velocities is divided into layers, shown in figure 6.4. Layer boundaries are placed if no wind velocity is detected for 100m above the last measured velocity. Typically, around 40 layers are distinguished each night. During the course of a night, the wind velocity for a given

height is assumed constant, and calculated from the average of the measured wind velocities within each layer. For values of C_n^2 where wind velocities were detected, these were left unchanged. Anomalous wind velocities resulting from difficulty of the SCIDAR algorithm to detect cross-covariance peaks were excluded during a second pass. An anomalous wind velocity was defined as a single point possessing a velocity of 6kms^{-1} more than its neighbouring points. These points were replaced by the average of the neighbouring four points.

We chose to express scintillation noise measured by SCIDAR as $\sum C_n^2(h)h^2/V_\perp$. Recalling equation 6.3, these are the parameters that determine scintillation index which arise from the atmosphere and are not dependent of the observation. Figures 6.5 - 6.7 show the turbulence profiles and corresponding vertical wind profiles obtained on the nights beginning of 2013-07-20, 2014-03-15 and 2014-03-16, together with the calculated velocity profiles and $C_n^2(h)h^2/V_\perp$ profiles.

6.6 Noise Measurements on ULTRACAM Photometry

The photometry from ULTRACAM and the *pt5m* telescope was corrected for bias and flat-field, and aperture photometry was performed using the ULTRACAM pipeline written by Tom Marsh[1]. The differential flux of the two brightest stars in the field for each data set was obtained in the r' band, by optimising the aperture radii in order to produce the light curve with the least amount of scatter in the out-of-transit region. Not all data obtained contained a transit, some were bright binaries or exoplanets not undergoing a transit at the time. If the data contained a transit, a full light curve fit was performed, and the data was divided by the fit. The light curve was calculated using the Mandel and Agol [88] analytical equations with quadratic limb darkening with 6 free parameters for the planetary and stellar radii, inclination, limb darkening coefficient, offset from predicted transit mid-time and two airmass coefficients, as in Chapter 4. Normalising the data in this way was necessary to obtain the correct estimate of the standard deviation. If left uncor-

[1]http://deneb.astro.warwick.ac.uk/phsaap/software/ultracam/html/index.html

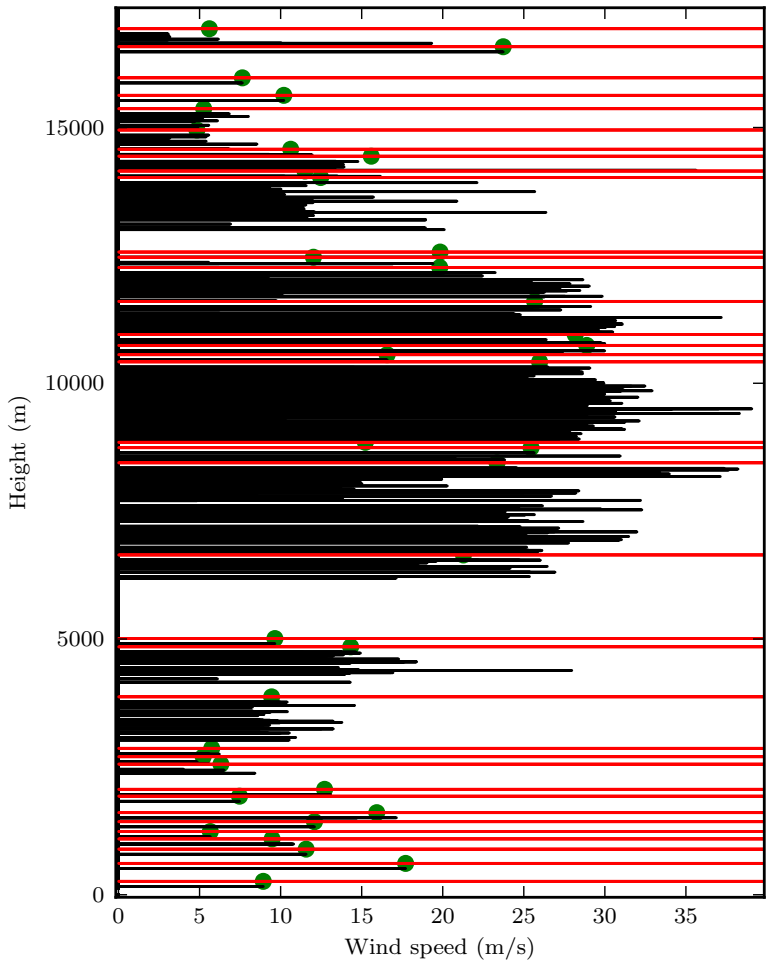

Figure 6.4: Wind speeds as a function of height for the night of 2014-03-13, used for estimating the wind speeds at each layer. The black horizontal lines represent the magnitude of the wind velocities measured at the corresponding altitude, summed over the entire night. The red horizontal lines represent the heights at which a layer boundary was detected. A layer boundary was placed if there is a gap of more than 100m in height between subsequent detected wind velocities. The boundary is placed (100m above the last measurement. The green dots on each red line represent the value of the average velocity that was assigned to each layer below a given boundary line.

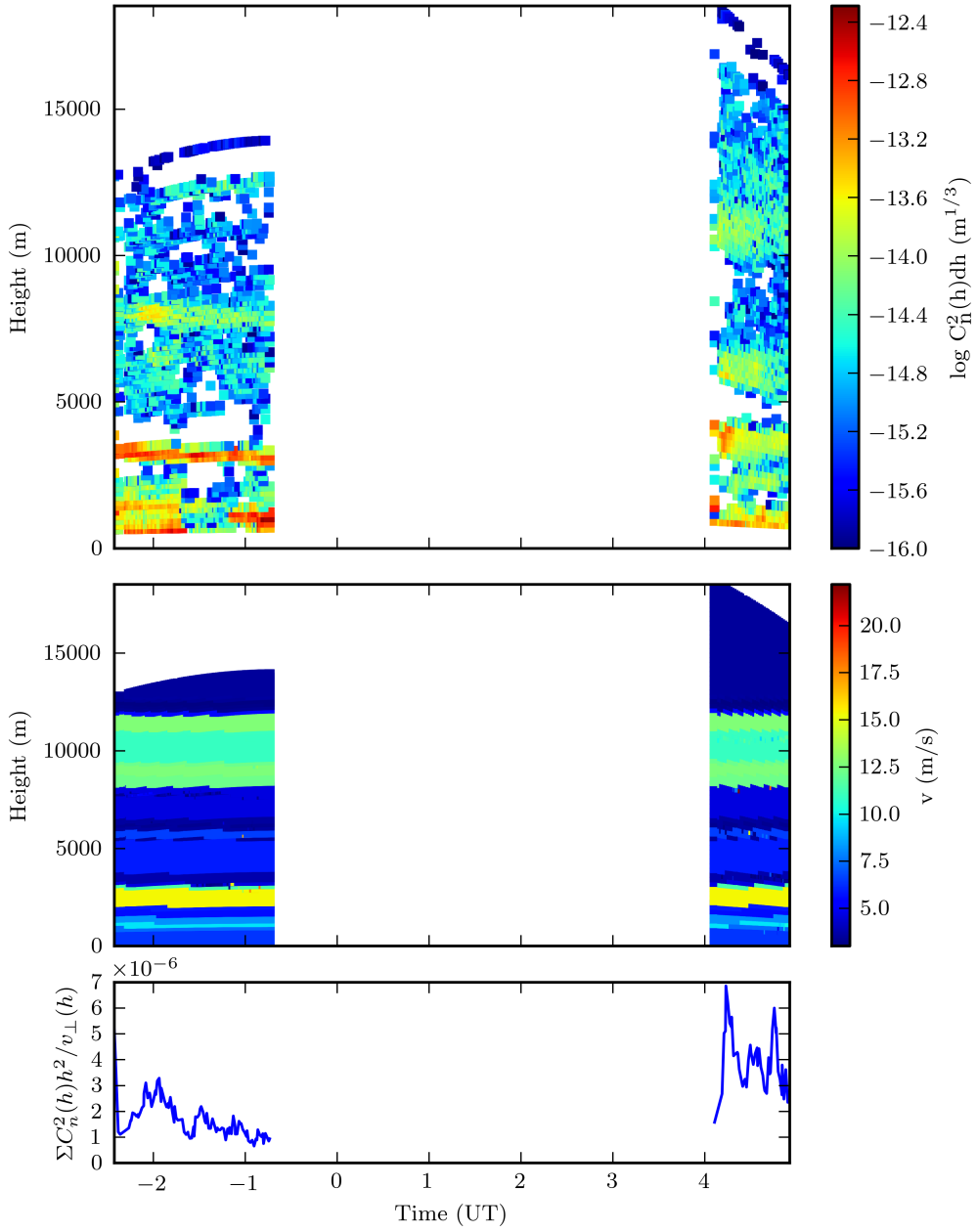

Figure 6.5: Atmospheric data for the night of 2013-07-20 obtained using SCIDAR on the 1.0m Jacobus Kapteyn Telescope. The top panel shows the measured C_n^2 profile with height. Data points with C_n^2 weaker than $10^{-16}\mathrm{m}^{2/3}$ have been removed for clarity. The middle panel shows the determined average wind velocity for the layers for each night. The bottom panel shows the calculated sum of $C_n^2(h)h^2/V_\perp$ from the information in the top two panels.

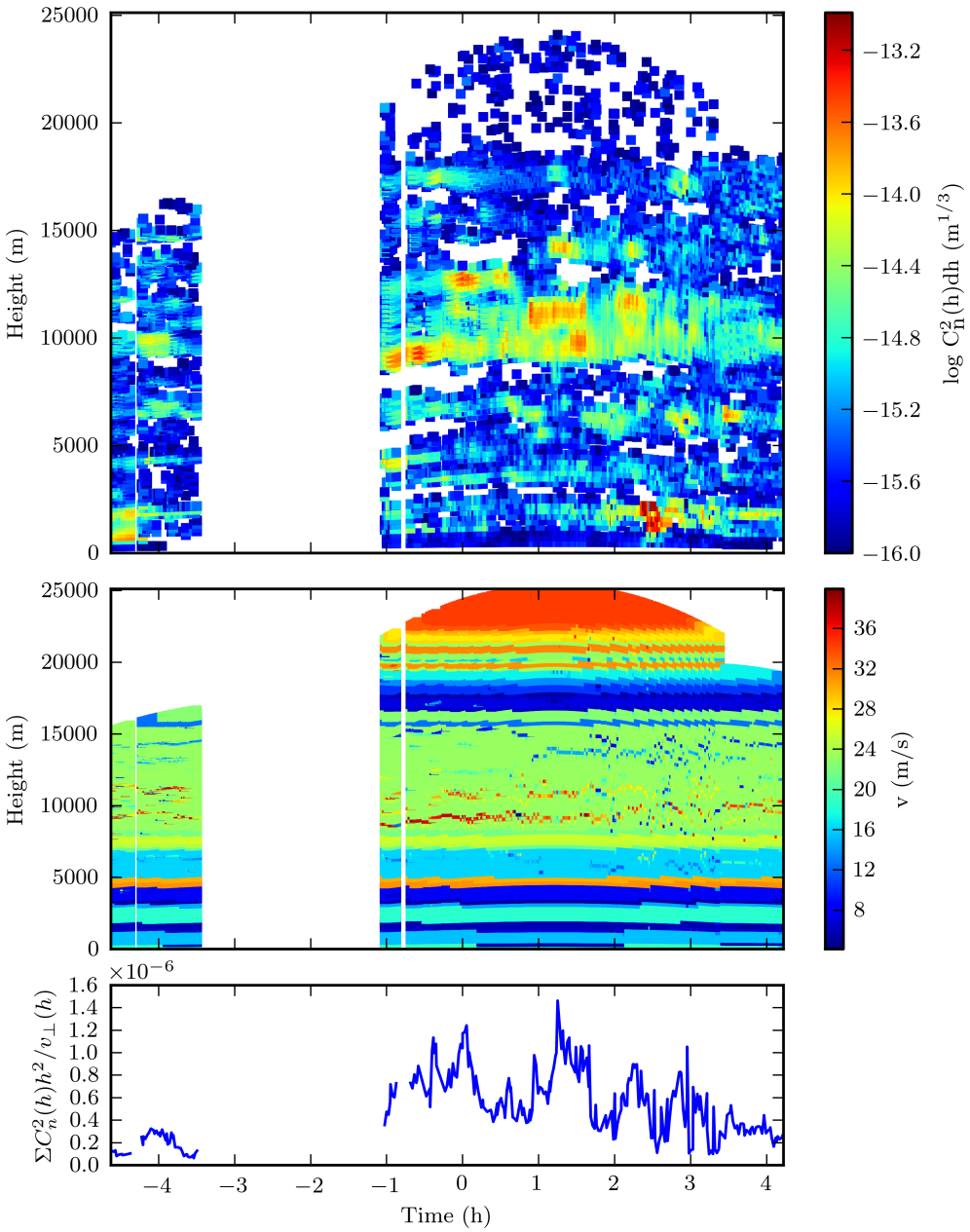

Figure 6.6: Atmospheric data for the night of 2014-03-15 obtained using SCIDAR on the 2.5m Isaac Newton Telescope. The top panel shows the measured C_n^2 profile with height. Data points with C_n^2 weaker than $10^-16\mathrm{m}^{1/3}$ have been removed for clarity. The middle panel shows the determined average wind velocity for the layers for each night. The bottom panel shows the calculated sum of $C_n^2(h)h^2/V_\perp$ from the information in the top two panels.

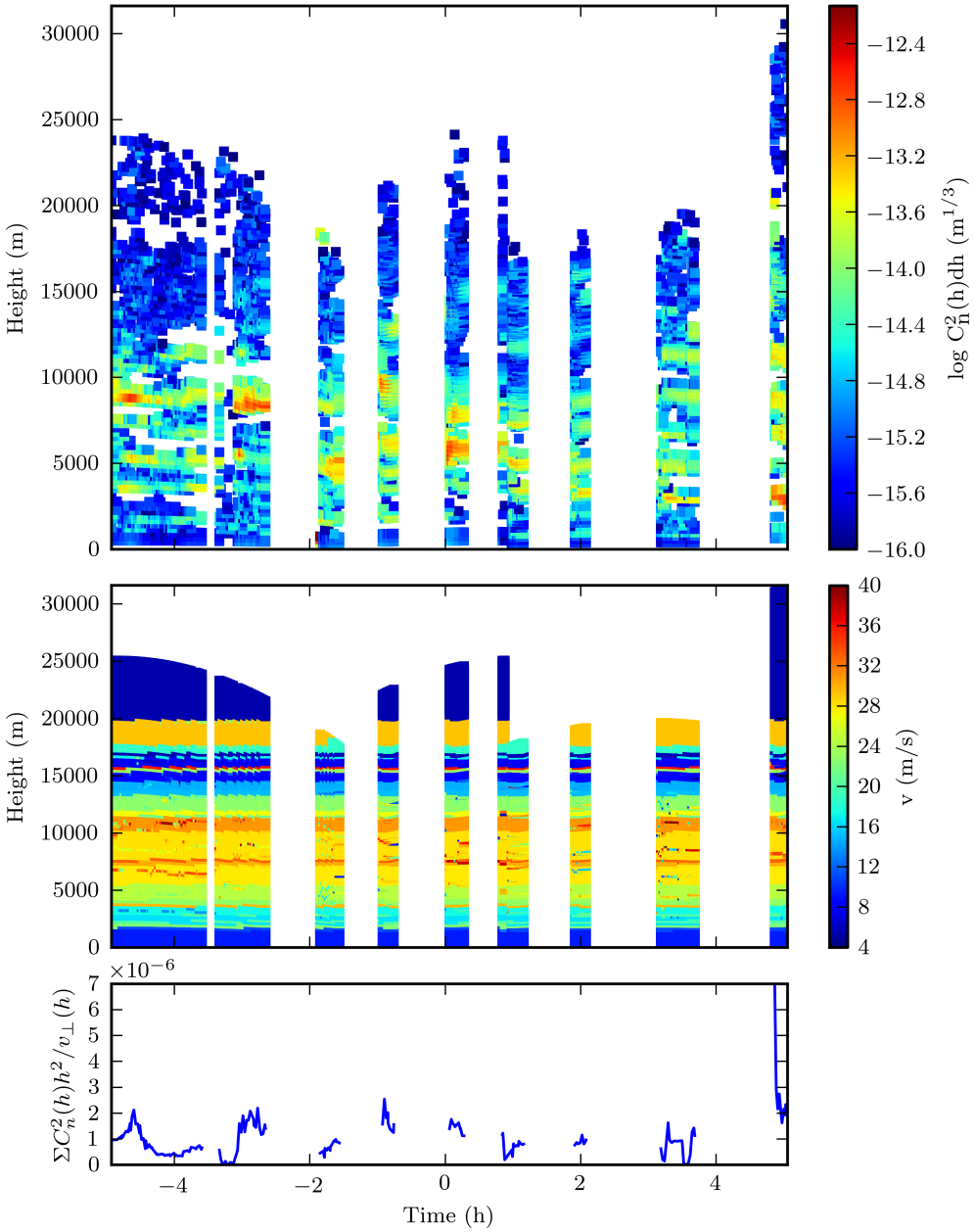

Figure 6.7: Atmospheric data for the night of 2014-03-16 obtained using SCIDAR on the 2.5m Isaac Newton Telescope. The top panel shows the measured C_n^2 profile with height. Data points with C_n^2 weaker than $10^-16\mathrm{m}^{1/3}$ have been removed for clarity. The middle panel shows the determined average wind velocity for the layers for each night. The bottom panel shows the calculated sum of $C_n^2(h)h^2/V_\perp$ from the information in the top two panels.

rected for, the presence of the transit produces a systematic offset in the standard deviations.

The total measured photometric noise, σ_m is calculated by measuring the normalised standard deviation of the differential counts in a running interval of 300s.

6.7 Results

In this section we show the comparison between σ_I obtained from the differential photometry of ULTRACAM and pt5m data and the noise estimate from SCIDAR. Coordinates and magnitudes of targets were obtained from SIMBAD[2].

2013-07-20

ULTRACAM photometry on the night of 2013-07-20 consists of two fields at the beginning and end of the night. The first contains two comparison stars around the field of HAT-P-23 at coordinates RA 20:24:29.72 +16:45:43.8, TYC 1632-1319-1 and TYC 1632-1019-1, with V magnitudes of 11.4 and 12.3 respectively. These stars were chosen as they produced the most stable differential flux (lowest ratio of σ/μ) within the observed field. The second set are faint $\sim$ 13 Vmag stars the field around the target V* OR And at coordinates RA 23:04:45.76 DEC +49:26:24.8 and RA 23:05:18.67 DEC +49:27:10.3. Both runs were taken with exposure times of 0.5s. Figure 6.8 shows the results obtained for the r band photometry.

The figure shows that the measured normalised standard deviation of the differential flux (red line) is higher than the system noise (yellow line), which has no knowledge of scintillation. The difference is due to scintillation, and is well predicted by turbulence profiling using SCIDAR. The difference between the measured noise and the system noise is greater for the first targets, as they are brighter and so more of the noise will be caused by scintillation. The step in the system noise (yellow line) is caused by the change of target. The data becomes noisy at the end due to twilight, which is reflected in the sharp rise in the measured system noise. The overestimation of scintillation by SCIDAR at the beginning of the night is caused

[2]SIMBAD Centre de donnes astronomiques de Strasbourg. http://simbad.u-strasbg.fr/simbad/

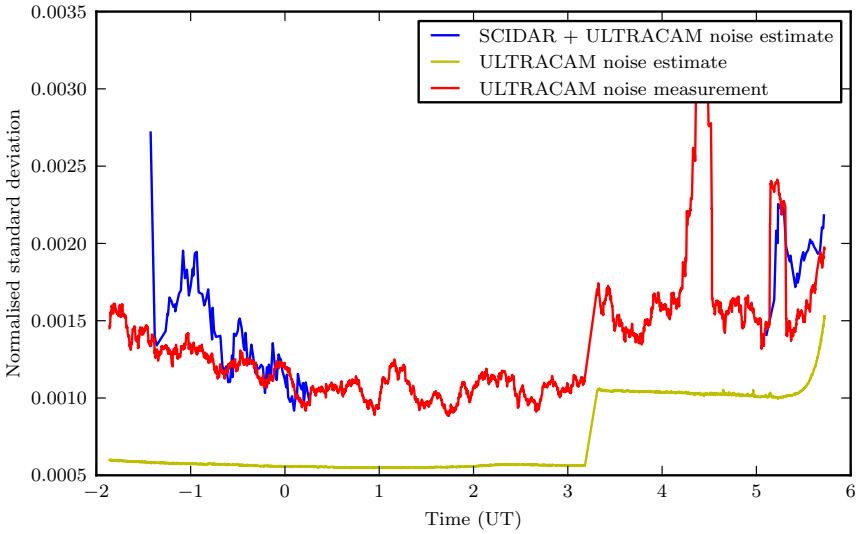

Figure 6.8: Comparison between predicted and measured scintillation from ULTRACAM on 2013-07-20. The red is line shows the normalised standard deviation of the measured flux from ULTRACAM. The prediction from SCIDAR (blue) takes into account scintillation, which is scaled according exposure time, telescope diameter and airmass of the observation, and the predicted noise from ULTRACAM. The predicted ULTRACAM noise includes photon noise and the small amount of system noise in ULTRACAM, shown in yellow.

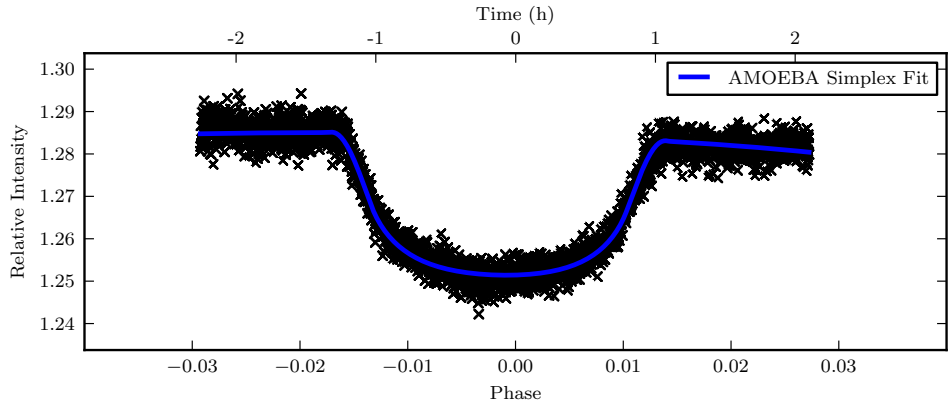

Figure 6.9: Light curve and fit of the transit of HAT-P-12b in the r' band on the night of 2014-03-15 using ULTRACAM on the 4.2m WHT.

by the low elevation of the target (45°).

2014-03-15

On the night of 2014-03-15, we examined the transit of HAT-P-12b. Throughout the night the seeing was stable, around 1-1.5". SCIDAR measurements at the INT show that the turbulence is close to the ground, so there is only very little scintillation. The target and comparison were HAT-P-12, a 12.8 Vmag star and a nearby star at RA 13:57:24.96 DEC+43:31:33.4 of similar brightness. The exposure time was 0.5s. Figure 6.9 shows the transit light curve fitted to the data obtained for the transit in the r' band.

Figure 6.10 and shows the analysis of the photometry of the light curve. The measured scintillation is the same order of magnitude as the prediction of SCIDAR and appears correlated. The discrepancy between SCIDAR and ULTRACAM noise is caused by both telescopes pointing in different directions. The fractional contribution from scintillation is low, due to the combination of weak turbulence and relative faintness of the targets, the data is shot noise dominated, with scintillation noise around 20%.

2014-03-16

On the night of 2014-03-16, we observed the transit of HAT-P-44b using ULTRACAM and the out-of-transit system WASP-54 using the $pt5m$ telescope. The light

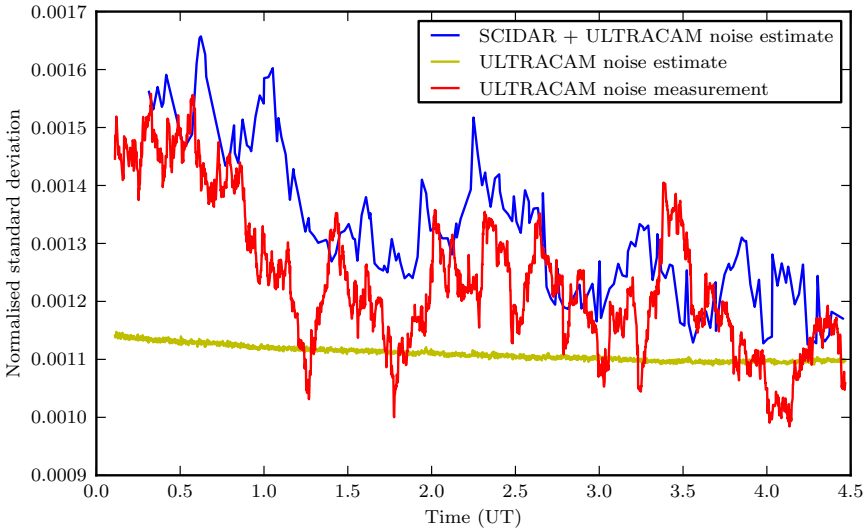

Figure 6.10: Comparison between predicted and measured scintillation from ULTRACAM on 2014-03-15. The red is line shows the normalised standard deviation of the measured flux from ULTRACAM. The prediction from SCIDAR (blue) takes into account scintillation, which is scaled according exposure time, telescope diameter and airmass of the observation, and the predicted noise from ULTRACAM. The predicted ULTRACAM noise includes photon noise and the small amount of system noise in ULTRACAM, shown in yellow.

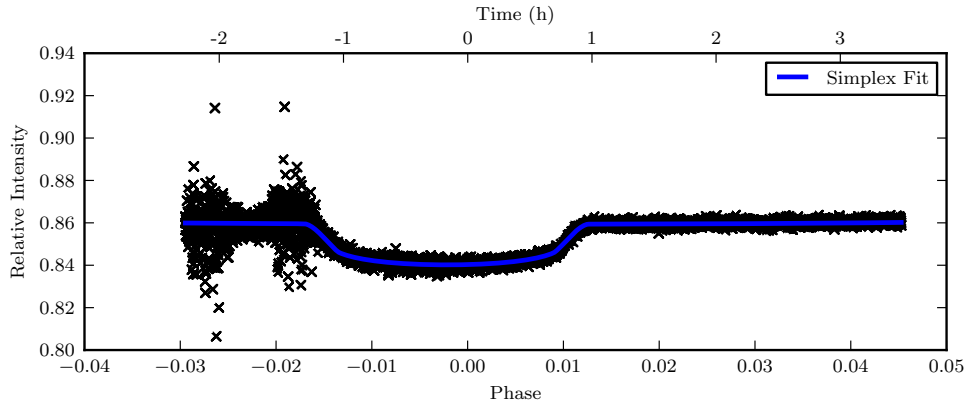

Figure 6.11: Light curve and fit of the transit of HAT-P-44b in the r' band on the night of 2014-03-16 using ULTRACAM on the 4.2m WHT.

curve from ULTRACAM was constructed from the 13.2 Vmag star GSC 03465-00123 and a nearby star of similar brightness at RA 14:12:42.10 DEC +47:01:05.0. Some thin clouds appear around 22:30 UT near the start of the transit, but clear up soon after. Figure 6.11 shows the light curve and fit obtained. From the light curve fitted data (figure 6.12), it can be seen that the scatter on the data improves as the night progresses. This is reflected in figure 6.13, which shows a plot of the normalised standard deviation of the light curve in the r' band. The high spikes in the yellow line are caused by the transparency variations creating large errors in the photometry, which is reflected in the measured variance shown in the red line. Anomalous measurements occur at 3 UT of 2014-03-16 where SCIDAR measures spikes. This is caused by a strong turbulent layer appearing in the SCIDAR profiles, but not in the ULTRACAM data, due to the different direction of pointing of the telescopes.

We compare the noise on the light curve for the g' band in figure 6.14. Recall from Chapter 2 that scintillation is independent of wavelength for large telescope diameters ($D >> r_F$). We observe a trend similar to the r' band in the g'. The curve on the yellow line is caused by the variable effects of extinction as the airmass changes.

The light curve from the $pt5m$ was created from the bright, 11.01 Vmag target, BD+00 3088, and nearby comparison HD 119217 observed on the night of 2014-03-16, simultaneously with the ULTRACAM measurement. Figure 6.11 shows the time-series photometry obtained. The comparison between the observed and predicted

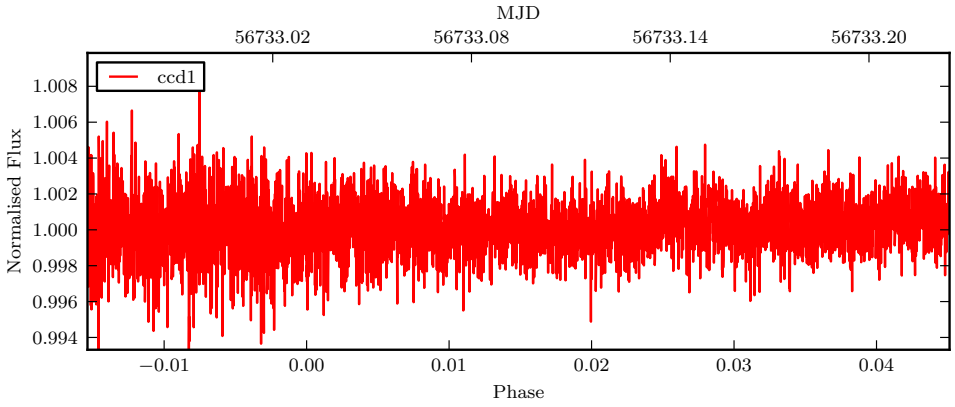

Figure 6.12: Differential photometry of HAT-P-44b with the transit fitted and divided out. The region of the transparency variations has is not included in this plot, to emphasise the improvement in the scatter of the data with time caused by scintillation.

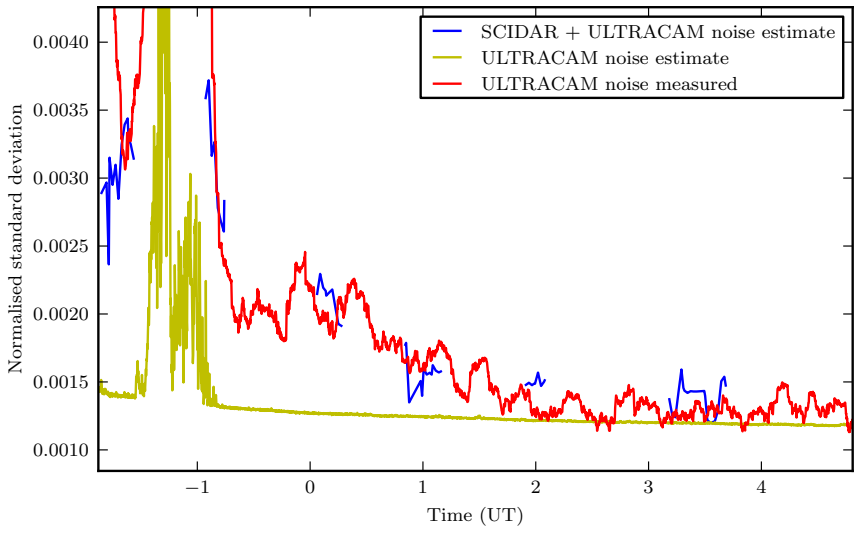

Figure 6.13: Comparison between predicted and measured scintillation from ULTRACAM on 2014-03-16 in the r' band. The red is line shows the normalised standard deviation of the measured flux from ULTRACAM. The prediction from SCIDAR (blue) takes into account scintillation, which is scaled according exposure time, telescope diameter and airmass of the observation, and the predicted noise from ULTRACAM. The predicted ULTRACAM noise includes photon noise and the small amount of system noise in ULTRACAM, shown in yellow.

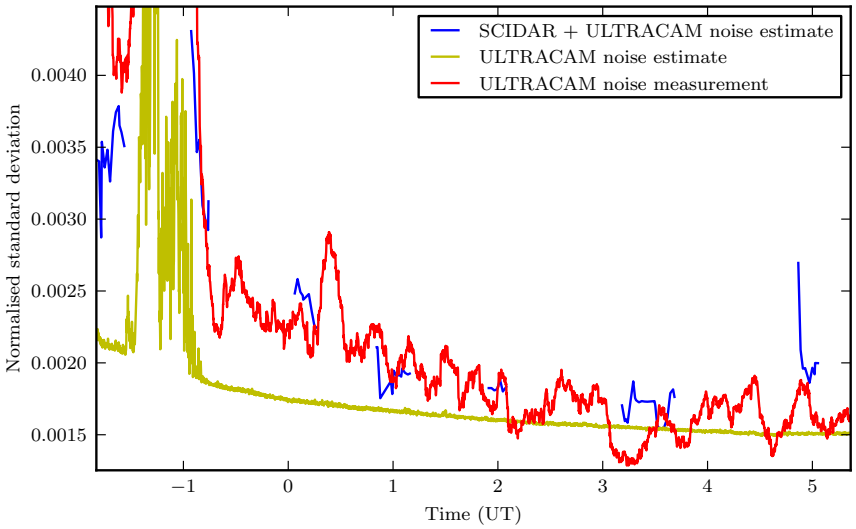

Figure 6.14: Comparison between predicted and measured scintillation from ULTRACAM on 2014-03-16 in the g' band. The red is line shows the normalised standard deviation of the measured flux from ULTRACAM. The prediction from SCIDAR (blue) takes into account scintillation, which is scaled according exposure time, telescope diameter and airmass of the observation, and the predicted noise from ULTRACAM. The predicted ULTRACAM noise includes photon noise and the small amount of system noise in ULTRACAM, shown in yellow.

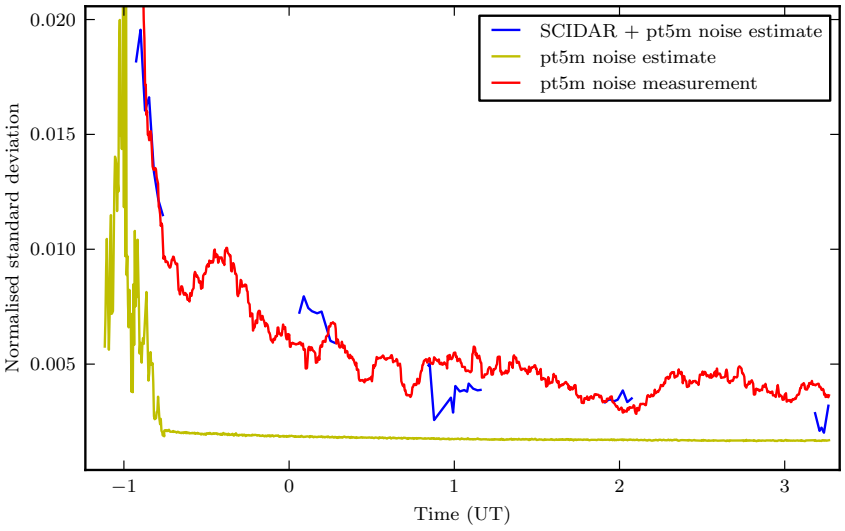

Figure 6.15: Comparison between predicted and measured scintillation from *pt5m* on 2014-03-16. The red is line shows the normalised standard deviation of the measured flux from pt5m. The prediction from SCIDAR (blue) takes into account scintillation, which is scaled according exposure time, telescope diameter and airmass of the observation, and the predicted noise from *pt5m* in the V band. The predicted *pt5m* noise includes photon noise and the small amount of system noise in *pt5m*, shown in yellow.

standard deviation is shown in figure 6.15. From here we can see that the predicted noise matches the measured noise on the light curve well. On both light curves, the same improvement with time is observed.

6.8 Discussion and Conclusion

We obtained 3 nights of turbulence profiling with SCIDAR simultaneously with observations using ULTRACAM and the *pt5m* on La Palma between 2013-07-20 and 2014-03-16. We predicted the scintillation index from the measured contemporaneous turbulence profile of the atmosphere for the telescope size and exposure time used. The total noise was calculated by combining the scintillation noise and the photon noise on the targets obtained from the aperture photometry. We found that the estimates of SCIDAR and measurements from photometry were correlated, and

in a mostly good agreement. Differences between the SCIDAR and turbulence profile measurements were caused by the different direction of pointing of the telescopes, being affected differently by wind velocities. The results show that turbulence profiling can be used to accurately predict the amount of scintillation noise present in photometric observation.

Chapter 7

The Secondary Eclipse of WASP-12b

In this chapter we present *z'*-band secondary eclipse photometry of the highly irradiated hot Jupiter WASP-12b using ULTRACAM on the 4.2m William Herschel Telescope. The results from this chapter have been published in Föhring et al. [47]. The observation, reduction, eclipse modelling and error estimation have been carried out by the author. The section on the comparison with atmospheric models has been written by Nikku Madhusudhan. We measure a decrease in flux of $\delta = 0.130 \pm 0.013\%$ during the passage of the planet behind the star, which is significantly deeper than the previous measurement at this wavelength ($0.082 \pm 0.015\%$, López-Morales et al. [84]). Our secondary eclipse is best fit with a mid-eclipse phase, ϕ, that is compatible with a circular orbit $\phi = 0.501 \pm 0.002$, in agreement with previous results [32]. In combination with existing data, our eclipse depth measurement allows us to constrain the characteristics of the planet's atmosphere, which is consistent with a carbon-rich model, with no evidence for a strong thermal inversion. If the difference in eclipse depth reported here compared to that of López-Morales et al. [84] is of physical origin, as opposed to due to systematics, it may be caused by temporal variability in the flux, due to atmospheric dynamics.

7.1 Introduction

Observations of secondary eclipses provide a powerful means of obtaining information about exoplanetary systems. During a secondary eclipse, as the planet passes behind its host star, a decrease in flux directly corresponding to the planet's emission is observed. Photometric measurements of the secondary eclipse allow us to probe the planet's thermal structure [36], atmospheric composition [37] and constrain the orbital eccentricity [23], all of which are key in assessing the planet's albedo, energy budget and tidal history. To date, ground-based observations have proved to be invaluable in aiding the atmospheric characterisation of transiting hot Jupiters (e.g. Sing and López-Morales [127]; de Mooij and Snellen [35]; Croll et al. [32]; Zhao et al. [144]).

The transiting exoplanet WASP-12b is a large (1.79 R_J) hot Jupiter on a close (0.0229 AU, 1.09 day) orbit around a 6300 K host star [58]. It is one of the largest and most intensely irradiated planets currently known, with an equilibrium temperature of $T_{eq} = 2516$ K. The combination of a relatively bright (1.35 $M_\odot$, G0V) host star and a large close-in planet with an orientation which enables the viewing of both primary and secondary events make WASP-12b an ideal system for ground-based follow-up observations.

The overinflated radius of WASP-12b poses a challenge for standard planetary models, which predict an upper limit of 1.2 R_J for evolved gas giants [10]. Proposed mechanisms for inflation include tidal heating [67], Ohmic dissipation (e.g. Perna et al. [106]; Batygin and Stevenson [5]; Huang and Cumming [65]), or strong irradiation (e.g. Enoch et al. [46]). Previous studies of WASP-12b have suggested intense tidal forces, giving it a prolate shape and causing it to lose mass to its host star through tidal stripping [78]. There is also evidence for the presence of a bow shock around the planetary magnetosphere directly in front of the planet [81]. Previous spectroscopic studies have found that the atmosphere of WASP-12b is lacking a strong thermal inversion and possesses very efficient day-night energy circulation, as well as an extreme overabundance of carbon, both of which are contrary to previous theoretical predictions [86], although this has been recently questioned by newer photometric data [33].

Theory predicts that the timescale for circularization of WASP-12b is very short. Initial radial velocity and eclipse measurements have suggested an eccentric orbit [58; 84], but this was later refuted Croll et al. [32]; Campo et al. [18]; Husnoo et al. [66]. An eccentric orbit would indicate orbital pumping from one or more undetected planets, or a very low tidal dissipation [78].

Previous observations of emission from the dayside atmosphere of WASP-12b have been reported using the Spitzer Space Telescope, at 3.6 μm, 4.5 μm, 5.8 μm and 8 μm [18], and from ground-based observations in the *J*, *H*, *Ks* [32; 144] and *z'* bands [84].

In this paper, we present a new, high-precision detection of the *z'* (9097Å) emission from the extrasolar planet WASP-12b, and discuss the implications on our understanding of the planet. In section 7.2 we describe our observations and data reduction. In section 7.3 we detail our light curve modelling and eclipse detection. In section 7.4 we show our method of error estimation, and in section 7.5, we compare the emission of the planet to atmospheric models. Finally, we discuss our results and provide conclusions in sections 7.6 and 7.7.

7.2 Observations and Data Reduction

The secondary eclipse of WASP-12b was observed on 2010 January 5 - 6 at the 4.2m William Herschel Telescope on La Palma using ULTRACAM [40]. A total of 3592 observations were made in the SDSS *u'*, *g'*, and *z'* filters between 22:54 UT and 05:30 UT during excellent transparency conditions. We obtained 3.05 hours of out-of-eclipse data and 2.70 hours of in-eclipse data at airmasses between 1.000 - 2.319. The telescope was defocussed to give a stellar FWHM of ∼5", enabling longer integration times without saturation, and reducing the effects of pixel sensitivity variations across the stellar profile (see Southworth et al. 128). An exposure time of 5.6s was used throughout the run, with a dead time between each exposure of 25ms. Each frame was timestamped to sub-millisecond accuracy using a dedicated GPS system [40].

The data were corrected for bias and flat-field using the ULTRACAM pipeline

software[1]. The effect of correcting the fringing that was apparent in the *z'* filter was investigated in detail using a fringe-frame constructed from night-sky frames; it was found that this correction did not produce a marked difference in the light curves and so was not employed in the final reduction.

We performed aperture photometry on the target and the brightest 9 comparison stars in the 5' ×5' field using aperture sizes of radii 15 - 50 pixels (4.5' - 15'). The best aperture was the one that produced the most stable photometry with the lowest variance in segments of the out-of-eclipse and mid-eclipse regions of the resulting light curve, and was found using a golden section search [70]. For our data this resulted in an aperture of 42 pixels. The centres of each star were determined by fitting a Moffat profile [94] to the PSF of each star. We decided to add an extra aperture on our target to include a background star, ∼10" from WASP-12 and partially overlapping our optimum aperture, as this improved the variance. The implications of this are discussed in section 7.4. We found that the size of the sky annulus did not have a significant effect on the photometry, and kept it constant with an inner radius of 60 pixels and outer radius of 90 pixels. The sky background level was determined using a clipped mean method, with fainter background stars masked out from the sky annuli.

We produced a single light curve by combining individual differential light curves that were produced from the three brightest comparison stars in the field, which had similar flux levels to the target in the *z'* band. The individual light curves were weighted based on the inverse chi-square of a straight-line fit to their out-of-eclipse and mid-eclipse sections. The scatter per point on this final light curve was measured as 0.14 mmag, or 0.013%.

In our data, the total drift in the pointing of WASP-12 on the CCDs was 14 pixels in x and 24 pixels in y. We tested our data for systematic correlations with x and y positions of the target on the detector, seeing, sky brightness variations and telescope parallactic angle. This was done by fitting linear correlations between each parameter and the out-of-eclipse portions of the light curve. We did not find any correlations. We discarded the latter 1.36 hours of the out-of-eclipse data precisely

[1]http://deneb.astro.warwick.ac.uk/phsaap/software/ultracam/html/index.html

at the onset of sudden transparency variations, as they caused the scatter per point to increase by up to a factor of 100. This left a total of 2740 observations between 22:54 UT and 04:08 UT, covering phases 0.426 and 0.594 based on the ephemeris of Hebb et al. [58], and air masses between 1.000 - 1.477.

7.3 Eclipse modelling

To establish the presence of an eclipse we modelled the light curve using the technique outlined by Sackett [121] without limb darkening. The input parameters of the model include the radii of the star and planet, the semi-major axis, the orbital inclination and the ephemeris, as given by Hebb et al. [58]. We also attempted to use the system parameters determined by Chan et al. [20], but found that the duration of the eclipse matches that found by Hebb et al. [58] more closely and yields a lower chi-squared fit.

The best-fit model was found by using a downhill simplex χ^2 minimisation routine [110], with the eclipse depth, δ, the phase of mid-eclipse, ϕ, and two background terms, c_1 and c_2, as free parameters. The two background terms allow the out-of-eclipse differential flux, B, to be fitted by an equation of the form: $B = c_1 + c_2 X$, where X is the airmass. The best-fit model, shown in Figure 7.1, is an eclipse with a depth of $\delta = 0.130\%$, centered at an orbital phase $\phi = 0.501$. The reduced χ^2 of the fit is 1.083. We also searched for evidence of a secondary eclipse in the g' and u' bands and found our results consistent with no detection in either.

We performed two tests to confirm the eclipse detection, in a manner similar to previously reported eclipse results (Deming et al. 36; Rogers et al. 119; López-Morales et al. 84). In the first test, we averaged all of the fully in-eclipse data points from the background-corrected light curve and repeated this for all of the out-of-eclipse points. The difference between the two measurements gives an eclipse depth of $0.135\% \pm 0.005\%$, where the error is calculated from the scatter on our in-eclipse and out-of-eclipse data points.

In the second test, we generated histograms of the in-eclipse and out-of-eclipse portions of the normalised light curve, and set the bin width equal to the measured

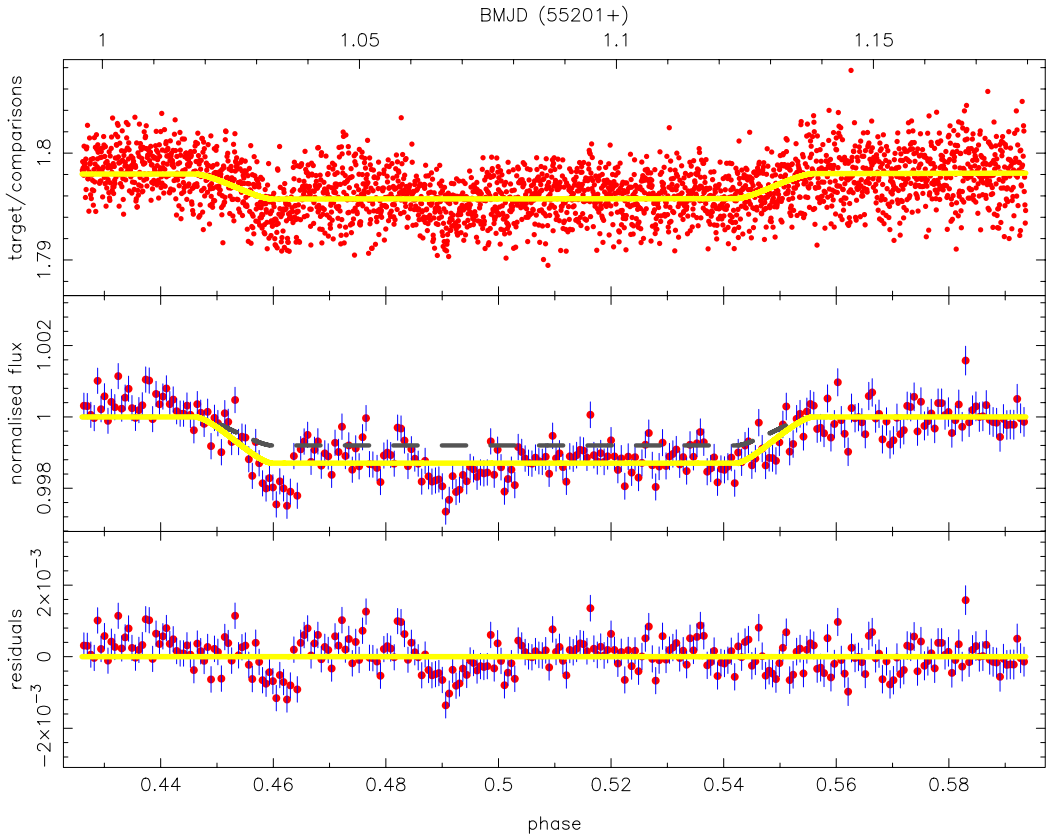

Figure 7.1: Secondary eclipse of WASP-12b observed in the *z'* band. The top panel shows the unbinned raw light curve, with the best-fit secondary eclipse model (including background) overplotted in yellow (see section 7.3). The middle panel shows the background subtracted and normalised light curve with the data binned into groups of 10 data points, corresponding to 1 minute, again with the best-fit model overplotted. The grey dashed line shows a depth of 0.082% as found by López-Morales et al. [84]. The bottom panel shows the residuals after subtraction of the best-fit model from the data shown in the middle panel.

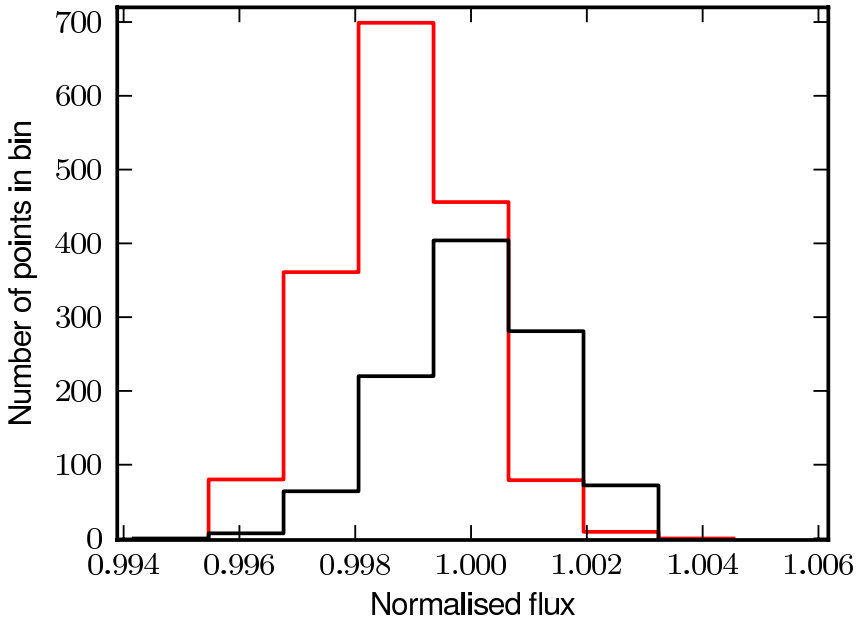

Figure 7.2: Histograms of the in-eclipse (red line) and out-of-eclipse portions of the normalised WASP-12b light curve. The width of each bin is 0.13%, the same as the eclipse depth.

eclipse depth. The result, shown in Figure 7.2, illustrates how the flux distribution of in-eclipse points is shifted by one bin, as expected, with respect to the out-of-eclipse flux distribution centred on 1.0.

7.4 Error Estimation

To compute the error in the eclipse depth and to determine the extent of systematics, we employ the binning technique described by Pont et al. [109]. Using this method, the uncertainty on the eclipse depth, $\sigma(N)$, is approximated as the error on the mean of the in-eclipse flux. In the absence of correlated noise, $\sigma(N) = \sigma_w/\sqrt{N}$, where N is the number of points in a given interval, here the eclipse, and σ_w is the measurement uncertainty, which can be obtained from the uncorrelated rms scatter per out-of-eclipse data points. When taking into account the covariance of the data on the timescales of the eclipse, the error on the eclipse depth can be shown to be well modelled by the relation $\sigma(N)^2 = \sigma_w^2/N + \sigma_r^2$, where σ_r is the systematic (red) noise component. The uncertainty $\sigma(N)$ can be estimated from the data by

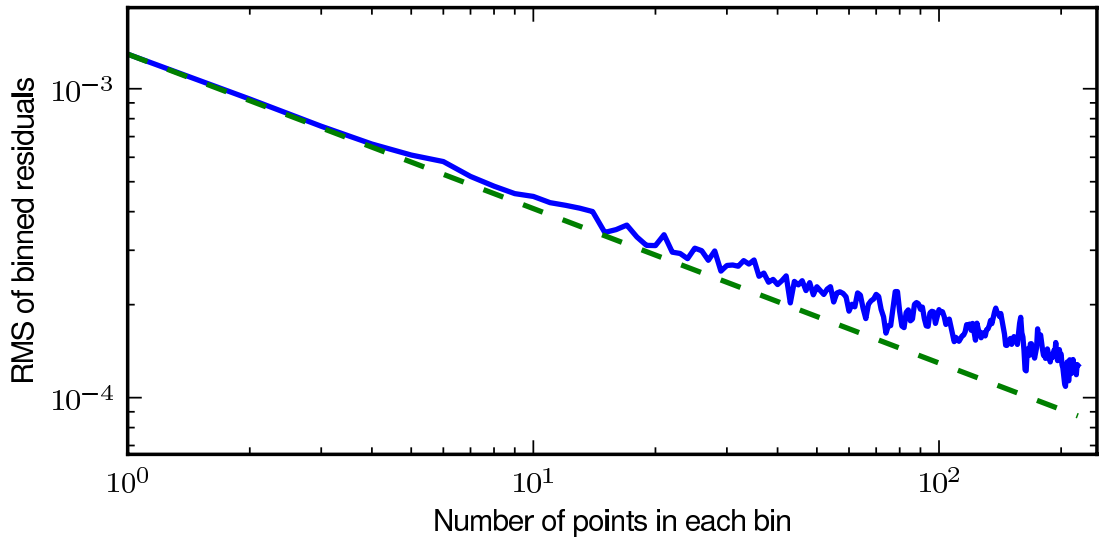

Figure 7.3: The root-mean-square scatter of our out-of-eclipse photometry (solid line), plotted as a function of the light curve binning factor. The dashed line displays the expectation for Gaussian noise.

binning the out-of-eclipse points in time in intervals of N points: the root mean square scatter of the binned residuals will follow an $N^{-1/2}$ relation in the absence of red noise; otherwise, they will be fit by $\sigma^2(N) = \sigma_w^2/N + \sigma_r^2$. Binning our data up to the timescales of the ingress and egress duration of 21 minutes (N = 220), we find $\sigma(220) \simeq \sigma_r = 0.013\%$.

We investigated the extent to which uncertainties in the system parameters affect our eclipse depth and mid-eclipse results. By varying the inclination, planet-to-star radius ratio, and semi-major axis of the system by 1σ from the reported values in Hebb et al. [58], the measured eclipse depth changed by a maximum of 3.59% or 0.28σ, while the mid-eclipse phase changes by 0.0004%.

We calculated two independent values of the errors in the eclipse depth and the phase of mid eclipse using the prayer-bead [52] and bootstrapping [110] techniques in order to estimate the error on the mid-eclipse phase. These provided estimates of $\phi = 0.501 \pm 0.002$, $\delta = 0.130 \pm 0.002\%$ and $\phi = 0.5014 \pm 0.0004$, $\delta = 0.1298 \pm 0.0003\%$, respectively. Taking the final values for eclipse depth and mid eclipse phase from the downhill simplex results and the errors from the most conservative estimate out of the Pont et al. [109] method, prayer-bead and bootstrap yielded the final

result for the phase of mid eclipse and the eclipse depth as $\phi = 0.501 \pm 0.002$ and $\delta = 0.130 \pm 0.013\%$.

It is necessary to discuss the implication of including additional background stars in our aperture photometry, as discussed in section 7.2. In their paper, Crossfield et al. [33] calculate that including an unresolved M dwarf star with a 1" separation from WASP-12 (Bergfors et al. 6, 7) in the photometry aperture dilutes the measured eclipse depth by 3.97% in the *z'* band. Accounting for this star in our measurement results in an eclipse depth of 0.135%. A second faint background star was also included in our aperture, which we have determined from our in-focus images contributes an additional dilution of 0.9%. This gives a total corrected eclipse depth of of 0.136%, which is within our error of ±0.013%.

7.5 Comparison with Atmospheric Models

We used our *z'*-band planet-star flux contrast, together with previously published data, to constrain the atmospheric properties of WASP-12b. We modelled the dayside atmosphere of WASP-12b using the approach followed in Madhusudhan [87]. The model, first developed in Madhusudhan and Seager [85], considers 1-D line-by-line radiative transfer in a plane-parallel atmosphere, with constraints of local thermodynamic equilibrium, hydrostatic equilibrium, and global energy balance, and includes the major molecular and collision-induced opacity sources expected in hydrogen-rich atmospheres. The temperature profile and molecular abundances constitute 12 free parameters of the model; six parameters for the temperature profile and six for the molecular abundances of H_2O, CO, CH_4, CO_2, C_2H_2, and HCN. Given the data, we explored the space of temperature profiles and composition, both oxygen-rich and carbon-rich [87], using a Markov Chain Monte Carlo optimisation algorithm [86] to find model fits to data.

We assumed that all the *z'*-band flux arose from thermal emission, in accordance with López-Morales and Seager [83], who showed that reflected light emission contributes 10-20 times less than thermal emission for very hot Jupiters, such as WASP-12b. We fitted models of WASP-12b to our observed *z'*-band flux together

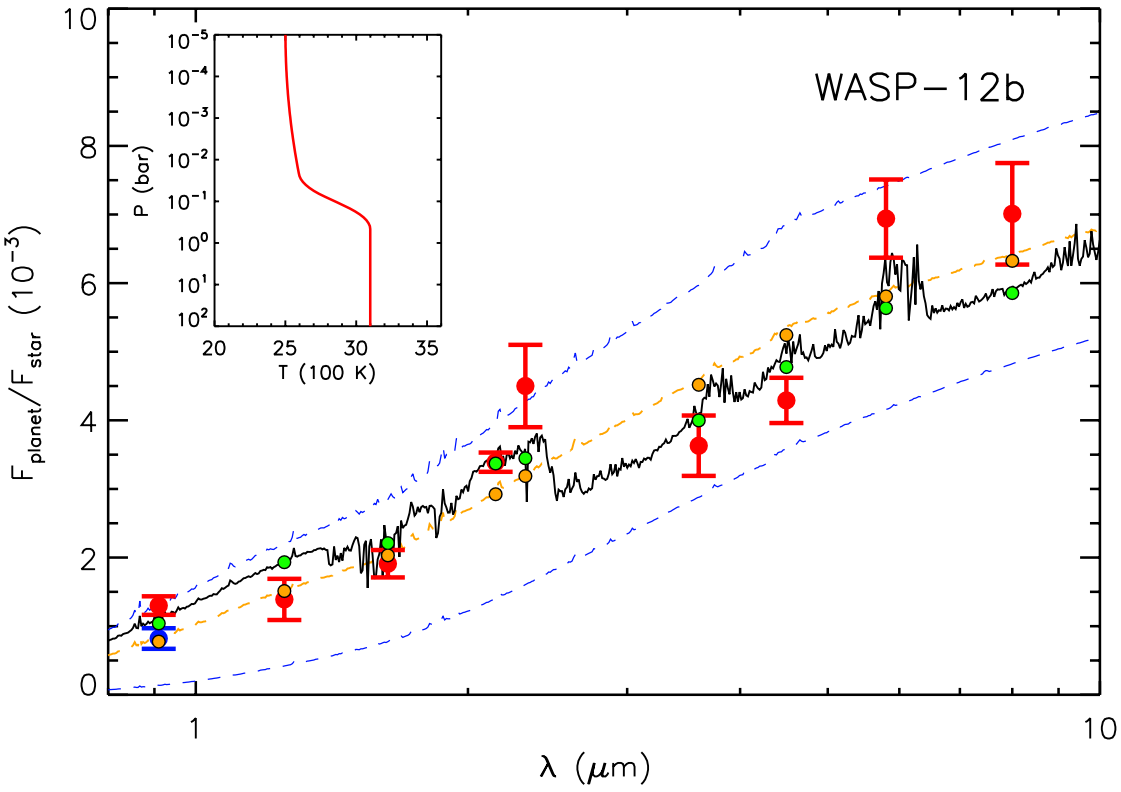

Figure 7.4: Observations and model secondary eclipse spectrum of WASP-12b. Our z'-band eclipse depth is shown as the red filled circle with error bars at 0.91 μm, together with previously published photometric observations at other wavelengths reported by Croll et al. [32], Campo et al. [18], Cowan et al. [30] and Crossfield et al. [33]. The blue circle with error bars beneath our data shows the previously published data in z' band by López-Morales et al. [84] (see Section 7.5). The black solid curve represents a best-fit model emission spectrum of the dayside atmosphere of WASP-12b with a carbon-rich composition and no thermal inversion. The orange dashed curve shows the best fitting blackbody model with a temperature of 3135K. The green circles without error bars represent the carbon-rich model integrated over the bandpasses of the data, while the orange circles are the integrated points for the blackbody model. The temperature profile is shown in the inset. The blue dashed curves are two blackbody spectra with temperatures of 2200K and 3200K shown for reference. The current data are best fit by a carbon-rich model without a strong thermal inversion, consistent with the findings of Madhusudhan et al. [86].

with existing photometric data in the J, H, and K bands [32], four-channels of *Spitzer* IRAC photometry [18; 30], and a narrow-band photometric observation at 2.3 μm [33]. For the two IRAC data points at 3.6 and 4.5 μm, we adopt the values from Cowan et al. [30], which have more conservative error bars. For the 4.5 μm point, for which two values have been reported by Cowan et al. [30], we choose the value that is consistent with the value reported by Campo et al. [18]. For all the previously published data, we use the revised values from Crossfield et al. [33] which have been corrected for the presence of a stellar companion. A model fit to all the data is shown in Figure 7.4. We found that a carbon-rich model (with C/O $\geq$ 1) and a weak thermal inversion in its dayside atmosphere provides the best fit to all the present data, in agreement with Madhusudhan et al. [86] and Madhusudhan [87]. The model spectrum shown in Figure 7.4, of an atmosphere that is carbon-rich and has no thermal inversion, provides a good fit to the data and has a χ^2 of 22.9. We also explored models with isothermal temperature profiles as suggested by Crossfield et al. [33], and found that the best fitting isothermal model (with one free parameter) has a temperature of 3135 K and a χ^2 of 48.8. To account for the different number of free parameters, we compared the models using the Bayesian Information Criterion [122], defined as BIC $=\chi^2 + N_{par} \times \ln(N_{dat})$, where N_{par} is the number of free parameters, and N_{dat} is the number of data. The BIC for the carbon-rich model was 49.3, lower than the value of 51.0 obtained for the isothermal model, indicating a better fit. An oxygen-rich model with or without a thermal inversion also provides a worse fit to the data compared to the carbon-rich model.An oxygen-rich model with or without a thermal inversion also provides a worse fit to the data compared to the carbon-rich model. Consequently, the present data favour the interpretation of a carbon-rich atmosphere with no thermal inversion in WASP-12b.

A more detailed atmospheric retrieval analysis and new data, which are beyond the scope of the current work, would be required to place tighter constraints on the C/O ratio of WASP-12b. In particular, we have used the *Spitzer* IRAC 3.6 and 4.5μm flux contrasts reported by Cowan et al. [30] and our present observation in the z' band. In doing so, a few other combinations of previous datasets at the same wavelengths have not been considered here. For example, considering the *Spitzer*

IRAC 3.6 and 4.5μm data from Campo et al. [18], which have lower uncertainties, would make the carbon-rich model more likely and the isothermal model even less likely. On the other hand, we have used only one of the two values for the IRAC 4.5μm point reported by Cowan et al. [30] that is consistent with the value of Campo et al. [18]. Considering the alternate point could improve the fit for the isothermal model. Yet other combinations result from using the previously reported *z'*-band flux of López-Morales et al. [84] instead of our current observation in the same band. We also note that a high-confidence narrow-band photometric observation at 2.3 μm might be able to provide a good constraint on the CO abundance. Future observations at this wavelength with more out-of-eclipse data than reported in Crossfield et al. [33] could provide a longer temporal baseline for a reliable estimate of the eclipse depth. We have also not used the thermal spectrum of WASP-12b obtained in the HST WFC3 bandpass (1.1 - 1. μm), reported by Swain et al. [129], as it has not yet been corrected for contamination due to the stellar companion [33]. A detailed atmospheric retrieval analysis of WASP-12b based on the various combinations of these existing, and possibly re-reduced and/or corrected, datasets will be pursued in a future study.

7.6 Discussion

Our observed eclipse depth, i.e. the planet-star flux ratio, in the *z'* band is 58% higher than that reported by López-Morales et al. [84]. This disagreement is at the 2.4-σ level and there are examples in the literature suggesting that this is not uncommon, e.g. the z'-band measurements of WASP-19b by Burton et al. [15] and Lendl et al. [77]. If this difference is of physical origin, as opposed to a systematic error, it may be evidence for temporal variability in the stellar or planetary flux. In principle, stellar variability may be caused due to stellar flares, as suggested in Haswell et al. [57], although this is unlikely given the spectral type of the host star. On the other hand, if the variability is in the emission from the planet it would imply temporal changes in the temperature distribution on the dayside hemisphere of WASP-12b at pressures close to the planetary photosphere in the *z'* band, typically

around 1 bar.

Assuming the stellar flux in the *z'* band is constant, our observation implies a 58% increase in the hemispherically-averaged dayside thermal emission from WASP-12b over that observed by López-Morales et al. [84]. Since the two observations were separated in time by 2 months, it may be possible that transient effects due to atmospheric dynamics might be causing the observed differences. Indeed, some general circulation models (GCMs) of hot Jupiters predict that large enough spatial structures, e.g. circumpolar vortices, in their atmospheres could cause temporal photometric variations in thermal emission from their dayside atmospheres (e.g. [114; 25]; but cf. [126]). Rauscher et al. [114] explored possible photometric variability in several hot Jupiters as a function of their mean zonal wind speeds and radiative forcing. For the example of the hot Jupiter HD 209458b, their models showed variations as high as 60-70% for wind speeds of 800 m/s. While a similar calculation has not been reported in the literature for WASP-12b, the order of magnitude higher incident irradiation received by WASP-12b compared to HD 209458b would imply higher wind speeds in WASP-12b and might cause the observed variability. GCM models of WASP-12b in the future would be able to investigate this possibility. Recent work by Fossati et al. [48] has shown that variability of a G-type star due to star spots would cause a magnitude variation of $\sim 0.2\%$. This amount is too low to explain our variable eclipse depth. Other work by Henry et al. [60] has found absorbing gas around WASP-12. A variable cloud of gas might cause some Rayleigh scattering, but that would be significant mainly in the visible, and not much in the red-optical where our *z'* band lies. The effect of a steady-state circumstellar disk or cloud of gas should cancel out when we subtract the in-eclipse and out-of-eclipse fluxes to obtain the eclipse depth.

We have also explored the possibility of local variations in the surface brightness of the dayside atmosphere of WASP-12b caused due to potential transient effects, e.g. "storms", following Agol et al. [1]. We considered a two-component *z'*-band brightness temperature distribution of the dayside hemisphere of the planet - a homogeneous background temperature (T_0) and a local perturbation with a temperature $T_1 = T_0 + \Delta T$ over a region with a parametric covering fraction (f), i.e. the

fraction of the surface area covered by the perturbation. Assuming nominal covering fractions of $f = 0.1 - 0.2$ ([126; 1]), we find that the difference between the two observed *z'*-band fluxes can be caused by temperature fluctuations of $\sim 450 - 750$ K or higher, relative to a background temperature of ~ 3000 K.

7.7 Conclusions

We have detected emission from WASP-12b in the *z'* band. We measure the eclipse depth at 0.91μm to be 0.130 ± 0.013 per cent, significantly deeper in comparison to previous data. Assuming this difference is not caused by systematics, and that the stellar flux is unchanging, given the early spectral type of the star, the observed discrepancy may be caused by a temporally variable photospheric temperature of the planet. Local thermal fluctuations in the surface brightness distribution of the planet caused by atmospheric dynamics may be able to explain the observed variability, which can be further constrained using general circulation models of WASP-12b in the future. Considering our *z'*-band observation along with previously reported photometric observations in other bandpasses, we find that the sum-total of data are best explained by a carbon-rich model, with no evidence for a strong thermal inversion, as has been previously reported. We also estimate the mid-eclipse phase of the planet to be 0.501 ± 0.002, which corresponds to a circular orbit.

Chapter 8

Conclusions

In future, children won't perceive the stars as mere twinkling points of light: they'll learn that each is a 'Sun', orbited by planets fully as interesting as those in our Solar system.

Martin Rees

This work has focussed on understanding and characterising the effect of the atmosphere for exoplanet photometry. The three main themes of this thesis have been: understanding scintillation through simulation, understanding scintillation through turbulence profiling and the exoplanet science that can be done using fast photometry.

In chapter 4 we investigated the effect of scintillation noise on ground-based transit photometry by simulation. We found that scintillation becomes the limiting source of noise for targets brighter than $V = 10.4$ for the average value of turbulence measured for a 0.5m telescope at La Palma. We compared simulations to analytical expressions of scintillation and found them to be in good agreement. We showed that by calculating scintillation index based on the average atmosphere model of Dravins et al. [44], the scintillation noise for La Palma is underestimated by a factor of 2 on average. The effect of scintillation on the astrophysical parameters for transit and secondary eclipses was examined in the visible and red-optical. We found that overall, the errors on the light curve arising from scintillation increase linearly the

scatter on the astrophysical parameters with a gradient in the range of 0.68 – 0.80.

In chapter 5 the effect of the noise due to aperture photometry was investigated for both instantaneous and short finite exposure times through simulation. It was found that for short finite exposure times speckle noise contributes to noise in photometry for aperture sizes of up to approximately 2.3×FWHM.

In chapter 6 we performed a comparison between estimates of scintillation obtained from turbulence profiling using SCIDAR with observations taken with ULTRACAM and the $pt5m$ telescope on La Palma between 2013-07-20 and 2014-03-16. We predicted the scintillation index from the measured contemporaneous turbulence profile of the atmosphere for the telescope size and exposure time used. The total noise was predicted by combining the scintillation noise and the photon noise on the targets obtained from the aperture photometry. We found that the estimates of SCIDAR and measurements from photometry were correlated, and in mostly good agreement. Differences between the SCIDAR and turbulence profile measurements were caused by the different direction of pointing of the telescopes, being affected differently by wind velocities. The results show that turbulence profiling can be used to accurately predict the amount of scintillation noise present in photometric observation.

Finally, in chapter 7 we presented the ground-based secondary eclipse of WASP-12b in the z' band using ULTRACAM. We measure the eclipse depth at 0.91μm to be 0.130 ± 0.013 per cent, significantly deeper in comparison to previous data. Assuming this difference is not caused by systematics, and that the stellar flux is unchanging, given the early spectral type of the star, the observed discrepancy may be caused by a temporally variable photospheric temperature of the planet. Local thermal fluctuations in the surface brightness distribution of the planet caused by atmospheric dynamics may be able to explain the observed variability, which can be further constrained using general circulation models of WASP-12b in the future. Considering our z'-band observation along with previously reported photometric observations in other bandpasses, we find that the sum-total of data are best explained by a carbon-rich model, with no evidence for a strong thermal inversion, as has been previously reported. We also estimate the mid-eclipse phase of the planet

to be 0.501 ± 0.002, which corresponds to a circular orbit.

8.1 Future Work

The work presented in this thesis opens up several avenues for future research, both in the direction of turbulence profiling and scintillation correction, as well as from astrophysical aspect.

8.1.1 Exoplanet Photometry

The results on the secondary eclipse of WASP-12b show that monitoring the variability of eclipses on longer timescales could reveal more about planetary atmospheric dynamics. Based on these published results, we have submitted a proposal for the WHT, to test the long-term variability of the secondary eclipse photometry of WASP-12b in the *z'*-band using ULTRACAM. This work can be expanded to monitor the long term variability of secondary eclipse photometry of other exoplanets to reveal weather patterns.

8.1.2 Scintillation Reduction

In the realms of turbulence profiling and scintillation reduction, there is still much to be done. We have shown that we can predict the total scintillation noise on observation using turbulence profiling, but this has opened many questions. It would be useful to obtain more simultaneous long time-series photometry and turbulence profiling to examine the ability of SCIDAR to predict scintillation noise in further detail. Effects such as flat fielding and correlated noise have not been examined, but our results suggest that the error budget is accounted for when including scintillation effects fully, although further observations would be needed. Simulation of scintillation can continue being a useful tool for investigating further effects in photometry, such as for the purpose of creating mock-images, which could also be used to investigate the errors arising from the reduction procedure in full detail and the effect of using different fitting algorithms. Accurately modelling the contribution of scintillation noise to the entire error budget for a given telescope and instrument

configuration is important in order to ascertain whether unaccounted noise on the observation is caused by systematics, or whether it originates from the atmosphere.

We will continue to investigate further avenues for improving precision on ground-based observations, such as the potential for using simultaneous observations in different wavelengths to correct for the achromatic component of scintillation. For example, using the *g'*-band of a multi-wavelength instrument to correct scintillation in the *z'*-band. Our preliminary tests on data from ULTRACAM show this to be a promising technique for reducing scintillation noise, however additional complications arising from systematic noise need to be addressed.

We have shown that using ULTRACAM, we are capable of obtaining a photometric precision of 0.1 milli-magnitudes (100 parts per million) for a 4.5h observation, which is currently the best precision obtainable from the ground. Space-based observatories, such as Kepler, are capable of obtaining a precision as good as 10 parts per million for a 10th magnitude star in the same cadence [26]. Future space-based missions are expected to provide precision of similar order of magnitude (Transiting Exoplanet Survey Satellite 90 ppm [76], PLATO 13 ppm [147], CHEOPS 10 ppm [14]). Providing an improvement in the observational precision of a factor of 2 using conjugate-plane photometry would enable the quality of ground-based observations to approach the precision attainable from space. While the usefulness of conjugate plane photometry for scintillation correction relies on the availability having two bright stars within $\sim 1'$ separation (the exact maximum separation depending on the ground layer), other techniques, such as tomographic atmospheric reconstruction [101] could provide a different means for reducing scintillation. Despite the effort needed to implement scintillation correction, such as the need for a dedicated instrument, an improvement of a factor of 1.5 on the astrophysical parameters at a fraction of a cost of a space-based instrument is worth the additional investment.

Bibliography

[1] Eric Agol, Nicolas B Cowan, Heather A Knutson, Drake Deming, Jason H Steffen, Gregory W Henry, and David Charbonneau. The climate of hd 189733b from fourteen transits and eclipses measured by spitzer. *ApJ* , 721(2):1861, 2010.

[2] R. Alonso, T. M. Brown, G. Torres, D. W. Latham, A. Sozzetti, G. Mandushev, J. A. Belmonte, D. Charbonneau, H. J. Deeg, E. W. Dunham, F. T. O'Donovan, and R. P. Stefanik. TrES-1: The Transiting Planet of a Bright K0 V Star. *ApJ* , 613:L153–L156, October 2004.

[3] R. Avila, L. J. Sánchez, F. Ibañez, J. Vernin, E. Masciadri, M. Azouit, A. Agabi, and S. Cuevas. Optical-Turbulence and Wind Profiles at San Pedro Mártir with G-SCIDAR. In *Revista Mexicana de Astronomia y Astrofisica Conference Series*, volume 31 of *Revista Mexicana de Astronomia y Astrofisica Conference Series*, pages 71–85, October 2007.

[4] A. Basden, T. Butterley, R. Myers, and R. Wilson. Durham extremely large telescope adaptive optics simulation platform. *Appl. Opt.* , 46:1089–1098, March 2007.

[5] K. Batygin and D. J. Stevenson. Inflating Hot Jupiters with Ohmic Dissipation. *ApJ* , 714:L238–L243, May 2010.

[6] C. Bergfors, W. Brandner, T. Henning, and S. Daemgen. Stellar companions to exoplanet host stars with Astralux. In A. Sozzetti, M. G. Lattanzi, and A. P. Boss, editors, *IAU Symposium*, volume 276 of *IAU Symposium*, pages 397–398, November 2011.

[7] C. Bergfors, W. Brandner, S. Daemgen, B. Biller, S. Hippler, M. Janson, N. Kudryavtseva, K. Geißler, T. Henning, and R. Köhler. Stellar companions to exoplanet host stars: Lucky Imaging of transiting planet hosts. *MNRAS* , 428:182–189, January 2013.

[8] M. S. Bessell. UBVRI photometry. II - The Cousins VRI system, its temperature and absolute flux calibration, and relevance for two-dimensional photometry. *PASP* , 91:589–607, October 1979.

[9] J. Binney and M. Merrifield. *Galactic Astronomy*. Princeton University Press, 1998.

[10] P. Bodenheimer, G. Laughlin, and D. N. C. Lin. On the Radii of Extrasolar Giant Planets. *ApJ* , 592:555–563, July 2003.

[11] G. D. Boreman and C. Dainty. Zernike expansions for non-Kolmogorov turbulence. In D. Malacara-Hernandez, S. E. Acosta, R. Rodriguez-Vera, Z. Malacara, and A. A. Morales, editors, *Second Iberoamerican Meeting on Optics*, volume 2730 of *Society of Photo-Optical Instrumentation Engineers (SPIE) Conference Series*, pages 192–199, February 1996.

[12] A. P. Boss. Proximity of Jupiter-Like Planets to Low-Mass Stars. *Science*, 267:360–362, January 1995.

[13] A. P. Boss. Giant planet formation by gravitational instability. *Science*, 276: 1836–1839, 1997.

[14] C. Broeg, A. Fortier, D. Ehrenreich, Y. Alibert, W. Baumjohann, W. Benz, M. Deleuil, M. Gillon, A. Ivanov, R. Liseau, M. Meyer, G. Oloffson, I. Pagano, G. Piotto, D. Pollacco, D. Queloz, R. Ragazzoni, E. Renotte, M. Steller, and N. Thomas. CHEOPS: A transit photometry mission for ESA's small mission programme. In *European Physical Journal Web of Conferences*, volume 47 of *European Physical Journal Web of Conferences*, April 2013.

[15] J. R. Burton, C. A. Watson, S. P. Littlefair, V. S. Dhillon, N. P. Gibson, T. R.

Marsh, and D. Pollacco. z'-band Ground-based Detection of the Secondary Eclipse of WASP-19b. *ApJS* , 201:36, August 2012.

[16] R. P. Butler, G. W. Marcy, D. A. Fischer, T. M. Brown, A. R. Contos, S. G. Korzennik, P. Nisenson, and R. W. Noyes. Evidence for Multiple Companions to Andromedae. *ApJ* , 526:916–927, December 1999.

[17] H. Campins, G. H. Rieke, and M. J. Lebofsky. Absolute calibration of photometry at 1 through 5 microns. *AJ* , 90:896–899, May 1985.

[18] C. J. Campo, J. Harrington, R. A. Hardy, K. B. Stevenson, S. Nymeyer, D. Ragozzine, N. B. Lust, D. R. Anderson, A. Collier-Cameron, J. Blecic, C. B. T. Britt, W. C. Bowman, P. J. Wheatley, T. J. Loredo, D. Deming, L. Hebb, C. Hellier, P. F. L. Maxted, D. Pollaco, and R. G. West. On the Orbit of Exoplanet WASP-12b. *ApJ* , 727:125, February 2011.

[19] J. A. Carter and J. N. Winn. Parameter Estimation from Time-series Data with Correlated Errors: A Wavelet-based Method and its Application to Transit Light Curves. *ApJ* , 704:51–67, October 2009.

[20] Tucker Chan, Mikael Ingemyr, Joshua N. Winn, Matthew J. Holman, Roberto Sanchis-Ojeda, Gil Esquerdo, and Mark Everett. The transit light-curve project. xiv. confirmation of anomalous radii for the exoplanets tres-4b, hat-p-3b, and wasp-12b. *AJ* , 141(6):179, 2011.

[21] D. Charbonneau. HD 209458 and the Power of the Dark Side. In *Scientific Frontiers in Research on Extrasolar Planets*, pages 449–456, 2003.

[22] D. Charbonneau, T. M. Brown, D. W. Latham, and M. Mayor. Detection of Planetary Transits Across a Sun-like Star. *The Astrophysical Journal Letters*, 529:L45–L48, January 2000.

[23] D. Charbonneau, L. E. Allen, S. T. Megeath, G. Torres, R. Alonso, T. M. Brown, R. L. Gilliland, D. W. Latham, G. Mandushev, F. T. O'Donovan, and A. Sozzetti. Detection of Thermal Emission from an Extrasolar Planet. *ApJ* , 626:523–529, June 2005.

[24] David Charbonneau, Timothy M. Brown, Robert W. Noyes, and Ronald L. Gilliland. Detection of an extrasolar planet atmosphere. *The Astrophysical Journal*, 568(1):377, 2002.

[25] James Y-K. Cho, Kristen Menou, Bradley M. S. Hansen, and Sara Seager. Atmospheric circulation of close-in extrasolar giant planets. i. global, barotropic, adiabatic simulations. *ApJ* , 675(1):817, 2008.

[26] J. L. Christiansen, J. M. Jenkins, D. A. Caldwell, C. J. Burke, P. Tenenbaum, S. Seader, S. E. Thompson, T. S. Barclay, B. D. Clarke, J. Li, J. C. Smith, M. C. Stumpe, J. D. Twicken, and J. Van Cleve. The Derivation, Properties, and Value of Kepler"s Combined Differential Photometric Precision. *PASP* , 124:1279–1287, December 2012.

[27] A. Claret. A new non-linear limb-darkening law for LTE stellar atmosphere models. Calculations for -5.0 = log[M/H] = +1, 2000 K = T_{eff} = 50000 K at several surface gravities. *A&A* , 363:1081–1190, November 2000.

[28] K. D. Colón and E. B. Ford. Benefits of Ground-Based Photometric Follow-Up for Transiting Extrasolar Planets Discovered with Kepler and CoRoT. *ApJ*, 703:1086–1095, September 2009.

[29] C. M. Copperwheat, P. J. Wheatley, J. Southworth, J. Bento, T. R. Marsh, V. S. Dhillon, J. J. Fortney, S. P. Littlefair, and R. Hickman. Transmission photometry of WASP-12b: simultaneous measurement of the planetary radius in three bands. *MNRAS* , 434:661–670, September 2013.

[30] Nicolas B. Cowan, Pavel Machalek, Bryce Croll, Louis M. Shekhtman, Adam Burrows, Drake Deming, Tom Greene, and Joseph L. Hora. Thermal phase variations of wasp-12b: Defying predictions. *ApJ* , 747(1):82, 2012.

[31] A. N. Cox. *Allen's astrophysical quantities*. Springer-Verlag, 2000.

[32] B. Croll, D. Lafreniere, L. Albert, R. Jayawardhana, J. J. Fortney, and N. Murray. Near-infrared Thermal Emission from WASP-12b: Detections of the Secondary Eclipse in Ks, H, and J. *AJ* , 141:30, February 2011.

[33] I. J. M. Crossfield, T. Barman, B. M. S. Hansen, I. Tanaka, and T. Kodama. Re-evaluating wasp-12b: Strong emission at 2.315m, deeper occultations, and an isothermal atmosphere. *ApJ* , 760(2):140, 2012.

[34] F. Dalaudier, A.S. Gurvich, V. Kan, and C. Sidi. Middle stratosphere temperature spectra observed with stellar scintillation and in situ techniques. *Advances in Space Research*, 14(9):61 – 64, 1994.

[35] E. J. W. de Mooij and I. A. G. Snellen. Ground-based K-band detection of thermal emission from the exoplanet TrES-3b. *A&A* , 493:L35–L38, January 2009.

[36] D. Deming, S. Seager, L. J. Richardson, and J. Harrington. Infrared radiation from an extrasolar planet. *Nature* , 434:740–743, March 2005.

[37] D. Deming, J. Harrington, S. Seager, and L. J. Richardson. Strong Infrared Emission from the Extrasolar Planet HD 189733b. *ApJ* , 644:560–564, June 2006.

[38] D. J. C. Dennis and T. B. Nickels. On the limitations of Taylor's hypothesis in constructing long structures in a turbulent boundary layer. *Journal of Fluid Mechanics*, 614:197, October 2008.

[39] V. Dhillon, T. Marsch, and Ultracam Team. ULTRACAM Successfully Commissioned on the WHT. *The Newsletter of the Isaac Newton Group of Telescopes*, 6:25–26, October 2002.

[40] V. S. Dhillon, T. R. Marsh, M. J. Stevenson, D. C. Atkinson, P. Kerry, P. T. Peacocke, A. J. A. Vick, S. M. Beard, D. J. Ives, D. W. Lunney, S. A. McLay, C. J. Tierney, J. Kelly, S. P. Littlefair, R. Nicholson, R. Pashley, E. T. Harlaftis, and K. O'Brien. ULTRACAM: an ultrafast, triple-beam CCD camera for high-speed astrophysics. *MNRAS* , 378:825–840, July 2007.

[41] P. Dierickx. IMAQ 0.7, Diffraction Analysis Software Package. *E.S.O.*, November 1988.

[42] D. Dravins, L. Lindegren, E. Mezey, and A. T. Young. Atmospheric Intensity Scintillation of Stars, I. Statistical Distributions and Temporal Properties. *PASP* , 109:173–207, February 1997.

[43] D. Dravins, L. Lindegren, E. Mezey, and A. T. Young. Atmospheric Intensity Scintillation of Stars. II. Dependence on Optical Wavelength. *PASP* , 109: 725–737, June 1997.

[44] D. Dravins, L. Lindegren, E. Mezey, and A. T. Young. Atmospheric Intensity Scintillation of Stars. III. Effects for Different Telescope Apertures. *PASP* , 110:610–633, May 1998.

[45] B. L. Ellerbroek. First-order performance evaluation of adaptive-optics systems for atmospheric-turbulence compensation in extended-field-of-view astronomical telescopes. *Journal of the Optical Society of America A*, 11:783–805, February 1994.

[46] B. Enoch, A. Collier Cameron, and K. Horne. Factors affecting the radii of close-in transiting exoplanets. *A&A* , 540:A99, April 2012.

[47] D. Föhring, V. S. Dhillon, Nikku Madhusudhan, T. R. Marsh, C. M. Copperwheat, S. P. Littlefair, and Richard W. Wilson. Ultracam z-band detection of the secondary eclipse of wasp-12b. *MNRAS* , 435(3):2268–2273, 2013.

[48] L. Fossati, T. R. Ayres, C. A. Haswell, D. Bohlender, O. Kochukhov, and L. Flöer. Absorbing Gas around the WASP-12 Planetary System. *ApJ* , 766: L20, April 2013.

[49] D. L. Fried. Statistics of a geometric representation of wavefront distortion. *J. Opt. Soc. Am.*, 55(11):1427–1431, 1965.

[50] A. Fuchs, M. Tallon, and J. Vernin. Focusing on a Turbulent Layer: Principle of the "Generalized SCIDAR". *PASP* , 110:86–91, January 1998.

[51] B. Scott Gaudi and Joshua N. Winn. Prospects for the characterization and confirmation of transiting exoplanets via the rossiter-mclaughlin effect. *The Astrophysical Journal*, 655(1):550, 2007.

[52] M. Gillon, B. Smalley, L. Hebb, D. R. Anderson, A. H. M. J. Triaud, C. Hellier, P. F. L. Maxted, D. Queloz, and D. M. Wilson. Improved parameters for the transiting hot Jupiters WASP-4b and WASP-5b. *A&A* , 496:259–267, March 2009.

[53] E. Golbraikh, H. Branover, N. S. Kopeika, and A. Zilberman. Non-Kolmogorov atmospheric turbulence and optical signal propagation. *Nonlinear Processes in Geophysics*, 13:297–301, July 2006.

[54] J. W. Goodman. *Introduction to Fourier optics*. Roberts & Co., 2005.

[55] M. E. Gracheva and A. S. Gurvich. Strong fluctuations in the intensity of light propagated through the atmosphere close to the earth. *Radiophysics and Quantum Electronics*, 8:511–515, July 1965.

[56] R. Griffin. On the possibility of determining stellar radial velocities to 0.01 km s^{-1}. *MNRAS* , 162:243–253, 1973.

[57] CA Haswell, L Fossati, T Ayres, K France, CS Froning, S Holmes, UC Kolb, R Busuttil, RA Street, L Hebb, et al. Near-ultraviolet absorption, chromospheric activity, and star-planet interactions in the wasp-12 system. *ApJ* , 760 (1):79, 2012.

[58] L. Hebb, A. Collier-Cameron, B. Loeillet, D. Pollacco, G. Hébrard, R. A. Street, F. Bouchy, H. C. Stempels, C. Moutou, E. Simpson, S. Udry, Y. C. Joshi, R. G. West, I. Skillen, D. M. Wilson, I. McDonald, N. P. Gibson, S. Aigrain, D. R. Anderson, C. R. Benn, D. J. Christian, B. Enoch, C. A. Haswell, C. Hellier, K. Horne, J. Irwin, T. A. Lister, P. Maxted, M. Mayor, A. J. Norton, N. Parley, F. Pont, D. Queloz, B. Smalley, and P. J. Wheatley. WASP-12b: The Hottest Transiting Extrasolar Planet Yet Discovered. *ApJ* , 693:1920–1928, March 2009.

[59] G. W. Henry, G. W. Marcy, R. P. Butler, and S. S. Vogt. A Transiting "51 Peg-like" Planet. *ApJ*, 529:L41–L44, January 2000.

[60] Gregory W Henry, Stephen R Kane, Sharon X Wang, Jason T Wright, Tabetha S Boyajian, Kaspar von Braun, David R Ciardi, Diana Dragomir, Chris Farrington, Debra A Fischer, et al. Host star properties and transit exclusion for the hd 38529 planetary system. *The Astrophysical Journal*, 768 (2):155, 2013.

[61] C. W. Higgins, M. Froidevaux, V. Simeonov, N. Vercauteren, C. Barry, and M. B. Parlange. The Effect of Scale on the Applicability of Taylor's Frozen Turbulence Hypothesis in the Atmospheric Boundary Layer. *Boundary-Layer Meteorology*, 143:379–391, May 2012.

[62] M. J. Holman and N. W. Murray. The Use of Transit Timing to Detect Terrestrial-Mass Extrasolar Planets. *Science*, 307:1288–1291, February 2005.

[63] M. J. Holman, J. N. Winn, D. W. Latham, F. T. O'Donovan, D. Charbonneau, G. A. Bakos, G. A. Esquerdo, C. Hergenrother, M. E. Everett, and A. Pál. The Transit Light Curve Project. I. Four Consecutive Transits of the Exoplanet XO-1b. *ApJ* , 652:1715–1723, December 2006.

[64] S. B. Howell. *Handbook of CCD Astronomy.* Cambridge University Press, April 2000.

[65] X. Huang and A. Cumming. Ohmic Dissipation in the Interiors of Hot Jupiters. *ApJ* , 757:47, September 2012.

[66] N. Husnoo, F. Pont, G. Hébrard, E. Simpson, T. Mazeh, F. Bouchy, C. Moutou, L. Arnold, I. Boisse, R. F. Díaz, A. Eggenberger, and A. Shporer. Orbital eccentricity of WASP-12 and WASP-14 from new radial velocity monitoring with SOPHIE. *MNRAS* , 413:2500–2508, June 2011.

[67] L. Ibgui, A. Burrows, and D. S. Spiegel. Tidal Heating Models for the Radii of the Inflated Transiting Giant Planets WASP-4b, WASP-6b, WASP-12b, WASP-15b, and TrES-4. *ApJ* , 713:751–763, April 2010.

[68] R. A. Johnston and R. G. Lane. Modeling Scintillation from an Aperiodic Kolmogorov Phase Screen. *Appl. Opt.* , 39:4761–4769, September 2000.

[69] S. Kenyon, J. Lawrence, M. C. B. Ashley, J. W. V. Storey, A. Tokovinin, and E. Fossat. Atmospheric scintillation at Dome C, Antarctica: implications for photometry and astrometry. *IAU Special Session*, 7, August 2006.

[70] J. Kiefer. Sequential minmax search for a maximum. *Proc. Am. Math. Soc.*, 4:502–506, 1935.

[71] David M. Kipping. Transit timing effects due to an exomoon. *Monthly Notices of the Royal Astronomical Society*, 392, January 2009.

[72] V. A. Klueckers, N. J. Wooder, T. W. Nicholls, M. J. Adcock, I. Munro, and J. C. Dainty. Profiling of atmospheric turbulence strength and velocity using a generalised SCIDAR technique. *A&AS* , 130:141–155, May 1998.

[73] A.N. Kolmogorov. Dissipation of energy in the locally isotropic turbulence. *Proceedings: Mathematical and Physical Sciences*, pages 15–17, 1941.

[74] A.N. Kolmogorov. The local structure of turbulence in incompressible viscous fluid for very large Reynolds numbers. *Proceedings: Mathematical and Physical Sciences*, pages 9–13, 1941.

[75] V. Kornilov, M. Sarazin, A. Tokovinin, T. Travouillon, and O. Voziakova. Comparison of the scintillation noise above different observatories measured with MASS instruments. *A&A* , 546, October 2012.

[76] R. Kraft Vanderspek, G. R. Ricker, D. W. Latham, K. Ennico, G. Bakos, T. M. Brown, A. J. Burgasser, D. Charbonneau, M. Clampin, L. Deming, J. P. Doty, E. W. Dunham, J. L. Elliot, M. J. Holman, S. Ida, J. M. Jenkins, J. G. Jernigan, N. Kawai, G. P. Laughlin, J. J. Lissauer, F. Martel, D. D. Sasselov, R. H. Schingler, S. Seager, A. Szentgyorgyi, G. Torres, S. Udry, J. N. Villasenor, J. N. Winn, and S. P. Worden. High-Precision Imaging Photometers for the Transient Exoplanet Survey Satellite. In *American Astronomical Society Meeting Abstracts #215*, volume 42 of *Bulletin of the American Astronomical Society*, January 2010.

[77] M. Lendl, M. Gillon, D. Queloz, R. Alonso, A. Fumel, E. Jehin, and D. Naef. A photometric study of the hot exoplanet WASP-19b. *A&A* , 552:A2, April 2013.

[78] S.-L. Li, N. Miller, D. N. C. Lin, and J. J. Fortney. WASP-12b as a prolate, inflated and disrupting planet from tidal dissipation. *Nature* , 463:1054–1056, February 2010.

[79] D. N. C. Lin and J. Papaloizou. On the tidal interaction between protoplanets and the protoplanetary disk. III - Orbital migration of protoplanets. *ApJ* , 309:846–857, October 1986.

[80] J. J. Lissauer. Urey prize lecture: On the diversity of plausible planetary systems. , 114:217–236, April 1995.

[81] J. Llama, K. Wood, M. Jardine, A. A. Vidotto, C. Helling, L. Fossati, and C. A. Haswell. The shocking transit of WASP-12b: modelling the observed early ingress in the near-ultraviolet. *MNRAS* , 416:L41–L44, September 2011.

[82] B. Lopez and M. Sarazin. The ESO atmospheric temporal coherence monitor dedicated to high angular resolution imaging. *A&A* , 276:320–+, September 1993.

[83] M. López-Morales and S. Seager. Thermal Emission from Transiting Very Hot Jupiters: Prospects for Ground-based Detection at Optical Wavelengths. *ApJ* , 667:L191–L194, October 2007.

[84] M. López-Morales, J. L. Coughlin, D. K. Sing, A. Burrows, D. Apai, J. C. Rogers, D. S. Spiegel, and E. R. Adams. Day-side z'-band Emission and Eccentricity of WASP-12b. *ApJ* , 716:L36–L40, June 2010.

[85] N. Madhusudhan and S. Seager. A temperature and abundance retrieval method for exoplanet atmospheres. *ApJ* , 707(1):24, 2009.

[86] N. Madhusudhan, J. Harrington, K. B. Stevenson, S. Nymeyer, C. J. Campo, P. J. Wheatley, D. Deming, J. Blecic, R. A. Hardy, N. B. Lust, D. R. Anderson,

A. Collier-Cameron, C. B. T. Britt, W. C. Bowman, L. Hebb, C. Hellier, P. F. L. Maxted, D. Pollacco, and R. G. West. A high C/O ratio and weak thermal inversion in the atmosphere of exoplanet WASP-12b. *Nature* , 469: 64–67, January 2011.

[87] Nikku Madhusudhan. C/o ratio as a dimension for characterizing exoplanetary atmospheres. *ApJ* , 758(1):36, 2012.

[88] K. Mandel and E. Agol. Analytic Light Curves for Planetary Transit Searches. *ApJ* , 580:L171–L175, December 2002.

[89] P. Martinez, J. Kolb, M. Sarazin, and J. Navarrete. Active optics Shack-Hartmann sensor: using spot sizes to measure the seeing at the focal plane of a telescope. *MNRAS* , 421:3019–3026, April 2012.

[90] D. L. Mary. A statistical analysis of the detection limits of fast photometry. *A&A* , 452:715–726, June 2006.

[91] M. Mayor and D. Queloz. A Jupiter-mass companion to a solar-type star. *Nature* , 378:355–359, November 1995.

[92] T. Mazeh, P. Guterman, S. Aigrain, S. Zucker, N. Grinberg, A. Alapini, R. Alonso, M. Auvergne, M. Barbieri, P. Barge, P. Bordé, F. Bouchy, H. Deeg, R. de La Reza, M. Deleuil, R. Dvorak, A. Erikson, M. Fridlund, P. Gondoin, L. Jorda, H. Lammer, A. Léger, A. Llebaria, P. Magain, C. Moutou, M. Ollivier, M. Pätzold, F. Pont, D. Queloz, H. Rauer, D. Rouan, R. Sabo, J. Schneider, and G. Wuchterl. Removing systematics from the CoRoT light curves. I. Magnitude-dependent zero point. *A&A* , 506:431–434, October 2009.

[93] Jordi Miralda-Escude. Orbital perturbations of transiting planets: A possible method to measure stellar quadrupoles and to detect earth-mass planets. *The Astrophysical Journal*, 564(2):1019, 2002.

[94] A. F. J. Moffat. A Theoretical Investigation of Focal Stellar Images in the Photographic Emulsion and Application to Photographic Photometry. *A&A* , 3:455, December 1969.

[95] L. Mortara and A. Fowler. Evaluations of Charge-Coupled Device / CCD / Performance for Astronomical Use. In *Society of Photo-Optical Instrumentation Engineers (SPIE) Conference Series*, volume 290 of *Society of Photo-Optical Instrumentation Engineers (SPIE) Conference Series*, page 28, January 1981.

[96] T. Naylor. An optimal extraction algorithm for imaging photometry. *MNRAS* , 296:339–346, May 1998.

[97] J. A. Nelder and R. Mead. A simplex method for function minimization. *The Computer Journal*, 7(4):308–313, 1965.

[98] N. S. Nightingale and D. F. Buscher. Interferometric seeing measurements at the La Palma Observatory. *MNRAS* , 251:155–166, July 1991.

[99] G. R. Ochs and R. J. Hill. Optical-scintillation method of measuring turbulence inner scale. *Appl. Opt.* , 24:2430–2432, August 1985.

[100] J. Osborn. *Proling the turbulent atmosphere and novel correction techniques for imaging and photometry in astronomy.* PhD thesis, Durham University, 2010.

[101] J. Osborn. Scintillation correction for astronomical photometry on large and extremely large telescopes with tomographic atmospheric reconstruction. *MNRAS* , 446:1305–1311, January 2015.

[102] J. Osborn, R. W. Wilson, V. S. Dhillon, R. Avila, and G. D. Love. Conjugate-plane photometry: reducing scintillation in ground-based photometry. *MNRAS* , 411:1223–1230, February 2011.

[103] J. Osborn, R. W. Wilson, H. W. Shepherd, T. Butterley, V. S. Dhillon, and R. Avila. Stereo SCIDAR: Profiling Atmospheric Optical Turbulence with Improved Altitude Resolution. *Proc. Third AOELT Conf. INAF Osservatorio Astrofisico di Arcetri*, 2013.

[104] J. Osborn, R. W. Wilson, V. S. Dhillon, R. Avila, and G. D. Love. Conjugate-plane photometry: reducing scintillation in ground-based photometry. *MNRAS* , in prep.

[105] M. Pedani. La palma sky brightness. www.tng.iac.es/info/la_palma_sky.html, 2002.

[106] R. Perna, K. Heng, and F. Pont. The Effects of Irradiation on Hot Jovian Atmospheres: Heat Redistribution and Energy Dissipation. *ApJ* , 751:59, May 2012.

[107] A. Phillips, M. G. Burton, M. C. B. Ashley, J. W. V. Storey, J. P. Lloyd, D. A. Harper, and J. Bally. The Near-Infrared Sky Emission at the South Pole in Winter. *ApJ* , 527:1009–1022, December 1999.

[108] F. Pont. Changing views on the radius inflation of hot jupiters. www.exoclimes.com/topics/changing-views-on-the-radius-inflation-of-hot-jupiters/, 2012.

[109] F. Pont, S. Zucker, and D. Queloz. The effect of red noise on planetary transit detection. *MNRAS* , 373:231–242, November 2006.

[110] W.H. Press, S.A. Teukolsky, W.T. Vetterling, and B.P. Flannery. *Numerical recipes 3rd edition: The art of scientific computing*. Cambridge University Press, 2007.

[111] William H. Press, Saul A. Teukolsky, William T. Vetterling, and Brian P. Flannery. *Numerical Recipes 3rd Edition: The Art of Scientific Computing*. Cambridge University Press, 3 edition, September 2007. ISBN 0521880688.

[112] P. Puget, E. Stadler, R. Doyon, P. Gigan, S. Thibault, G. Luppino, G. Barrick, T. Benedict, T. Forveille, W. Rambold, J. Thomas, T. Vermeulen, J. Ward, J.-L. Beuzit, P. Feautrier, Y. Magnard, G. Mella, O. Preis, P. Vallee, S.-y. Wang, C.-J. Lin, D. N. Hall, and K. W. Hodapp. WIRCam: the infrared wide-field camera for the Canada-France-Hawaii Telescope. In *Ground-based*

Instrumentation for Astronomy, volume 5492 of *Society of Photo-Optical Instrumentation Engineers (SPIE) Conference Series*, pages 978–987, September 2004.

[113] C. Rao, W. Jiang, and N. Ling. Spatial and temporal characterization of phase fluctuations in non-Kolmogorov atmospheric turbulence. *Journal of Modern Optics*, 47:1111–1126, June 2000.

[114] E. Rauscher, K. Menou, J. Y.-K. Cho, S. Seager, and B. M. S. Hansen. Hot Jupiter Variability in Eclipse Depth. *ApJ* , 662:L115–L118, June 2007.

[115] L. Jeremy Richardson, Drake Deming, Guenter Wiedemann, Cedric Goukenleuque, David Steyert, Joseph Harrington, and Larry W. Esposito. Infrared observations during the secondary eclipse of hd 209458b. i. 3.6 micron occultation spectroscopy using the very large telescope. *The Astrophysical Journal*, 584(2):1053, 2003.

[116] F. Roddier. The effects of atmospheric turbulence in optical astronomy. *Progress in optics. Volume 19. Amsterdam, North-Holland Publishing Co., 1981, p. 281-376.*, 19:281–376, 1981.

[117] F. Roddier and E. Wolf. Progress in Optics. *Vol*, 19:281, 1981.

[118] A. Rodríguez, S. Ferraz-Mello, T. A. Michtchenko, C. Beaugé, and O. Miloni. Tidal decay and orbital circularization in close-in two-planet systems. *MNRAS* , 415:2349–2358, August 2011.

[119] J. C. Rogers, D. Apai, M. López-Morales, D. K. Sing, and A. Burrows. Ks-Band Detection of Thermal Emission and Color Constraints to CoRoT-1b: A Low-Albedo Planet with Inefficient Atmospheric Energy Redistribution and a Temperature Inversion. *ApJ* , 707:1707, December 2009.

[120] R. Russell. Troposphere. www.windows2universe.org/earth/Atmosphere/troposphere.html 2009.

[121] P. D. Sackett. Searching for Unseen Planets via Occultation and Microlensing. In J.-M. Mariotti and D. Alloin, editors, *NATO ASIC Proc. 532: Planets Outside the Solar System: Theory and Observations*, page 189, 1999.

[122] Gideon Schwarz. Estimating the Dimension of a Model. *The Annals of Statistics*, 6(2):461–464, 1978.

[123] S. Seager and G. Mallén-Ornelas. A Unique Solution of Planet and Star Parameters from an Extrasolar Planet Transit Light Curve. *ApJ* , 585:1038–1055, March 2003.

[124] R. M. Sharples, R. Bender, M. D. Lehnert, S. K. Ramsay Howat, M. N. Bremer, R. L. Davies, R. Genzel, R. Hofmann, R. J. Ivison, R. Saglia, and N. A. Thatte. KMOS: an infrared multiple-object integral field spectrograph for the ESO VLT. In *Ground-based Instrumentation for Astronomy*, volume 5492 of *Society of Photo-Optical Instrumentation Engineers (SPIE) Conference Series*, pages 1179–1186, September 2004.

[125] H. W. Shepherd, J. Osborn, R. W. Wilson, T. Butterley, R. Avila, V. S. Dhillon, and T. J. Morris. Stereo-SCIDAR: optical turbulence profiling with high sensitivity using a modified SCIDAR instrument. *MNRAS* , 437:3568–3577, February 2014.

[126] Adam P Showman, Jonathan J Fortney, Yuan Lian, Mark S Marley, Richard S Freedman, Heather A Knutson, and David Charbonneau. Atmospheric circulation of hot jupiters: Coupled radiative-dynamical general circulation model simulations of hd 189733b and hd 209458b. *ApJ* , 699(1):564, 2009.

[127] D. K. Sing and M. López-Morales. Ground-based secondary eclipse detection of the very-hot Jupiter OGLE-TR-56b. *A&A* , 493:L31–L34, January 2009.

[128] John Southworth, TC Hinse, UG Jørgensen, M Dominik, Davide Ricci, MJ Burgdorf, Allan Hornstrup, PJ Wheatley, T Anguita, V Bozza, et al. High-precision photometry by telescope defocusing–i. the transiting planetary system wasp-5. *MNRAS* , 396(2):1023–1031, 2009.

[129] Mark Swain, Pieter Deroo, Giovanna Tinetti, Morgan Hollis, Marcell Tessenyi, Michael Line, Hajime Kawahara, Yuka Fujii, Adam P. Showman, and Sergey N. Yurchenko. Probing the extreme planetary atmosphere of wasp-12b. *Icarus*, 225(1):432 – 445, 2013. URL `http://www.sciencedirect.com/science/article/pii/S0019103513001632`.

[130] O. Tamuz, T. Mazeh, and S. Zucker. Correcting systematic effects in a large set of photometric light curves. *MNRAS* , 356:1466–1470, February 2005.

[131] Tatarski. *Wave propagation in a turbulent medium.* McGraw-Hill, 1961.

[132] G. I. Taylor. The Spectrum of Turbulence. *Royal Society of London Proceedings Series A*, 164:476–490, February 1938.

[133] M. Tegmark, M. A. Strauss, M. R. Blanton, K. Abazajian, S. Dodelson, H. Sandvik, X. Wang, D. H. Weinberg, I. Zehavi, N. A. Bahcall, F. Hoyle, D. Schlegel, R. Scoccimarro, M. S. Vogeley, A. Berlind, T. Budavari, A. Connolly, D. J. Eisenstein, D. Finkbeiner, J. A. Frieman, J. E. Gunn, L. Hui, B. Jain, D. Johnston, S. Kent, H. Lin, R. Nakajima, R. C. Nichol, J. P. Ostriker, A. Pope, R. Scranton, U. Seljak, R. K. Sheth, A. Stebbins, A. S. Szalay, I. Szapudi, Y. Xu, J. Annis, J. Brinkmann, S. Burles, F. J. Castander, I. Csabai, J. Loveday, M. Doi, M. Fukugita, B. Gillespie, G. Hennessy, D. W. Hogg, Ž. Ivezić, G. R. Knapp, D. Q. Lamb, B. C. Lee, R. H. Lupton, T. A. McKay, P. Kunszt, J. A. Munn, L. O'Connell, J. Peoples, J. R. Pier, M. Richmond, C. Rockosi, D. P. Schneider, C. Stoughton, D. L. Tucker, D. E. vanden Berk, B. Yanny, and D. G. York. Cosmological parameters from SDSS and WMAP. *Phys. Rev. D* , 69(10):103501, May 2004.

[134] J. Vernin. Mechanism of formation of optical turbulence. In *Astronomical Site Evaluation in the Visible and Radio Range*, volume 266 of *Astronomical Society of the Pacific Conference Series*, page 2, 2002.

[135] J. Vernin, R. Barletti, G. Ceppatelli, L. Paternò, A. Righini, and N. Speroni. Optical remote sensing of atmospheric turbulence: a comparison with simultaneous thermal measurements. *Appl. Opt.*, 18(2):243–247, 1979.

[136] Jean Vernin, Michel Crochet, Max Azouit, and Ogubazghi Ghebrebrhan. Sodar/radar simultaneous measurements of atmospheric turbulence. *Radio Science*, 25(5):953–959, 1990.

[137] A. Vidal-Madjar, A. Lecavelier des Etangs, J.-M. Désert, G. E. Ballester, R. Ferlet, G. Hébrard, and M. Mayor. An extended upper atmosphere around the extrasolar planet HD209458b. *Nature*, 422:143–146, March 2003.

[138] R. J. Wainscoat and L. L. Cowie. A filter for deep near-infrared imaging. *AJ* , 103:332–337, January 1992.

[139] R. Wilson. Results of the JOSE site evaluation project for adaptive optics at the William Herschel Telescope. , 42:465–469, November 1998.

[140] R. W. Wilson, T. Butterley, and M. Sarazin. The Durham/ESO SLODAR optical turbulence profiler. *MNRAS* , 399:2129–2138, November 2009.

[141] R.W. Wilson, N. O'Mahony, C. Packham, and M. Azzaro. The seeing at the William Herschel Telescope. *Monthly Notices of the Royal Astronomical Society*, 309(2):379–387, 1999.

[142] J. N. Winn. Transits and Occultations. *ArXiv e-prints*, January 2010.

[143] A. T. Young. Photometric error analysis. VI. Confirmation of Reiger's theory of scintillation. *AJ*, 72:747, August 1967.

[144] M. Zhao, J. D. Monnier, M. R. Swain, T. Barman, and S. Hinkley. Ground-based Detections of Thermal Emission from CoRoT-1b and WASP-12b. *ApJ* , 744:122, January 2012.

[145] A. Ziad, J. Borgnino, F. Martin, J. Maire, and D. Mourard. Towards the monitoring of atmospheric turbulence model. *A&A* , 414:L33–L36, January 2004.

[146] A. Zilberman, E. Golbraikh, N. S. Kopeika, A. Virtser, I. Kupershmidt, and Y. Shtemler. Lidar study of aerosol turbulence characteristics in the tropo-

sphere: Kolmogorov and non-Kolmogorov turbulence. *Atmospheric Research*, 88:66–77, April 2008.

[147] W. Zima, T. Arentoft, J. De Ridder, S. Salmon, C. Catala, H. Kjeldsen, and C. Aerts. The PLATO End-to-End CCD Simulator – Modelling spaaaaaace-based ultra-high precision CCD photometry for the assessment study of the PLATO Mission. *ArXiv e-prints*, April 2010.